𝕬𝖗𝖌𝖔𝖓𝖓𝖊 𝕹𝖆𝖙𝖎𝖔𝖓𝖆𝖑 𝕷𝖆𝖇𝖔𝖗𝖆𝖙𝖔𝖗𝖞

REACTOR DEVELOPMENT PROGRAM
PROGRESS REPORT

June 1969

The facilities of Argonne National Laboratory are owned by the United States Government. Under the terms of a contract (W-31-109-Eng-38) between the U. S. Atomic Energy Commission, Argonne Universities Association and The University of Chicago, the University employs the staff and operates the Laboratory in accordance with policies and programs formulated, approved and reviewed by the Association.

ARGONNE NATIONAL LABORATORY
9700 South Cass Avenue
Argonne, Illinois 60439

REACTOR DEVELOPMENT PROGRAM
PROGRESS REPORT

June 1969

Robert B. Duffield, Laboratory Director
Stephen Lawroski, Associate Laboratory Director

Division	Director
Chemical Engineering	R. C. Vogel
EBR-II Project	M. Levenson
Metallurgy	M. V. Nevitt
Reactor Engineering	L. J. Koch
Reactor Physics	R. Avery

Report coordinated by
A. Glassner and A. D. Rossin

Issued July 29, 1969

FOREWORD

The Reactor Development Program Progress Report, issued monthly, is intended to be a means of reporting those items of significant technical progress which have occurred in both the specific reactor projects and the general engineering research and development programs. The report is organized in accordance with budget activities in a way which, it is hoped, gives the clearest, most logical overall view of progress. Since the intent is to report only items of significant progress, not all activities are reported each month. In order to issue this report as soon as possible after the end of the month editorial work must necessarily be limited. Also, since this is an informal progress report, the results and data presented should be understood to be preliminary and subject to change unless otherwise stated.

The issuance of these reports is not intended to constitute publication in any sense of the word. Final results either will be submitted for publication in regular professional journals or will be published in the form of ANL topical reports.

The last six reports issued
in this series are:

November 1968	ANL-7518
December 1968	ANL-7527
January 1969	ANL-7548
February 1969	ANL-7553
March 1969	ANL-7561
April-May 1969	ANL-7577

REACTOR DEVELOPMENT PROGRAM

Highlights of Project Activities for June 1969

EBR-II

The reactor was operated for 998 MWd from May 21 through June 20, raising its cumulated operation to 26,041 MWd.

The PNL-7 group of unencapsulated mixed-oxide elements was tagged successfully by the experimenter with a xenon isotopic mixture. This is the second group of test elements to be xenon tagged.

A redesigned stainless steel drop rod that provides a small, prompt reactivity step was installed in the reactor in Run 35. Indications are that reactivity changes are confined to rod positions ranging between 3 and 8 in. from full insertion, a region traversed by the rod in less than 90 msec. Total worth of the rod is 6 Ih.

ZPR-3

Assembly 57 has been constructed to provide an appropriate source of neutrons for the measurement of integral values of the capture-to-fission ratio (alpha) for U-233, U-235, and Pu-239 in a relatively low energy (10-keV range) spectrum. The core duplicates that of a previously studied subcritical (STSF-1A) and will be used for both reactivity-reaction rate measurements of alpha at low power and for high-power irradiations. In the latter work, alpha will be determined from changes in isotopic composition in irradiated foils. To permit greater shielding to be interposed in the matrix between reactor and control room, the assembly was built offcenter in the facility.

ZPR-6 and -9

Acceptance testing of the emergency steam turbine generator has been completed. Balancing of the supply and exhaust air systems for Building 316W is in progress. This constitutes part of the acceptance testing program for the air-exhaust systems.

ZPPR

Transition experiments with the FTR-I assembly continue. Uncertainty in control-rod calibration due to the spontaneous fission source in Pu-240 was shown to be less than 1%, and the total worth of 22 safety rods was determined to be 3.97% $\Delta k/k$. A temperature coefficient appropriate to the correction of measured reactivity differences was found to be -2.05 ± 0.49 Ih/°C. The reference loading of 362.84 kg (rather than 361.44 kg reported last month) was corrected for control-rod withdrawal and high neutron source to yield a critical mass of 359.14 kg for the unsmoothed heterogeneous assembly. FTR-I on ZPR-3 with its smaller void fraction had a critical mass of 331.94 kg.

TABLE OF CONTENTS

TABLE OF CONTENTS

TABLE OF CONTENTS

TABLE OF CONTENTS

I. LIQUID METAL FAST BREEDER REACTORS--CIVILIAN

A. Fuel Development--LMFBR

1. Oxide

a. Fuel Studies

(i) Fuel Element Performance (L. A. Neimark and F. L. Brown)

Last Reported: ANL-7577, pp. 1-10 (April-May 1969).

(a) Group O-2 Fuel Elements. Temperatures were calculated for the radial locations at which distinguishing features occurred in the microstructures of vibratorily compacted mixed-oxide Elements SOV-7, SOV-3, and HOV-15. These elements operated with 20 to 23% of the fuel in the molten state at the normal EBR-II power level of 45 MW. The exposure concluded with $1\frac{1}{2}$ days of operation at 30 MW, resulting in significant alteration of the fuel morphology previously obtained during operation at 45 MW.

Temperature calculations required measurements of the diameter of the molten-fuel boundary in order to establish a reference location of known temperature. Fuel restructuring at 30-MW operation obscured the location of the melt boundary over most of the length of the elements. However, the obscuring effect decreased toward the bottoms of the fuel columns, and transverse metallographic samples from within a centimeter or two of the bottoms exhibited melt boundaries that were sharp enough to be measured. Therefore, these samples were used for the temperature calculations.

The melt boundary is approximately contiguous with the inner edge of a band of concentrated fission products, which can be best delineated by beta-gamma autoradiography. In the upper regions of the fuel column, movement of fission products out of the band and up the radial temperature gradient was the principal factor that obscured the melt boundary.

As shown in Table I.A.1, the temperatures of structural features that could be readily identified on photomicrographs of these elements agreed well among the elements. The mean temperature of incipient formation of columnar grains was calculated as $1985 \pm 50°C$, and the temperature of formation of equiaxed grains was $1575 \pm 12°C$. Initial fuel densities had little effect on the thermal conductivity of the restructured fuel.

TABLE I.A.1. Temperatures at Selected Locations during Operation of Mixed-oxide Elements with Center Melting

	Fuel Elements			Effective Thermal Conductivity (cal/sec-cm-°C)	Density (% of Theoretical)
	SOV-7	SOV-3	HOV-15		
Smear density, %	85	83	80		
Maximum linear power, kW/ft	21.3	21.4	21.4		
Maximum burnup, a/o	3.6	3.7	3.5		
Temperature at melt boundary, °C	2790	2790	2790		
Columnar grains				0.00545[a]	99
Temperature at OD of columnar grains, °C	2034	2010	1934		
Equiaxed grains				0.00533-0.00501[a]	97
Temperature at OD of equiaxed grains, °C	1570	1563	1586		
Porous periphery				0.00478[b]	80-85
Temperature at fuel surface, °C	1154	1058	1233		
Gap				Conductance: 0.094-0.106 cal/sec-cm²-°C[c]	
Temperature at cladding inner surface, °C	522	528	508		
Volume of molten fuel, %	20	22	23		
Volume of central void, %	5.0	7.9	9.4		

[a]Corrected for fuel density; assumed constant above 2000°C. Asamoto's formula: Baily, W. E., et al., Thermal Conductivity of Uranium-Plutonium Oxide Fuels, Nucl. Metallurgy 13, 301 (1967).
[b]Minimum value suggested for design of Vipac elements at PNWL: Christenson, J. A., Determination of Oxide Fuel Temperature Profiles, BNWL-CC-604 (1966).
[c]Value for a $3\frac{1}{2}$-mil radial gap in a pellet element.

The calculations also indicated that the interface between the cladding and the porous peripheral vibratorily compacted fuel was equivalent to about a $3\frac{1}{2}$-mil radial gap in pellet fuel with a gap conductance of about 750 Btu/hr-ft²-°F.

(b) Group O-3 Fuel Elements. The 19 $(U,Pu)O_2$ fuel elements of Group O-3 (see Progress Report for January 1969, ANL-7548, pp. 1-2) have been inspected radiographically and visually. Ten elements were acceptable, eight are to be repaired, and one was rejected. The eight elements to be repaired had weld penetrations less than the 80% specified. The rejected Element, SOV-15, with Dynapak fuel and Type 304 stainless steel cladding, had a nick on the outer surface of the cladding. The nick had a depth of 10-13% of the wall thickness and, therefore, exceeded the maximum allowable defect thickness of 10%.

(ii) <u>Compatibility between Uranium-Plutonium Oxide and Cladding Alloys</u> (T. W. Latimer)

Last Reported: ANL-7577, pp. 4-5 (April-May 1969).

Although all vanadium alloys tested thus far have been hardened to some extent after contact with $(U_{0.8}Pu_{0.2})O_{1.97}$ at 700-800°C for 1000 hr, the presence of 5 w/o or more titanium in the alloys significantly affected the depth and degree of hardness of the hardened layer (see Progress Report for October 1968, ANL-7513, pp. 3-4). Heat treatment of compatibility couples has begun in order to determine the effect of smaller amounts of titanium on the hardness changes. The compatibility couples consist of $(U_{0.8}Pu_{0.2})O_{1.97}$ fuel and one of the following alloys, V-15 w/o Cr, V-15 w/o Cr-0.3 w/o Ti, and V-15 w/o Cr-1 w/o Ti; all will be heat treated for 1000 hr at 700°C.

2. <u>Carbide</u>

   a. <u>Fabrication and Evaluation</u>

      (i) <u>Fuel Element Performance</u> (L. A. Neimark and T. W. Latimer)

      Last Reported: ANL-7553, pp. 5-6 (Feb 1969).

      Four experimental (U,Pu) carbide fuel elements were discharged from EBR-II on April 3, 1969. These elements were from Subassembly XO15, which occupied a position in Row 4. Maximum midplane burnup of the peak element is estimated to be 6.7 a/o. Elements HMV-2 and NMV-3 were vibratorily compacted physical mixtures of UC-20 w/o PuC clad with Hastelloy-X and Nb-1 w/o Zr, respectively. Element TVMV-1 contained vibratorily compacted hyperstoichiometric $(U_{0.8}Pu_{0.2})C$ with V-20 w/o Ti cladding. Element NMP-1 contained stoichiometric $(U_{0.8}Pu_{0.2})C$ pellets with Nb-1 w/o Zr cladding. These elements are being neutron radiographed.

B. Physics Development--LMFBR

1. Experimental Reactor Physics

a. Fast Critical Experiments--Experimental Support (Illinois)

(i) Fission Process and Cross Section Data Related to Fast Reactors (R. Gold)

Last Reported: ANL-7553, p. 9 (Feb 1969).

(a) ^{252}Cf Half-life by Neutron Counting. Improvements in experimental techniques require modification of the recently reported[*] disintegration constant for ^{252}Cf, $(7.212 \pm 0.017) \times 10^{-4}$ day^{-1}, obtained by neutron counting. Certain discrepancies in our procedure for neutron calibration have been rectified. Review of past data plus the accumulation of more absolute evaluations yield a decay constant of $(7.243 \pm 0.022) \times 10^{-4}$ day^{-1} for the source identified as Cf No. 0; the revised calibrations affect the source ratio of Cf No. O/Ra-Be by only 0.05%. The weighted mean thus becomes $(7.239 \pm 0.016) \times 10^{-4}$ day^{-1}, with better internal consistency. This corresponds to a half-life of 957.5 ± 2.1 days or 2.621 ± 0.006 yr. Decay of the ^{252}Cf sample has now been observed for 5.8 yr.

b. Planning and Evaluation of FFTF Critical Assembly Experiments (A. Travelli)

Last Reported: ANL-7577, pp. 15-17 (April-May 1969).

(i) Computational Study of the Effect of Residual Na_2CO_3 on Sodium-voiding Experiments. The core compositions of fast critical assemblies considered in connection with the FFTF Critical Experiment Program at the Argonne National Laboratory may include some sodium carbonate. This material is sometimes used in critical assemblies in order to achieve sodium and oxygen concentrations very close to the concentrations desired for these elements without disturbing the concentrations of other essential materials.

The use of sodium carbonate plates often provides the experimenter with a considerable advantage for obtaining the proper concentrations in the core, but is accompanied by some disadvantages. The inconvenience of substituting carbon for oxygen in a core was investigated in the FARET program,[**] where it was determined that the atom ratio of oxygen to carbon for leakage and scattering equivalence is 0.87. Since oxygen is present in the FTR core compositions, an obvious and convenient procedure consists in reducing the oxygen concentration so that

---

* De Volpi, A., and Porges, K. G., Inorg. Nucl. Chem. Letters 5, 111 (1969).
** Persiani, P. J., Hess, A. L., and Kucera, D., ANL-7320 (1966), p. 560.

the sum of the oxygen concentration and 87% of the carbon concentration in the core added up to the desired oxygen concentration.

Another possible disadvantage of sodium carbonate in the core is that it is not possible to void the sodium entirely without disturbing seriously the concentration of other materials which contribute substantially to the core reactivity. Therefore, the results of an ideal experiment in which all of the sodium but only the sodium is removed from a core containing some sodium in the form of elemental sodium and some in the form of sodium carbonate must be inferred by extrapolation from the results obtained by removing all the elemental sodium but not the sodium carbonate. It is generally assumed that the uncertainty introduced by this type of correction is negligible when compared with other uncertainties of the measurements. A series of calculations was performed in order to assess the validity of this assumption.

In an experiment in which a large fraction of the core volume is voided of sodium it may be expected that the greatest discrepancy between experiment and calculation of the sodium-void effect would be found in the spectral component. This expectation is based on the fact that previous experience in the FTR Critical Experiments Program and for other assemblies[*] indicates that the leakage component of the sodium-void coefficient can be calculated in good agreement with the experimental data. This consideration, in addition to the fact that heterogeneity effects on the leakage component are expected to be small and approximately proportional to the sodium removal, makes it possible to restrict the study of the effect of the residual sodium carbonate on the sodium-void coefficient to the study of the effect on the spectral component only.

A series of calculations have been run for the cell of FTR-2 as built on the ZPPR. The purpose of the calculations was to ascertain the relative magnitude of the spectral reactivity effects which could be expected by removing progressively the elemental sodium from the core, and to find whether or not the results could be extrapolated to the spectral reactivity effect of removing all the sodium from the core.

Figure I.B.1 identifies the plate configuration of the two-drawer cell of FTR-1 and FTR-2 that was considered in the calculations (see Progress Report for December 1968, ANL-7527, p. 32).

Fig. I.B.1

FTR-2 Core Two-drawer Cell

---

[*]Helm, F. H., and Travelli, A., ANL-7210 (1966).

Three sets of cross sections were produced for this study through the MC^2 code* over a 29-group structure equivalent to the structure of Set 29004 (see ANL-7527, p. 10). The sets, labeled Sets #1, 2, and 3, provided the cross sections for the various isotopes for the cases, respectively, when no sodium was removed from the cell, when all the elemental sodium was removed, and when all the sodium was removed including the sodium contained in the cell in the form of sodium carbonate. The main differences between the cross sections of various sets were due to the different degree of self-shielding of the resonances in the low-energy region for different degrees of sodium voiding. The resonance self-shielding of the resonances is treated by MC^2 according to the equivalence principle.

A calculation of the material buckling was run with Set #1 for a homogeneous cell equivalent to the FTR-1 cell and for $k = 1$. The result found for the material buckling was $B_m^2 = 1.878 \times 10^{-3}$ cm^{-2}.

A series of S_{14} calculations with a modified single-Gaussian quadrature** was then run by means of the one-dimensional Argonne discrete S_n code SNARG-1D† and using the three cross-section sets previously derived. All SNARG calculations were run in plane geometry and corresponded closely to the cell represented in Fig. I.B.1 with periodic boundary conditions. The stainless steel between the drawers of the cell was considered to be equivalent to additional plates with appropriate thicknesses and compositions. The stainless steel contained in the cans of some of the plates was smeared over the volume of the corresponding plates. All other stainless steel contained in the cell was smeared uniformly over the cell volume, and so was any void present in the cell. The mesh-point distribution was chosen so that at least four mesh intervals would be found over every plate region. The transverse buckling was chosen to be equal in all cases to the value of the material buckling obtained in the homogeneous calculation previously mentioned.

The calculations consisted of the determination of the real fluxes and of k for the cell and for the following cases:

A. The heterogeneous cell as described in Fig. I.B.1, with the cross sections of Set #1.

B. The heterogeneous cell as described in Fig. I.B.1, but with the sodium removed from the 0.5-in. sodium plate in the left drawer of that figure. The cross sections were again taken from Set #1 in all regions, with the exception of the Pu-U-Mo and U_3O_8 plates adjacent to the voided region. The cross sections for these plates were obtained by interpolation between Sets #1 and #2.

---

*Toppel, B. J., Rago, A. L., and O'Shea, D. M., ANL-7318 (1967).
**Meneghetti, D., Nucl. Sci. Eng. 4, 295 (1962).
† Duffy, G. J., et al., ANL-7221 (1966).

C. The same as B, but with the sodium removed from the 0.5-in. sodium plate in the right drawer of that figure.

D. The heterogeneous cell as described in Fig. I.B.1, but with the sodium removed from both the 0.5-in. sodium plates present in the two drawers of the cell. The cross sections were taken as in B.

E. The heterogeneous cell as described in Fig. I.B.1, but with the sodium removed from all the plates in the cell which contain elemental sodium. The cross sections of Set #2 were used in all regions.

F. The heterogeneous cell as described in Fig. I.B.1, but with the sodium removed from all the plates in the cell which contain sodium, either in the form of elemental sodium or in the form of sodium carbonate. The cross sections of Set #3 were used in all regions.

The results of these calculations are summarized in Fig. I.B.2. The changes in reactivity are due to the combination of the effects that sodium removal at various locations of the heterogeneous cell has on the resonance self-shielding and on the broad-group structure of the flux across the cell. The effect on the resonance self-shielding is estimated to account for approximately 13% of the reactivity change following total sodium voiding.
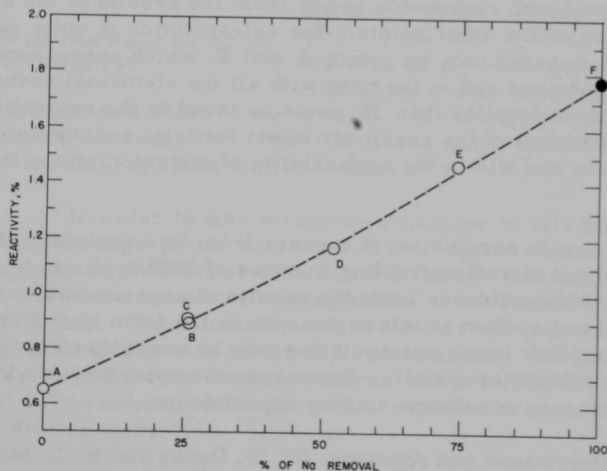
Fig. I.B.2. Spectral Reactivity Effects for Various Sodium-voiding
Configurations in the FTR-2 Core Cell

It may be noticed from Fig. I.B.2 that removals of equal amounts of sodium from the cell have different reactivity effects, depending

on the location from which the sodium is removed (compare the reactivity difference between points B and A with the reactivity difference between points C and A), on how much sodium has already been removed (compare the reactivity difference between points D and B with the reactivity difference between C and A), and on the thickness of the voided regions (compare the reactivity difference between points E and D with the reactivity difference between D and C). These differences correspond to the higher-order perturbation effects that have prompted this investigation. The high-order reactivity effects, however, appear to be rather small in comparison with the first-order reactivity effects of the sodium removal in the FTR-2 cell. Their magnitude is never larger than 20% of the first-order effects, and it seldom exceeds 10% of those effects. This may be due in part to the judicious way in which the plate arrangement was chosen in the FTR-2 cell, but results obtained both theoretically and experimentally for a very different case indicate that this conclusion may have a more general validity.

An important effect of the relatively small ratio of second- to first-order reactivity effects, and of their being somewhat constant with sodium content, is found in the remarkably regular pattern of the integrated reactivity effects versus fraction of sodium voiding as shown in Fig. I.B.2. It appears that the results of Case F, which correspond to the desired situation of total sodium voiding but which is not experimentally feasible, can be extrapolated with reasonable safety from the results of the experiments corresponding to the other points. The extrapolation is quite satisfactory even when it is based only on points A and E, which correspond physically to the unvoided core and to the core with all the elemental sodium removed. A relative error smaller than 3% would be found in the evaluation of the spectral component of the reactivity effect for total sodium removal with this procedure and within the applicability of the calculations that have been described.

In conclusion, it appears from this study that the spectral reactivity effect of sodium voiding in cores of FTR type can be extrapolated with reasonable confidence from the results of experiments in which a small amount of sodium is left in the core in the form of sodium carbonate. The error implicit in the extrapolation may be considered very small in comparison with heterogeneity effects and other phenomena which currently limit the accuracy of sodium-voiding experiments.

2. ZPR-3 Operations and Analysis (W. G. Davey and R. L. McVean)

Last Reported: ANL-7577, pp. 17-35 (April-May 1969).

a. Basic Studies of Plutonium Systems

(i) Assembly 57. Assembly 57 has been built and experiments have begun. The main purpose of this assembly is to obtain an integral value of the capture-to-fission rates (alpha) of the fissile

and Pu-239 in a relatively soft spectrum (10-keV range). This parameter will be determined by the reactivity-reaction rate method and by the high-power irradiation of high-purity foils. The foil irradiations and source-effect measurements needed for the former experiment have been done.

Assembly 57 is a three-region assembly, with a central core surrounded by an inner reflector of iron and an outer reflector of depleted uranium. It is basically a duplicate of the STSF-1A subcritical assembly built at Gulf General Atomic, with an enlargement of the core to achieve criticality and the addition of the depleted uranium reflector to provide additional radiation shielding. The core contains plates of enriched uranium, depleted uranium, and beryllium oxide in the one-drawer-cell configuration shown in Fig. I.B.3.

FRONT DRAWER – TOP VIEW

BACK DRAWER – TOP VIEW

Fig. I.B.3. Core and Axial Blanket Loadings for ZPR-3 Assembly 57

The plates have a nonhydrogenous coating whose thickness affects the geometry in two ways. The coating of the 0.125 x 0.89 x 1.75-in. enriched-uranium CANEL fuel causes the length of the columns of 9 fuel plates to be 1/16-1/8 in. longer than the 8 in. of the other materials. Also, to accommodate the increase in plate thickness, the nominal width of the materials in the cell has been reduced by 1/16 in. from the usual 2 in. The 1.75-in. height of the CANEL plates gives a 1/4-in. channel above the fuel columns.

In order to take maximum advantage of this as a cooling channel during the high-power run, the axial reflector columns behind the fuel were also made shorter, as shown in Fig. I.B.3. The materials inventory permitted the use of the loading shown in the central 13 drawers of each matrix half. The remaining axial reflector and the radial reflector consisted of solid blocks of iron and depleted uranium. The core control and safety drawers have the same loading as shown in Fig. I.B.3 except for the removal of one column of Beo, iron, and depleted uranium required by the thicker drawer walls.

The geometry of Assembly 57 is shown in Fig. I.B.4. The atom densities in each of the regions are listed in Table I.B.1. The breakdown of the assembly into regions is complicated by four characteristics of the assembly.

(1) Each matrix contains a 7 x 7 array of aluminum tubes which was placed in the matrix of stainless steel tubes. The core is loaded in the aluminum tubes. Thus the axial reflector is in aluminum tubes, while the radial is, in general, in stainless steel tubes.

(2) The core drawers, containing some axial reflector, are aluminum. Their back drawers, containing the remainder of the axial reflector, are stainless steel.

(3) The central axial reflector has cooling channels, which gives them lower atom densities than the solid reflector regions.

(4) The radial reflector in the aluminum matrix is in drawers. In the stainless steel matrix the pieces are loaded directly into the matrix.
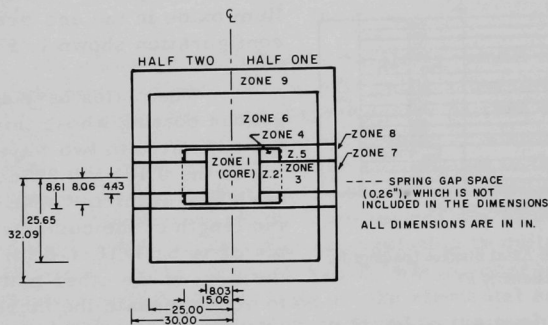
Fig. I.B.4. Equivalent Cylindrical Loading for Critical Loading of ZPR-3 Assembly 57

TABLE I.B.1. Composition of Assembly 57 of ZPR-3

Zone	Atom Density (x 10^{22} atoms/cm^3)									
	U-235	U-238	Be	O	Al	Fe	Cr	Ni	Mn	Si
Core										
Zone 1	0.4081	0.6347	3.901	3.901	0.5546	-	-	-	-	-
Safety, Control Rods	0.4065	0.6322	3.533	3.533	0.4339	0.5281	0.1314	0.0575	0.0055	0.0064
Inner Reflector										
Zone 2	-	-	-	-	0.5472	6.555	0.0506	0.0221	0.0021	0.0025
Zone 3	-	-	-	-	0.4339	5.000	1.243	0.5443	0.0519	0.0609
Zone 4	-	-	-	-	0.5472	7.093	-	-	-	-
Zone 5	-	-	-	-	0.4339	7.205	0.0262	0.0115	0.0011	0.0013
Zone 6	-	-	-	-	-	7.554	0.1129	0.0494	0.0047	0.0055
Safety Rod--Core	-	-	-	-	0.4339	5.226	1.300	0.5689	0.0543	0.0637
Safety Rod--Reflector	-	-	-	-	-	4.521	1.125	0.4921	0.0469	0.0551
Outer Reflector										
Zone 7	0.0078	3.741	-	-	0.4339	0.1053	0.0262	0.0115	0.0011	0.0013
Zone 8	0.0083	4.000	-	-	0.4339	0.1053	0.0262	0.0115	0.0011	0.0013
Zone 9	0.0083	3.989	-	-	0.4540	0.1129	0.0494	0.0047	0.0055
Safety Rod--Core	0.0076	3.619	-	-	0.4339	0.4926	0.1225	0.0536	0.0051	0.0060
Safety Rod--Reflector	0.0077	3.674	-	-	-	0.9487	0.2360	0.1033	0.0099	0.0116
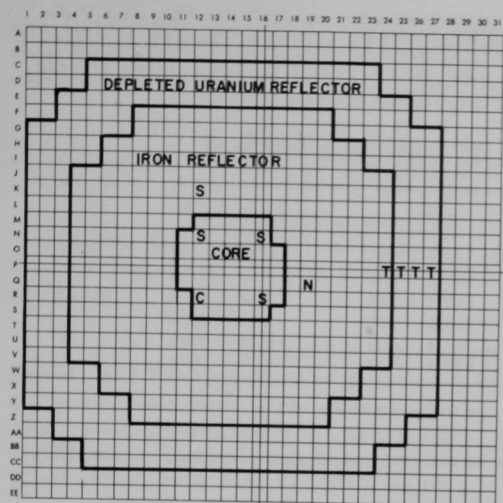
LOADING 57-12   HALF I

S=SAFETY ROD C=CONTROL ROD T=SOURCE TUBE
DRAWER N=NEUTRON LEVEL DETECTOR

Fig. I.B.5. Critical Loading of ZPR-3 Assembly 57

The critical loading of Assembly 57 is shown in Fig. I.B.5. Half 2 has the same loading as that shown for Half 1 except for not having a neutron-level detector. The assembly was built offcenter in the matrix to provide additional matrix locations on the control-room side for shielding materials. This loading contained 85.59 kg U-235, and was critical with one control rod withdrawn 4.35 in. and all other rods fully inserted. The integral worth of the control rod at this position is 152 Ih, which is equivalent to 1.12 kg U-235. The critical mass is then 84.47 kg U-235. When corrected for core differences, this compares well with the extrapolated critical mass of 89 kg U-235 for the STSF-1A.

The STSF-1A assembly had a central drawer on one half replaced with the accelerator beam tube and had a radial drift tube hole extending to the core axis in the other half, at approximately 5 in. from the matrix interface. The replacement of the core drawer at 1-P-14 with a proton-recoil counter drawer raised the critical mass to 87.5 kg U-235. Compensation for a drift-tube hole would raise this to close to the extrapolated value. The control and safety drawers in the core are worth 240 Ih each. The safety drawers in the iron reflector are worth 15 Ih each.

(ii) Assemblies 53 and 54. Corrected critical masses for Assemblies 53 and 54 have been calculated for core temperatures of 34.6 and 36.1°C, respectively. Estimates for the reactivity difference between the jagged outline and a circularized core proved negligible, and since no safety or control rods were spiked in either assembly, the only corrections to the critical mass were for positioning of control rods. Results of these corrections give loaded and corrected masses in Table I.B.2.

TABLE I.B.2. Corrected Critical Masses for ZPR-3 Assemblies 53 and 54

Assembly	Loaded Mass (kg)		Corrected Mass (kg)	
	Pu-239 + Pu-241	U-235	Pu-239 + Pu-241	U-235
53	149.9	0.53	148.62	0.53
54	130.8	0.46	129.8	0.46

The reactivity Doppler results for natural UO_2 and PuO_2 in Assembly 53 are listed in Table I.B.3. The values given are experimental reactivity increments and are not corrected for expansion effects. The inhours/% Δk conversion for Assembly 53 was 1045.6.

TABLE I.B.3. Reactivity Doppler Measurements in ZPR-3 Assembly 53

Temp (°K)	$\Delta\rho$ (Ih)	$\Delta\rho$ (Ih/kg)[a]
UO_2: 301-499	-0.537 ± 0.005	-4.43 ± 0.04
301-799	-1.155 ± 0.005	-9.54 ± 0.04
301-1101	-1.649 ± 0.005	-13.62 ± 0.04
PuO_2: 354-502	-0.288 ± 0.006	-2.54 ± 0.05
354-801	-0.703 ± 0.006	-6.20 ± 0.05
354-1100	-0.993 ± 0.006	-8.76 ± 0.05

[a]For UO_2, Ih/kg U-238; for PuO_2, Ih/kg Pu-239.

The total worths of the unheated samples were: for UO_2 (120.1 g U-238, 0.84 g U-235, 16.2 g O) at 301°K, -7.16 ± 0.15 Ih; for PuO_2 (113.4 g Pu-239, 3.01 g Pu-240, 0.145 g Pu-241, 15.6 g O) at 354°K, +77.1 ± 0.2 Ih. The experiment was performed with a 3/8-in. graphite buffer around the Doppler rod, separating it from the normal core environment.

3. ZPR-6 and -9 Operations and Analysis (W. Y. Kato and C. E. Till)

Last Reported: ANL-7577, pp. 35-38 (April-May 1969).

a. Integral Studies of Large Systems

(i) VTRZ Facility Development. Two maximum temperature runs of the Variable Temperature Rodded Zone (VTRZ) prototype: a 3-hr run of April 25 and a 100-hr run of May 12-16 were made. In general, all subsystems of the prototype worked well and demonstrated the basic feasibility of the design. In particular, the following conclusions were drawn:

1. The inner-barrel containment envelope for the argon cover gas works well. No leaks occurred in the metal "O"-ring seals or in the thermocouple or power-lead penetrations. Normal care is apparently sufficient to assure reliable operation of these seals after repeated removal and installation.

2. The general heating arrangement for the inner matrix was good, providing reasonable heatup and equilibration rates. The three-bus, SCR-controlled cartridge-heater arrangement worked well.

3. The cooling guard ring (CGR), rapid cool-down (RCD), and outer matrix-cooling (OMC) air systems worked well mechanically

and electrically, provided adequate cooling capacity, and maintained reasonable outer-barrel temperatures. The insulation around the inner barrel worked well mechanically and provided an adequate thermal barrier.

4. The inner matrix and calandria system worked well, with no binding and only small distortions after repeated runs.

5. Adequate space has been provided in the design for mechanical and electrical connections and manipulation. Heater, fuse, thermocouple, and swelling monitor connections inside the heated zone are workable.

6. Expansion and support of the heated zone on the ball mounts and the operation of the axial guides was good except for cracking of the ceramic inserts as discussed below. Only a small amount of heat was transferred through the ball mounts, and that heat was carried away by the CGR and OMC cooling-air systems.

Operation of the VTRZ prototype has indicated several areas in which the prototype design is not optimum. None of these constitute a safety hazard, but significant improvement in operation, particularly from an experimental point of view, can be achieved by making appropriate changes in the final design. The major areas in which design improvements can be made are the following:

1. The prototype design of the cooling-guard-ring ducts permit an unnecessary amount of air leakage out of them, around the insulation, and along the outer surfaces of the heated zone. This results in unnecessary radial heat losses and low surface temperatures. The design has been changed to provide for sealed CGR ducts in order to prevent cooling-air leakage.

2. The originally specified insulation material was inappropriate for several reasons, including loss of strength after heating. Several insulation materials have been found which have adequate strength and lower content of residual hydrogen. One of three possibilities will be chosen for the final design.

3. Some minor local buckling of the heated matrix was observed after the high-temperature runs. This is attributable to thermal stresses set up by inadequate temperature control of the front and rear covers and flanges. Normal heat transfer from the heated matrix was not sufficient to keep all of the heated-zone extremities close to the matrix in temperature. In order to control this situation, tubular heaters are being placed at strategic locations on the outside of the inner barrel to permit control of extremity temperatures.

4. The alumina plates and balls used in the ball mounts are apparently of insufficient strength under operating conditions. Cracks were observed in some of the alumina plates. These plates are used as inserts, to provide a bearing surface, at the ends of the Type 304 stainless steel ball-mount brackets. The alumina plates and balls are being replaced by much stronger tungsten carbide plates and balls.

Construction of a prototype model of the argon loop and of the instrumentation for this loop is nearly complete. Tests of the heater fuses and of the plutonium-alpha monitors have been successfully completed. A workable design of the swelling monitor operated successfully in the 100-hr run. The design of the temperature, pressure, and flow-rate monitoring equipment and the associated interlock circuitry is about 50% complete.

4. ZPPR Operations and Analysis (W. G. Davey and P. I. Amundson)

Last Reported: ANL-7577, pp. 38-42 (April-May 1969).

   a. Doppler Effect

   (i) Reactivity Doppler Equipment. The ZPPR reactivity Doppler mechanism has been checked out and a UO_2 capsule has been heated to 800°C. All systems performed satisfactorily, except that the power input of the temperature controller was barely sufficient to reach the desired temperature. End reflectors, designed to reduce radiative heat transfer from the ends of the sample, were incorporated, giving an increase of 10-15°C at the center of the sample.

   (ii) Reactivity Doppler Analysis. Preliminary results have been obtained for analysis of the natural UO_2 reactivity Doppler experiment in ZPR-3 Assembly 53. The method used involved RABBLE calculations of the change in Σ_a of the U-238 due to Doppler broadening; DIF2D (ARC system two-dimensional diffusion) calculations of fluxes in the sample and reactor; and PERT2D (ARC system two-dimensional perturbation) calculations of the change in k due to Doppler broadening of the U-238 resonances. No expansion corrections have been made, as Till at Argonne has shown that this effect is small for fertile oxide samples.

   Resolved resonance parameters were obtained from Schmidt,* and the basic cross sections were from the ANL-224 set. Resonance parameters in the unresolved region for U-238 were obtained statistically, using a chi-squared ($\nu = 1$) distribution for selection of neutron widths. The neutron widths were then randomly ordered over the energy interval of interest. Radiation widths and resonance spacing were assumed

---

*Schmidt, J. J., Neutron Cross Sections for Fast Reactor Materials, KFK 120 (February 1966).

constant. One selection of 60 resonances was used to determine broad-group cross sections for each group between the resolved resonance limit and 24.8 keV. Estimates based on the values of $\delta\Sigma_a$ between temperatures indicate that contributions from resonances above 24.8 keV would be less than one percent of the total change in k. Measured and calculated values for the reactivity worth of the change in Σ_a of U-238 are listed in Table I.B.4.

TABLE I.B.4. Comparison of Measured and Calculated
Doppler Effect for $^{238}UO_2$ in ZPR-3 Assembly 53

Temperature Change (°K)	Measured (Δk)	Calculated (Δk)
300-500	-(5.05 ± 0.05) x 10⁻⁶	-3.91 x 10⁻⁶
300-800	-(1.086 ± 0.05) x 10⁻⁵	-7.92 x 10⁻⁶
300-1100	-(1.550 ± 0.05) x 10⁻⁵	-1.09 x 10⁻⁵

Work is underway to repeat the above calculations with ENDF/B cross-section library and Schmidt's resonance parameters.

b.   Technique Development

(i) Study of Delayed-neutron Parameters. Program SPECB (which produces spectrum-weighted delayed-neutron parameters) has been completely checked by comparison with MACH-Bailiff using identical input data. The program has been expanded to include calculation of inhours/% Δk, and total fission neutrons produced.

(ii) Techniques for Control-rod Calibration. The two versions of program CROC (an inverse kinetics control-rod-calibration routine with a drift correction) with and without reactor-drift calculation have been combined into one program with user's option of performing either or both types of calculation. The use of drift correction appears to have a signifi-cant effect on calculation, whether or not the drift rate itself is significant. The difference between the two calculations for measurements made with ZPR-3 Assemblies 53 and 54 is illustrated in Table I.B.5.

TABLE I.B.5. Source Strength, k_{ex}, and Incremental Rod
Worths from Drifted and Nondrifted Calculations

	Q_ℓ	k_{ex} (x 10⁴)	10² Δk/k(%)
Nondrifted	0.691	3.201	4.507
Drifted	0.711	3.181	4.525
Nondrifted	0.693	3.611	4.929
Drifted	0.678	3.625	4.916
Nondrifted	1.035	2.898	3.833
Drifted	0.904	2.972	3.789
Nondrifted	1.015	2.470	3.387
Drifted	1.047	2.452	3.398

The results indicate that the reactivity increment is not appreciably affected, but the source strength and the final k_{ex} are more sensitive to the type of calculation. Thus the rod calibration is not adversely affected by neglecting the drift calculation, but the source value is. Generally, the drift correction is not desirable, unless substantial drift is present and data are obtained over a long enough time to make the total drift significant compared to the change in source worth during that time.

A source iteration procedure has been built into CROC which provides a small correction, of the order of 1% in 3 iterations. At this point convergence is completed.

Rod and source calibrations have been completed for ZPPR Assembly 1, and programs SPANE and IVY (inverse kinetics) have been converted to the IBM 360/75. A plot routine has been incorporated into SPANE to provide graphs of reactivity versus rod position.

A computer program (REDIC) has been written for the SEL 840 which will evaluate rod positions in terms of reactivity and calculate reactivity differences between settings on the 2 rods with position encoders. The calculation is based on the polynomial coefficients from SPANE.

b. <u>Mockup Studies</u>. Experiments with ZPPR Assembly 1 continued. This assembly corresponds to Assembly II of the FTR Resumed Phase-B Critical Experiments Program. As part of the Program, transition experiments are being performed with FTR-I before proceeding to the study of FTR-II. Reported herein are the transition experiments and the associated reactor operational measurements completed to date.

TABLE I.B.6. Reactor Inventory for Loading 1-17

Drawer Type	Number[a]	Fissile Mass[b] (kg)
Core:		
1-column plutonium	224	113.964
2-column plutonium	224	226.598
Safety	14	14.162
Control[c]	4	4.046
Poison	8	4.070
Radial Reflector	772	0.000
	Total	362.840

[a]Total for both halves of the assembly. Either assembly half contains 1/2 the stated value.
[b]Pu-239 + Pu-241 + U-235.
[c]Fissile mass includes two control drawers which were partially withdrawn, one 10.000 in. and the other 11.666 in.

(i) <u>FTR-I on ZPPR, As-built System</u>. The reference configuration for the FTR-I core is Loading 1-17. Reactor matrix and drawer loadings, as-built compositions, and fissile mass of Loading 1-17 were reported in ANL-7577. The total fissile mass (Pu-239, Pu-241, and U-235) of this reference configuration was reported incorrectly; the correct value is 362.840 kg. The reactor inventory for Loading 1-17 is presented in Table I.B.6. Figure I.B.6 depicts the equivalent cylindrical loading for the reference core, with the radii being derived from an equivalent cylindrical geometry having the same zonal areas as the actual loading.
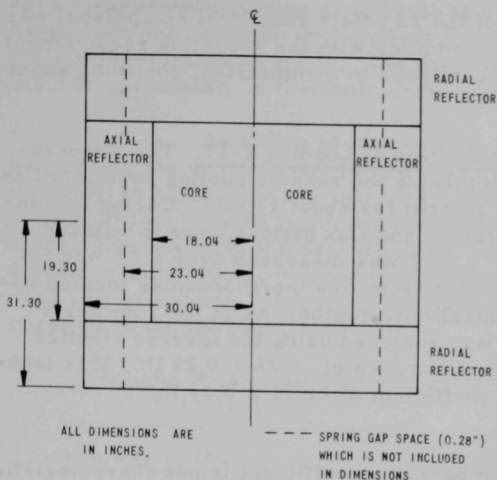
Fig. I.B.6

Equivalent Cylindrical Loading for FTR-1
Reference Loading of ZPPR (Loading 1-17)

(ii) <u>Calibrations of Control and Safety Rods</u>. Control and
safety rods were calibrated by the inverse kinetics method. Initially, the
effective neutron source due to the spontaneous fission of Pu-240 was de-
termined from three period-type measurements at power levels ranging
from 2 to 20 W. From a stabilized power level of approximately 250 W,
each rod being calibrated was individually driven from its most reactive
position to its least reactive and the resultant flux history recorded. The
flux history was analyzed using the delayed-neutron fractions given in
Table I.B.7 and the source term of 1.991 ± 0.163 obtained from the period
experiments.

TABLE I.B.7. Calculated Delayed-neutron Fractions for FTR-I on ZPPR

Group	β_i (U-235)	β_i (U-238)	β_i (Pu-239 + 241)	β_i (Pu-240)
1	1.8171 - 06	1.7951 - 05	5.9505 - 05	1.7121 - 06
2	1.0185 - 05	1.8918 - 04	4.3846 - 04	1.6693 - 05
3	8.9899 - 06	2.2370 - 04	3.3824 - 04	1.1740 - 05
4	1.9462 - 05	5.3578 - 04	5.1363 - 04	2.1401 - 05
5	6.1208 - 06	3.1070 - 04	1.6129 - 04	7.8267 - 06
6	1.2433 - 06	1.0357 - 04	5.4808 - 05	1.7732 - 06

Notes: β_{eff} = 3.0558 - 03; ℓ = 5.4592 - 07 sec; $Ih/\%\rho$ = 1.0391 + 03. A value
such as 1.8171 - 06 indicates 1.8171×10^{-6}.

The effect of source uncertainty on rod calibrations was
checked by evaluating rod calibration data utilizing source constants
modified by the standard deviation of ± 0.163 (8.2%). The resulting de-
viation in calculated rod worth was less than 1%, indicating little sen-
sitivity to source error.

The total worth of the 22 safety rods (fuel and poison) was determined as 3.97% $\Delta k/k$, which complies with the operating requirement of $\geq 1.5\%$ $\Delta k/k$. Worths of individual rods in symmetrical positions about the core center agreed to within 4%.

(iii) Temperature Coefficient of Loading 1-17. The temperature coefficient was measured by turning the reactor cooling system off and allowing the reactor power level to drift for about 17 min. During this interval, the resulting core temperature and flux history were monitored. A temperature difference of 2.86 ± 0.13°F was measured over a 17-min interval by averaging the data recorded from five thermocouples located between the matrix tubes in the central core region. As in the rod-worth determinations, the flux history was analyzed using the inverse kinetics technique and yielded a reactivity difference of -3.26 ± 0.23 Ih. This technique resulted in a temperature coefficient of -1.14 ± 0.27 Ih/°F (-2.05 ± 0.49 Ih/°C).

The resulting temperature coefficient is not characteristic of the core as an average, because of the temperature distribution measured. However, since the recording of the temperature is consistent throughout the experimental program, the coefficient can be appropriately applied to correct measured reactivity differences for temperature effects.

(iv) Measurements of Core-edge Worth. The worth of core drawers relative to reflector materials was measured at several core-edge positions in FTR-I. The reactivity effect resulting from these substitutions was measured by determining the position of the calibrated control rods necessary to maintain a power level of 50 W. Core temperatures were recorded and the temperature coefficient of -1.14 ± 0.27 Ih/°F used for applying the appropriate temperature correction.

The measured worths are listed in Table I.B.8. Each drawer worth was obtained from the difference between two measurements,

TABLE I.B.8. Edge-worth Measurements for FTR-I on ZPPR (Loading 1-17)

Matrix Position	Radius[a,b]	Fissile Mass[c] (kg)	Substitution			
			Worth of Core for Reflector		Worth of Reflector for Core	
			Ih[d]	Ih/kg	Ih[d]	Ih/kg
132-30	48.23	0.5088			20.55	40.39
130-32	48.94	0.5088			18.71	36.78
129-40	49.07	0.5088	18.91	37.17		
136-46	50.01	0.5088	18.26	35.89		
131-44	51.89	0.5088	15.33	30.13		
134-29	47.43	1.0116			48.92	48.36
133-45	49.83	1.0116	44.09	43.58		
128-37	51.96	1.0116	38.53	38.09		

[a]Equivalent cylindrical core radius of Loading 1-17 = 49.03 cm.
[b]Distance as measured from center of core central drawer to drawer center in given matrix position.
[c]Pu-239 + Pu-241 + U-235.
[d]Measurement uncertainty is ±0.91 Ih. This does not include the ±2% uncertainty in the control-rod calibration.

each measurement having an uncertainty of ±0.64 Ih. This uncertainty is based upon the reproducibility of the reference loading after accounting for temperature differences. The uncertainty, however, does not include the ±2% uncertainty in the control-rod calibration.

As shown in Table I.B.8, the specific worths were obtained by dividing the worth by the fissile mass to adjust for the two columns of fuel (1.0116 kg) in drawers located in odd-numbered matrix tubes and one column of fuel (0.5088 kg) in drawers located in even-numbered matrix tubes. Evaluation of the data indicated that this fissile-mass normalization did not completely account for the differences in the drawers containing one- or two-columns of fuel. A straight-line fit made for each set of data resulted in the following equations:

2-column Plutonium Drawers (1.0116 kg)	1-column Plutonium Drawers (0.5088 kg)
$\rho(\text{Ih}/\text{kg}) = 155.82 - 2.261 \ r(\text{cm})$	$\rho(\text{Ih}/\text{kg}) = 164.13 - 2.580 \ r(\text{cm})$

for 46 cm $<$ r $<$ 52 cm.

The average worth of core material relative to radial reflector material is the average of the two fitted equations. Evaluating this average worth at the equivalent cylindrical core radius of 49.03 cm gave 41.28 Ih/kg as the average conversion factor from core-edge fissile mass to reactivity.

(v) Critical Mass of FTR-I on ZPPR. The critical mass for FTR-I on ZPPR is summarized in Table I.B.9. Adjustments were made to the mass of the reference loading (1-17) to account for: (1) the partial withdrawal of Control Rods No. 3 and 4, and (2) the subcriticality of the reference loading at the reference power level (50 W) due to the high neutron source in the fuel. These corrections amount to -3.43 kg of fissile mass and result in a critical mass of 359.41 kg for the unsmoothed heterogeneous assembly. The average temperature of the core central region for this critical mass was 22.2°C.

TABLE I.B.9. Critical Mass of FTR-I on ZPPR

	Reactivity (Ih)	Pu-239 + Pu-241 + U-235 (kg)
Reference Loading (1-17)		362.84
Corrections to the Loaded Mass:		
1. Control Rods No. 3 and 4 Partially Withdrawn	-143.57	-3.48
2. Reference Core Subcritical at Reference Power Level	+2.11	+0.05
Critical Mass of the Unsmoothed Heterogeneous Cylinder		359.41

(vi) Subcriticality of ZPR-3/FTR-I Configuration. The FTR-I
critical configuration achieved in ZPR-3 (see Progress Report for February
1969, ANL-7553, p. 12) was rebuilt on ZPPR for the purpose of providing
an integral worth measure of the differences between ZPR-3 and ZPPR.
Within the normal limitations due to drawer lengths, material lengths, and
material inventory, the compositions used in ZPR-3 were reproduced as
closely as possible. An interface view of the rebuilt assembly is shown in
Fig. I.B.7. Drawer loadings* and zone compositions for this configuration
are the same as for FTR-I on ZPPR (see ANL-7577, pp. 40-41). Because
the ZPPR matrix has a larger void fraction than that associated with
ZPR-3, the rebuilt configuration was not expected to be critical on ZPPR.
This was proven to be true, and the degree of subcriticality was determined
as - \$3.29 ± 0.15 from the power-history method of reactivity analysis.

An interesting comparison is provided by summing the
worths of the core drawers comprising the difference between the FTR-I
critical loadings achieved on ZPR-3 and ZPPR. This difference consists of
37 core drawers having a total fissile mass (Pu-239 + Pu-241 + U-235) of
29.38 kg and radii ranging from about 46 to 49 cm. Utilizing the two edge-
worth equations corresponding to the two types of core drawers, and
neglecting any possible interaction effects, the worth of the 37 drawers
sums to - \$4.23. Accounting for the partial insertion of control rods in the
ZPPR critical configuration, the edge-drawer data indicate a subcriticality
of - \$3.78. Table I.B.10 depicts the 37 drawers and their individual con-
tribution as determined from the ZPPR/FTR-I edge-worth equations.

(vii) Addition of B_4C Control Ring and Enlargement of Radial
Reflector. The proposed FTR-II assembly is characterized by a B_4C con-
trol ring which separates the core and Ni-Na radial reflector. An approxi-
mate two-drawer-thick B_4C-Na ring was installed in the ZPPR/FTR-I
assembly just outside the predicted radius of the FTR-II critical
configuration. The loading of the drawers comprising the control ring is
illustrated in Fig. I.B.9, and an interface view of the loaded ring is shown
in Fig. I.B.10. The control ring is composed of 32.4 v/o B_4C,
32.4 v/o Na, 16.2 v/o stainless steel, and 19.0 v/o void, and contains
304.2 kg B_4C. The degree of subcriticality resulting from the addition of
the B_4C was measured using the power-history technique; the data are
being analyzed.

The thickness of the radial reflector surrounding the con-
trol ring was then slightly increased such that the control ring plus outside
radial reflector had an equivalent cylindrical thickness of 24.42 cm. The
resulting configuration is shown in Fig. I.B.11. By use of the power-history
technique, an attempt was made to evaluate the resulting reactivity change
due to the enlargement of the radial reflector. The data are being analyzed.

---

*The positions of the control and safety rods are identical in the ZPPR/FTR-I assembly and the ZPPR simulation
of the ZPR-3/FTR-I assembly. Because of a smaller core, the drawers adjacent to the outer poison rods in
the ZPPR simulation of ZPR-3/FTR-I contain radial reflector materials rather than core materials as in
ZPPR/FTR-I. The loading of these drawers is shown in Fig. I.B.8.
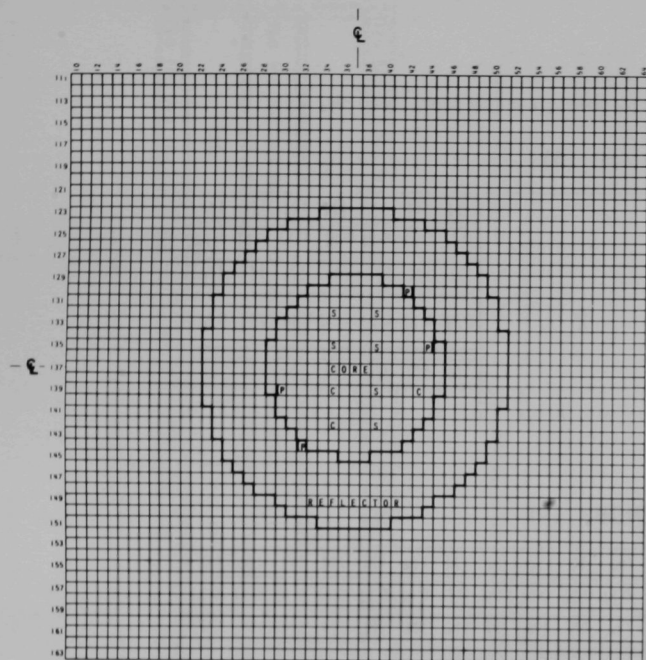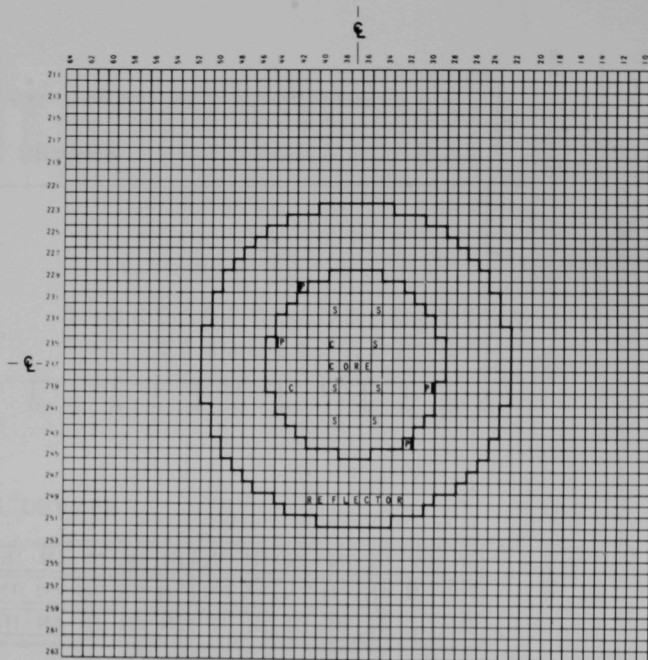
ZPPR HALF 1   ZPPR HALF 2

S = SAFETY ROD   C = CONTROL ROD   P = DRAWER ADJACENT TO POISON SAFETY ROD

■ = POISON SAFETY ROD (WITHDRAWN DURING OPERATION)

Fig. I.B.7. ZPPR Simulation of FTR-I Critical Configuration Achieved on ZPR-3 (ZPPR Loading 1-33)
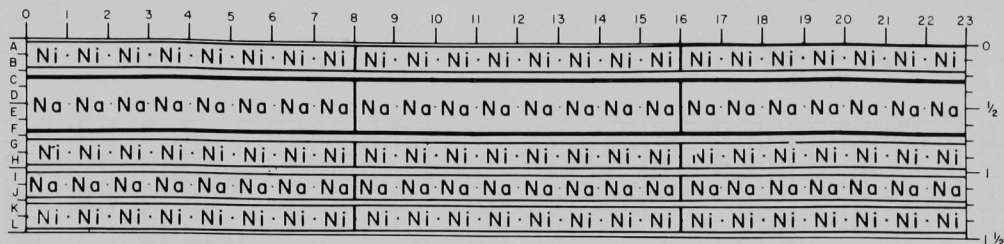
(a) FRONT DRAWER
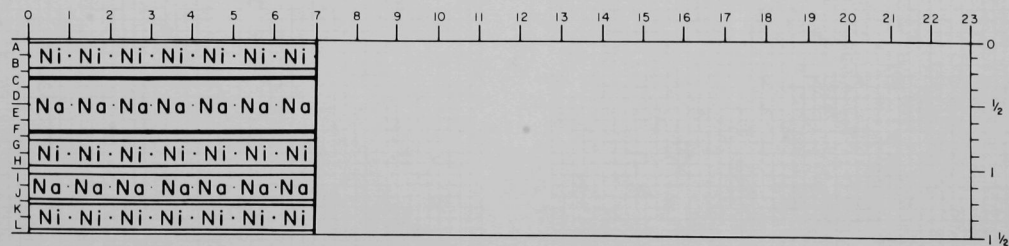
(b) BACK DRAWER

Fig. I.B.8. Radial Reflector Drawers Adjacent to Poison Safety Rod for FTR-I/II on ZPPR

TABLE I.B.10. Subcriticality of ZPR-3/FTR-I Configuration
As Determined from Edge-worth Measurements

Matrix Position	Radius (cm)	Pu-239 + Pu-241 + U-235 (kg)	Worth (Ih)
Half 1			
134-29	47.43	1.0116	49.14
140-29	47.43	1.0116	49.14
132-30	48.23	0.5088	20.20
142-30	48.23	0.5088	20.20
131-31	47.92	1.0116	48.02
143-31	47.92	1.0116	48.02
130-32	48.94	0.5088	19.26
144-32	48.94	0.5088	19.26
145-35	47.49	1.0116	49.01
145-39	47.49	1.0116	49.01
130-42	48.94	0.5088	19.26
144-42	48.94	0.5088	19.26
131-43	47.92	1.0116	48.02
143-43	47.92	1.0116	48.02
132-44	48.23	0.5088	20.20
142-44	48.23	0.5088	20.20
134-45	47.43	1.0116	49.14
140-45	47.43	1.0116	49.14
Half 2			
18 drawers corresponding to those in			644.50
Half 1 + 239-29	45.64	1.0116	53.24
		Total =	1342.24[a]

[a]Using 1039.1 Ih = 1% and β = 0.0030558, total worth of 37 drawers sums to $4.23.
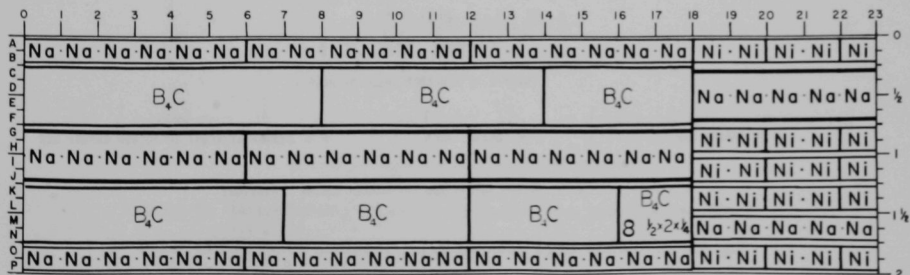
Fig. I.B.9. B₄C Control Ring Drawer for FTR-II on ZPPR
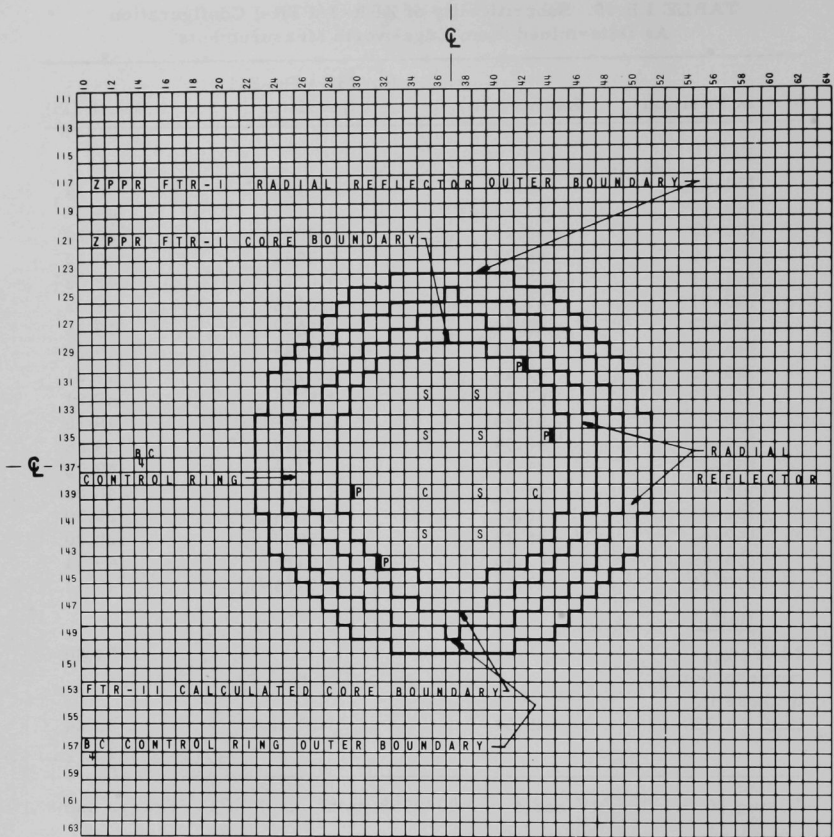
24

ZPPR HALF I

(HALF 2 IS A MIRROR IMAGE OF HALF I)

S = SAFETY ROD   C = CONTROL ROD   P = DRAWER ADJACENT TO POISON SAFETY ROD

▌ = POISON SAFETY ROD (WITHDRAWN DURING OPERATION)

Fig. I.B.10. Control-ring Placement during Transition from FTR-I to FTR-II
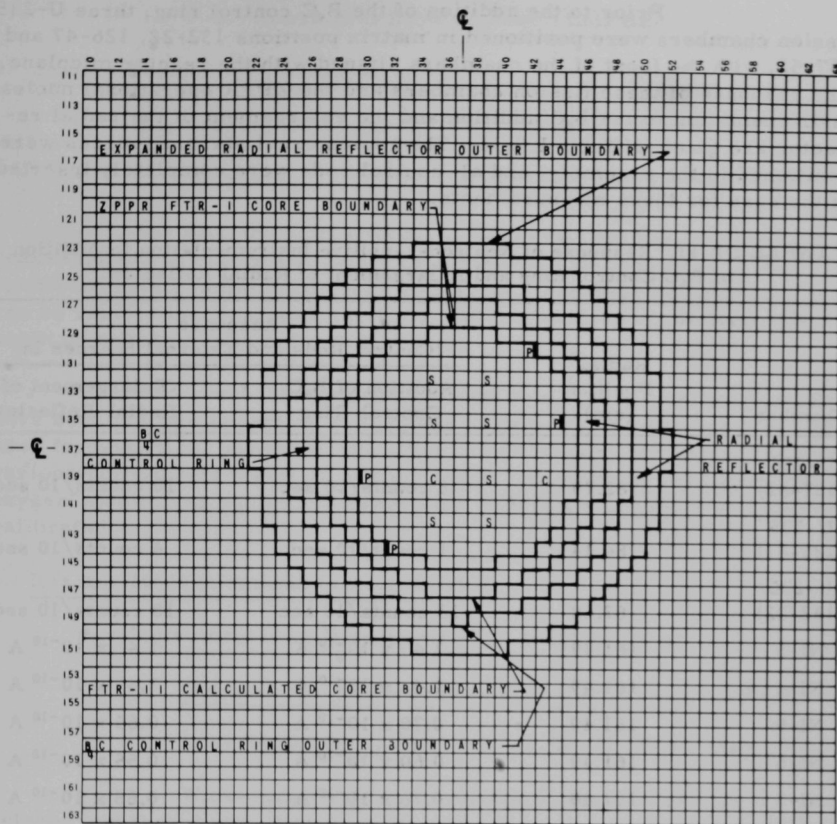
ZPPR HALF I

(HALF 2 IS A MIRROR IMAGE OF HALF I)

S = SAFETY ROD   C = CONTROL ROD   P = DRAWER ADJACENT TO POISON SAFETY ROD

█ = POISON SAFETY ROD (WITHDRAWN DURING OPERATION)

Fig. I.B.11. Radial Reflector Expansion during Transition from FTR-I to FTR-II

Prior to the addition of the B_4C control ring, three U-235 fission chambers were positioned in matrix positions 132-22, 126-47 and 137-52, with the front of the chambers aligned with the reactor midplane. The response of these fission chambers and the ZPPR operational nuclear instrumentation to the B_4C addition and the enlargement of the radial reflector are given in Table I.B.11. The two external startup sources were positioned in the assembly, and all control rods were completely inserted in the core for these measurements.

TABLE I.B.11. Response of Neutron-sensitive Instrumentation to Addition of B_4C Control Ring and Enlargement of Radial Reflector

Chamber	Radial[a] Position (cm)	Response (Control Rods and External Sources In)	
		Addition of B_4C Control Ring	Enlargement of Radial Reflector
U-235 (137-52)	82.79	8 counts/10 sec	10 counts/10 sec
U-235 (126-47)	84.14	1 count/10 sec	4 counts/10 sec
U-235 (132-32)	87.68	13 counts/10 sec	18 counts/10 sec
NI-3	161.49	1.4×10^{-10} A	1.4×10^{-10} A
NI-4	161.49	1.4×10^{-10} A	1.4×10^{-10} A
NI-5	161.49	0.70×10^{-10} A	0.65×10^{-10} A
NI-6	161.49	0.60×10^{-10} A	0.55×10^{-10} A
NI-7	161.49	0.76×10^{-10} A	0.68×10^{-10} A
NI-8	161.49	0.97×10^{-10} A	0.86×10^{-10} A

[a]As measured from center of central core drawer. The equivalent cylindrical radius of the outer edge of the enlarged radial reflector is 82.23 cm. The front of all the fission and operational chambers are aligned with the reactor midplane.

C. Component Development--LMFBR

1. Sodium Technology Development

a. Engineering Development (J. T. Holmes)

Last Reported: ANL-7577, p. 43 (April-May 1969)

The SAL (Sodium Analytical Loop) facility has been completely reassembled. A safety analysis was completed and presented to the divisional safety committee. It is anticipated that their recommendations can be readily incorporated into SAL, and that startup of the loop will begin on schedule (about the end of June).

Two evacuable gloveboxes with atmosphere-purification systems have been put into operation and appear to be working satisfactorily. One is used for analytical purposes; the other, much larger, can be used to examine various components taken off sodium loops. At present, the moisture- and oxygen-monitoring equipment associated with these gloveboxes is being calibrated.

2. Reactor Mechanism and Instrumentation

a. Instrumentation Development (T. P. Mulcahey)

(i) Out-of-core Neutron Flux Detection System (G. F. Popper)

Last Reported: ANL-7577, pp. 43-46 (April-May 1969).

Wide-range and intermediate-range circuits are being developed and tested with detectors installed in a special thimble in EBR-II. Environment and performance requirements for FFTF and future LMFBRs serve as development and test goals so that suitable neutron-flux measurement systems will be available for such reactors.

(a) Detectors and Cables. Another sample of a reworked Westinghouse WX-31353-25 cable assembly was tested up to 700°F in air. This cable performed similarly to the cable tested last month, except that this assembly failed due to voltage breakdown with 500 V dc applied after only about 24 hr of operation at 700°F in air compared to 150 hr for the first sample. All four of the Westinghouse cables have been returned to the manufacturer for evaluation and modification of the end seals and connectors.

The Electronic Specialties Co. (ESC) cable assembly was tested up to 500°F in air, at which point failure due to voltage breakdown upon application of 500 V dc occurred. As was the case with the Westinghouse cable, the point of breakdown was the connector end. The hermetic

seal on the end of the ESC cable assembly also failed after this relatively short time at a modest temperature. The ESC cable had an almost constant capacitance of 27.3 pf/ft at all test temperatures up to 500°F with either 1 kHz or 1 MHz applied. The dc insulation resistance varied with temperature as shown in Fig. I.C.1. Above 500°F, the cable could hold only 300 V dc or less without the breakdown phenomenon occurring. No further work is planned with the ESC cable assembly.
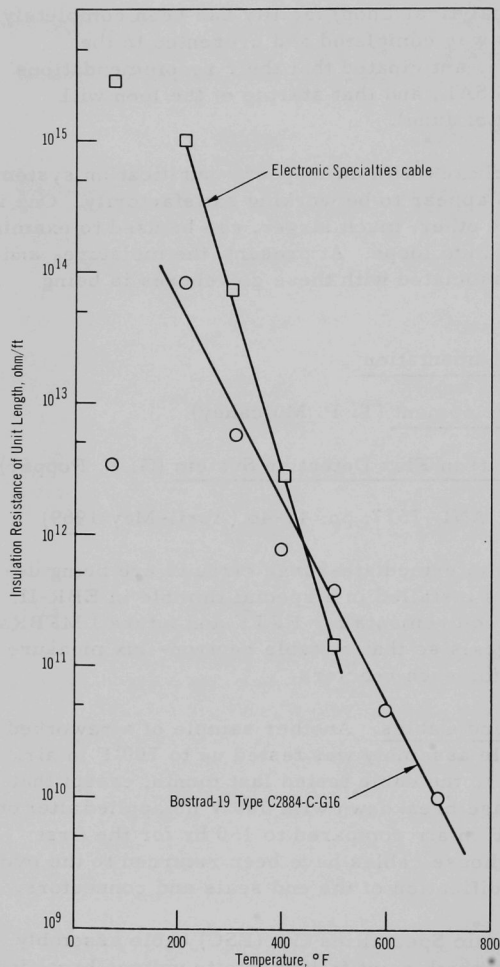
Fig. I.C.1. Variation of Insulation Resistance with Temperature for Several Cables

Both the Westinghouse and ESC cables were vacuum-baked and backfilled with dry nitrogen after the seals failed to see if the breakdown was caused by moisture entering the cable after the hermetic seal had broken. The use of dry nitrogen did significantly improve the room- and low-temperature resistance characteristics of the insulation. However, the use of dry nitrogen did not improve the breakdown characteristics of either cable in any way at high temperature. Therefore, it is considered that the small amount of moisture present in the air at temperatures above ~300°F does not degrade cable performance significantly.

Three samples of Boston Insulated Wire Co. Bostrad-19 cable are being tested: C2884-C-G16, 6060-C-G16, and 7448-C-G16. The C2884-C-G16 cable is a coaxial type consisting of nickel-clad copper inner conductor and outer shield braid with a braided-glass insulation. The 6060-C-G16 cable is the same except that an extra outer glass braid is wrapped around the outer shield. The 7448-C-G16 is the 6060-C-G16 with an additional nickel-clad copper shield wrapped with mica tape and glass-braid outer covering, making it a triaxial cable.

All three samples have been tested up to 700°F in air. No connectors have been attached to the hot end, however. The variation of insulation resistance with temperature for the C2884-C-G16 cable is shown on Fig. I.C.1. The low apparent insulation resistance at room temperature is due to absorbed moisture in the as-received condition. At temperatures above about 200°F, the moisture is driven out and the insulation resistance improves significantly. This insulation-resistance characteristic with temperature was duplicated almost exactly by the 6060-C-G16 coaxial and 7448-C-G16 triaxial cables.
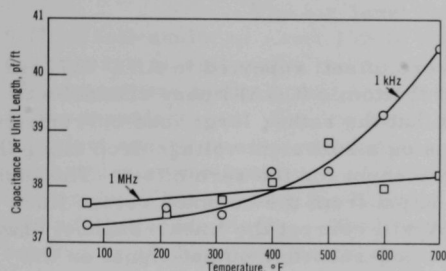
Fig. I.C.2. Variation of Cable (Bostrad-19, Type C2884-C-G16) Capacitance with Temperature and Applied Frequency. Test conducted in air.

Figure I.C.2 shows the changes of C2884-C-G16 cable capacitance with temperature. This characteristic is typical of glass-, quartz-, and mica-insulated types of cable. Very little change in capacitance is noted when 1 MHz is applied, but significant changes are noted at low frequencies (1 kHz), where polarization effects are more pronounced at high temperature. For some reason, possibly lot of manufacture, the C2884-C-G16 cable had a slightly higher (37.3 pf/ft) capacitance than did either the 6060-C-G16 or the 7448-C-G16 cables (32.6) pf/ft). The 6060-C-G16 cables are so similar in performance that only physical-size identification could be used to tell the cables apart during the test.

All three cables were able to withstand 500 V dc in 700°F air initially, but the 6060-C-G16 and 7448-C-G16 cables were very marginal. Breakdown of these two cables began at about 530 V dc. The C2884-C-G16 cable was able to withstand at least 800 V, the maximum applied, without any evidence of breakdown. All three cables were soaked in 700°F air for more than 2 weeks (340 hr). The insulation resistance of all cables improved only slightly during this time, and the capacitance did not change. The C2884-C-G16 cable can still take at least 800 V, the maximum applied, while the 6060-C-G16 and 7448-C-G16 are breaking down at about 450 V dc. The superior performance of the C2884-C-G16 cable is surprising because this cable is the base for the other two types. The only explanation at this time, even after discussions with the manufacturer as to possible variations in processing, is that a looser weave was achieved on this sample, giving better dielectric properties. However, this explanation is not supported by the higher measured capacitance of this cable, which indicates a firmer weave. Although these differences should be resolved, it might not be possible to do so if they are related to in-plant processing. By far, these

cables are performing better than any others tested to date in terms of their ability to hold high voltage with minimum or no breakdown. None of these cables are or have been sealed from the moisture in the air, so these test results also support the conclusion that residual moisture at 700°F is not a serious problem.

The detector-cable test programs at both Reuter-Stokes and Westinghouse have encountered delays because of cable-assembly defects as a result of testing. Neither program was completed this month as had been expected originally.

(b) Circuits. The zero offset, reported in ANL-7577, in the recorder output of the Gulf General Atomic (GGA) linear channel was isolated and corrected. It was found that the rather large load currents from the bistable trip amplifiers were causing a sufficient voltage drop along the common power-supply return line to account for the zero offset. The isolation of the linear-channel amplifier output from the common return line solved the zero-offset problem. GGA will correct the linear-channel drawings to reflect these changes. The period-recorder output signal on the wide-range channel was similarly isolated from the common return line.

The recorded response of the GGA linear channel now indicates a perfect one-to-one correspondence with the EBR-II linear channel without any correction. The linear-channel recorder output signal varies by $\pm 1.1\%$ of full scale at constant reactor power and exactly agrees with the variation in the EBR-II linear-channel recorded signal. Data now indicate that the recorded period signal is fluctuating around plus and minus infinity when the reactor is running at constant power, as would be expected, and not around an approximately positive 150-sec period as found from previous data due to the zero offset. Therefore, it is apparent that the problem with the period-recorder-signal zero offset has been solved.

An analog recording of the GGA log-countrate (LCRM) and log campbelling (LAMS) output signals taken during a reactor shutdown showed that the slope of the LCRM and LAMS recorder output curves were not the same, but they should be. As the LCRM output was checked against calibration signals just prior to the shutdown, it is assumed to be correct. Therefore, it is deduced that the LAMS-recorder output signal has either drifted out of calibration during the past year or was never adjusted correctly in the first place, due to the large noise signals originally present. This misalignment is probably the reason that little, if any, overlap appeared to exist between the LCRM and LAMS signals as recently reported. Actually, an overlap of about a decade and a half can probably be achieved, as is indicated by the new data. A slope and bias adjustment of the LAMS-recorder output was made, and the overall signal level increased by a factor of ten. The LCRM signal level was increased by a factor of ten at the same time. The noise in the recorded LCRM output signal is now less

than ±0.06% of full-scale, or ±1.1% of the reading in the clamped condition, and is a true indication of residual system noise. The LAMS recorded output signal varies by less than ±5% of the reading, or ±0.3% of full-scale at a constant reactor power. Surprisingly, the slope of the LAMS output signal is still in error by a measurable amount. The cause must be investigated because the slope misalignment was adjusted less than 10 days before the data were taken. However, it is clear that the erratic LCRM- and LAMS-recorder output signals no longer exist.

The log-level slope was reported to be off by about 0.7% of full-scale, or about 15% of the reading; however, the 0.7% of full-scale error is well within the specification for this channel. A slope adjustment was made to the channel using revised calibration data supplied by the manufacturer. The log-level output of the GGA channel now indicates a perfect one-to-one correspondence with the EBR-II linear channel. The largest deviations found were less than ±9% of the reading, or about ±0.4% of full-scale. This is about the limit of precision that can be expected from this type of 10-decade display. The log-level signal varies less than ±5% of the reading or ±0.2% of full-scale, at constant reactor power.

To reduce further the stray noise signals being injected into the system on the shielded twisted pairs recommended by the manufacturer, all signal cables between the preamplifier and the channel electronics were changed to coaxial cables. In addition, flexible conduit was placed around these cables from the preamplifier to the junction box at the reactor-building penetrations. These changes significantly reduced the noise at the preamplifier output. The primary noise eliminated was 60 cycles (22 to 6 mV rms) being injected on the ±15 V lines.

As a result of the cable changes, channel alignment, and recorder output signal level increases made recently, the GGA 10-decade neutron monitor is performing adequately. More reactor startup data are urgently needed to evaluate fully the effects of these improvements on channel performance.

b.   FFTF Instrumentation (R. A. Jaross)

(i)   In-core Flowmeter Development (for FFTF)

Last Reported: ANL-7577, pp. 47-50 (April-May 1969).

(a)   Flow-sensor Feasibility Studies. A static sodium tank and bellows testing rig was modified for droptests of probe-type flowsensors in high-temperature sodium.

A number of drops in air were made to check the mechanism and velocity-measuring system. Although the drop mechanism is

a free device, the spring-loading effect of the three bellows when they are expanded provides an initial acceleration greater than that due to gravity. The drop tube moves approximately 26 in. downward before the shock absorbers are contacted. The velocity-measuring system uses a magnetic pickup that moves with the drop tube past a series of $10/32 \times 2$-in. steel machine screws equally spaced 3 in. apart over a 24-in. span. Other components of the system include: a decade amplifier that also functions as a limiter between the magnetic pickup and the first-pulse generator, two pulse generators in cascade to modulate the grid or cathode of an oscilloscope with a known time base as an indicator, and a scope camera to obtain a single-sweep picture from which data can be obtained for use in calculating the average velocity between the 3-in. points of the drop-tube excursion. In air, the drop through 24 in. takes 245 msec; the average velocity of the last 6 in. is 11.1 ft/sec.

The drop mechanism has been installed over the sodium tank. Although the velocity-measuring equipment has not yet been connected, several drops in sodium appeared to be slightly slower than in air. The speed might be improved by evacuating the sodium tank partially.

Three identical Inconel coil forms have been made for the eddy-current probe. One coil form, designated No. 2, has five coils coaxially located as Pri. #1, Sec. #1, Pri. #2, Sec. #2, and Pri. #3. Each coil has 410 turns (± one turn) of 16-mil 20%-silver wire that is clad with nickel and coated with ceramic. All coils are $7/16$-in. ID x $29/32$-in. OD x $1/2$-in. wide, and each is spaced coaxially by a solid $1/16$-in.-thick Inconel spacer. The three primary coils are connected in opposing series to give a radial-flux field in each secondary. The two secondary coils are connected in aiding series. This coil assembly has been tested in the oscillating test mechanism with a $1/32$-in.-wall Type 304 stainless steel tube over the coil assembly and moving in unison with it inside a 2-in. OD x 1-in. ID 6061T6 aluminum tube. With 2.09-ft/sec peak velocity and 300-mA rms primary current, a 24-mV peak-to-peak maximum signal was obtained from the secondaries with frequencies from 150 to 180 Hz. The sensitivity is about 10% more than expected. This coil assembly is being coated with ceramic, filled, and cured; it should be useful to at least 1000°F. It will be the first coil tested in the droptest rig.

A second Inconel coil form, designated No. 3, was wound identically to No. 2 except that the two secondary coils each have approximately 1550 turns of ceramic-coated copper wire of 5-mil diameter (AWG36). This coil assembly is being tested in the oscillating test apparatus, but sensitivity measurements have not yet been made. This probe, which should be useful to 800°F, was made as a backup probe for No. 2.

Leads from the top of the drop-test apparatus down to the coil assembly will be two twisted pairs of fiberglass-insulated copper

wire of 32-mil diameter (AWG20); each pair will be in a 1/4-in. Type 304 stainless steel tube lined with fiberquartz sleeving.

We have obtained one sample piece of Supramica-620, a machinable ceramic, large enough for a five-section coil form as No. 2 above. A ceramic coil form will simplify the insulation problem.

The fabrication of the three different permanent-magnet, solid-configuration, 1-in.-OD, cylindrical flow-sensor designs is nearing completion. The components are ready for final assembly and welding. When inserted and welded in the end of the flow-sensor cylinder, the end bushing will be welded to a 1-in.-OD, 13-ft-long tube as required for droptests in the sodium tank.

The lead end of the flow sensors will be modified later for tests in an existing low-temperature, 30-gpm sodium loop (being modified as a backup to the droptest tank) and/or the 250-gpm CAMEL loop.

(ii) Failed-fuel Location Method (E. S. Sowa)

Last Reported: ANL-7577, pp. 51-52 (April-May 1969).

(a) Gas-disengagement Tests. High-speed (8000 frames/sec) photographs were taken of gas bubbles injected into water flowing at 0, 1, 2, 6 and 10 ft/sec. These photographs were taken in the glass test apparatus constructed for studying the gas injection. The gas-injection region was an exact replica of the injection-capsule configuration in the Fuel Failure Detection Loop (FFDL).

Analyses of the films show that bubble size depends strongly on the velocity of the fluid moving in the channel. Bubble size ranged from <1.0 mm at 10 ft/sec to ~1.5 cm at 0, 1, and 2 ft/sec. Thus, because low-flow tests in the FFDL would not be meaningful unless proper fragmentation of bubbles is effected, the low-flow tests have been postponed until a proper bubble-fragmentation system is installed in the loop.

To attempt fragmentation of the injected gas into small bubbles, cavitation produced by ultrasound was attempted in the water system. For this, a 500-W magnetostrictive transducer was connected with an exponential horn to a quarter-wavelength double-cantilever resonator. One end of the resonator protruded into the interior of the flow channel and also supported the injected capsule. The gas was admitted through a hollow channel along the central axis of the resonator. With approximately 500 W of excitation supplied to the transducer at 25 kHz, tests with water flowing at 2 ft/sec showed no fragmentation of the gas (although outgassing of the water provided evidence of ultrasound input).

A second method for bubble fragmentation was tried. It employed a venturi restriction above the point of gas injection. A plastic venturi, whose throat was roughened to produce high turbulence, was constructed and tried in the water system. The tests were successful. Bubble fragmented into sizes of < 1.0 mm with water velocities of 1 and 2 ft/sec. Thus a stainless steel venturi insert is being constructed for installation in the FFDL.

c.   EBR-II In-core Instrument Test Facility (E. Hutter)

(i)   Preliminary Study of Various Concepts (O. S. Seim, T. Sullivan, and J. Pardini)

Last Reported: ANL-7577, pp. 52-53 (April-May 1969).

Evaluation of various concepts of instrument test thimbles has continued. Most of the effort has been devoted to the concept in which cooling is accomplished with primary-tank bulk sodium and the ambient primary sodium serves as a heat sink.

Temperature calculations were made for an open bundle of typical instruments (thermocouples) in an argon environment in the EBR-II core. The results of the calculations showed that the gamma heat generated within the instruments must be dissipated primarily by thermal radiation and that the resultant high temperature levels when the clearance between the sensor and the thimble is large may preclude performance of some desirable tests. Therefore, further calculations were made for a concept of multiple sensor thimbles. The results of these calculations indicated that the maximum temperature of a typical thermocouple can be varied from about 850°F to over 1300°F if appropriate flow control can be achieved.

The results of preliminary hydraulic calculations indicated that the pressure drop in the thimble coolant passages is high enough to make use of the coolant flow from the reactor high-pressure inlet plenum desirable. This applies when using one or more of the larger sensor tubes or a number of the smaller sensor tubes. The results of the hydraulic calculations also showed that, because the test heat load within the thimble is small compared to the heat load of the thimble hardware, the flow-control device can be used with a variety of thimble configurations.

3.   Fuel Handling, Vessels, and Internals--Core Component Test Loop (CCTL) (R. A. Jaross)

Last Reported: ANL-7577, pp. 53-54 (April-May 1969).

Although the valve and its associated inlet pipe have been removed for more complete examination, the exact cause of the sodium leakage associated with the CCTL cold-trap sodium throttle valve has not been yet determined.

a.   Material-property Measurements

Preliminary measurements of tensile strength, yield strength, and percent elongation have been made of 2-in. and 4-in. pipe removed from CCTL. The 2-in. sample tested was from near the 2-in. failed valve, but was sound pipe unaffected by the corrosion products produced by the leak; the 4-in. pipe was removed from the CCTL pump outlet adjacent to the electro-magnetic flowmeter. The properties are well within the statistical range of data in MSA-69-42 for material that had been exposed to 1200°F sodium (CCTL was at 1060°F).

The behavior of the Type 304 stainless steel aircraft cable dis-cussed in ANL-7577 is peculiar to the hard-drawn, high-tensile strength, finely stranded aircraft cable. The piping of CCTL is not affected by sodium to increase brittleness and reduce tensile strength as was the aircraft cable. These preliminary measurements serve as the basis for proceeding with other CCTL mechanical work.

D.   Systems and Plant--LMFBR

1.   1000-MWe Plant

a.   Contract Management, Technical Review, and Evaluation
(L. W. Fromm)

Last Reported: ANL-7561, pp. 24-25 (March 1969).

All work by the contractors has been completed except for the publication and transmittal of two documents (Task-IV reports from Babcock & Wilcox and Atomics International) both of which are in the process of publication.

Patent clearance has been received on the Task-II, -III, and -IV reports of General Electric, which were released for publication and external distribution.

A plan has been developed for the evaluation of all reports from the contractors, and the technical specialists are evaluating the documents. A few evaluations have been drafted and are being reviewed.

E. EBR-II

1. Research and Development

a. Reactor Experimental Support--Reactor Analysis and Testing
(R. R. Smith)

(i) Nuclear Analysis and Safety

Last Reported: ANL-7577, pp. 61-64 (April-May 1969).

(a) Design and Initial Calibration of Stainless Steel Drop
Rod (R. W. Hyndman and J. K. Long)

A stainless steel drop rod has been in use in control-
rod location No. 1 to provide a small, prompt reactivity step for kinetic
studies. The rod contains a 12-in.-long stainless steel rod bundle which,
when dropped out of the core, removes reactivity in the pattern described
by Hyndman and Nicholson.* Since the velocity of the rod is slow at the
start and at the end of the rod travel, the removal of reactivity was spread
out over about 250 msec, with a slowly varying tail at each end. Subsequent
inverse kinetics interpretation of the resulting power traces was limited to
time constants of the order of 1/4 sec because of the distribution of reac-
tivity changes during the drop.

A redesigned rod bundle or group of bundles therefore
was sought in which reactivity changes of various segments would cancel
each other during the low-velocity portions of the rod travel. Effective
reactivity changes would then take place in a shorter time interval, and the
rod drop would more closely approximate a step change in reactivity.

The worths of substitutions of stainless steel for so-
dium at a central-rod location were taken from ZPR-3 critical-assembly
data.** After the data were modified to account for the fact that the ZPR-3
data were taken with a mockup of somewhat different size than the present
EBR-II configuration, the curve shown in Fig. I.E.1 was adopted to repre-
sent the worth of the substitution.

The constraints and conditions placed on the redesign
of the rod were as follows. The lower adapter was to remain unchanged, the
position and length of the rod bundle could be changed, the position of the
upper follower could be changed, and one additional follower of undetermined
length and position, but having the same density as the rod bundle, could be
inserted.

---

*Hyndman, R. W., and Nicholson, R. B., The EBR-II Feedback Function, ANL-7476 (July 1968).
**Keeney, W. P., and Long, J. K., Idaho Division Summary Report for July, August, September 1960,
ANL-6301.
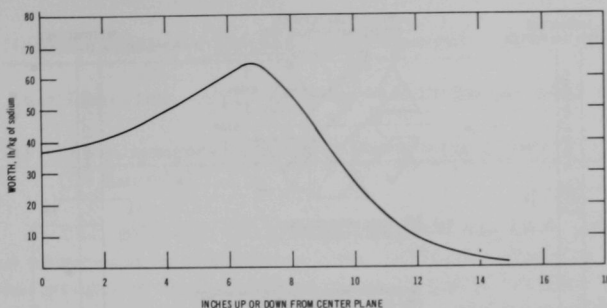
Fig. I.E.1. Worth of Stainless Steel Substituted for Equal Volume of Sodium
(9 kg of stainless steel = volume of 1 kg of sodium = 1150 cc;
radius = ~8.2 in.; reactor assumed to be symmetrical about
center plane)

With the options open on the lengths and positions of
the stainless steel segments of the rod, there are a large number of com-
binations whose pattern of worth could be investigated. A computer survey
of worth patterns therefore was carried out to select those patterns which
produced negligible reactivity changes in the first and last few inches of
travel, avoided any positive pulse, and had a total worth large enough to
allow meaningful analysis. The survey led to the selection of the rod shown
in Fig. I.E.2. The rod was designed to be dropped from 13 in. rather than
the full 14 in. so that possible asymmetrics in flux could be compensated
for by making slight adjustments in drop height.

A rod with the features shown in Fig. I.E.2 was fabri-
cated, and was installed in Run 35. The orifice was designed for a low
coolant flow (4 gpm) to reduce temperature gradients between the rod and
adjacent subassemblies.

Preliminary calibration of the new rod was done by
rod-drop methods. The results of the calibration are shown in Fig. I.E.3
together with the calibration predicted from the critical-experiment data.
Although the critical experiment seems to predict a higher worth, the dis-
agreement in scale is not surprising in view of known differences between
the geometry of the critical assembly and of EBR-II as of now. The 6-Ih
total worth of the rod is expected to be sufficient for analysis of the rod-
drop experiments. The general shape of the measured calibration is con-
sidered very satisfactory because it indicates that reactivity changes are
effectively confined to rod positions ranging between 3 and 8 in. from full
insertion, a region traversed by the rod in less than 90 msec.
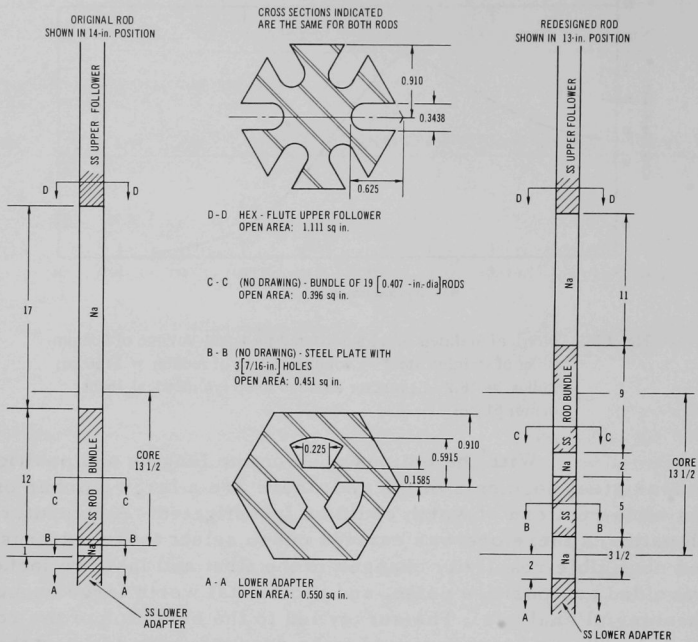
Fig. I.E.2. Comparison of Design Features of Original and Redesigned
Stainless Steel Drop Rods (all dimensions are in inches)
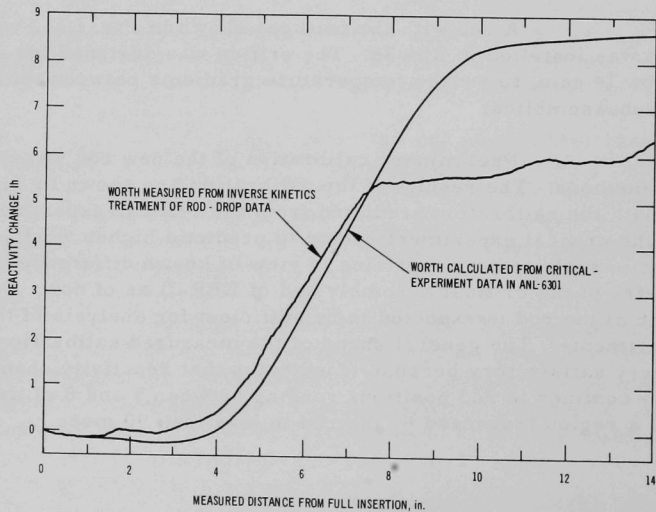
Fig. I.E.3. Measured and Calculated Worths of Redesigned Stainless Steel
Drop Rod as a Function of Distance from Full Insertion

b. Nuclear Analysis Methods Development

Last Reported: ANL-7577, pp. 64-75 (April-May 1969).

(i) Developments in Bowing Programs BOW-IV and BOW-V
(D. Kucera)

The BOW-IV CDC-3600 program has been completed. This program, the successor to the bowing code BOW-III, contains an iterative procedure that produces final configurations in complete load equilibrium. With this improved procedure, BOW-IV becomes the first of the bowing programs to reflect the chosen physical bowing model truly. BOW-IV has been tested for input values corresponding to power levels ranging from 0 to 135 MW in EBR-II Run 25.

BOW-IV contains the assumption of incompressibility of all subassembly tops regardless of imposed loads, which requires an extensive amount of complex programming. Since incompressibility formally may be considered a special case of compressibility, the less complex conditions for compressibility are equally useful. These conditions, more general and simpler, were incorporated into the program to provide a version designated BOW-V.

BOW-V is nearly a third shorter than BOW-IV, operates more rapidly, and is in total agreement with BOW-IV for the incompressible-top case of EBR-II Run 25. BOW-V requires about 1.6 sec per iteration, with convergence attained in 11 iterations in the worst case studies so far and about four iterations for a typical case. Debugging of BOW-V through drastic variations in input has begun.

(ii) Reactivity Effects of Utilizing Space-energy-weighted
Multigroup Cross Sections for Nickel- and Steel-reflected
EBR-II Type Systems (D. Meneghetti and K. E. Phillips)

The comparative reactivity effects of utilizing various numbers of spatially dependent coarse cross-section sets to simulate fine-energy spatially dependent analysis of EBR-II type systems have been calculated. The spatially dependent fine-energy-detailed neutron-flux spectra for the simulated applied source solutions were discussed in ANL-7577, pp. 69-73, which also showed the effects of various numbers of collapsed coarse-group sets on the corresponding coarse-group leakages from core to reflector. In the calculations, the energy range from 2.1 keV to 1.35 MeV, comprising the region of the resonance-scattering effects, was subdivided into fine-energy groups. The systems calculated simulated an approximate core composition of the EBR-II radially surrounded by 25 cm of either nickel-rich or stainless steel-rich reflector followed by essentially a

depleted-uranium blanket 10 cm thick. The 25-cm-thick reflector consisted of two regions, one 10 cm and the other 15 cm thick, with the inner region having a higher sodium content. In the case of the nickel-rich reflector, the approximate atomic densities for the two regions, respectively, in units of 10^{24} atoms/cm, are (1) sodium, 0.003; nickel, 0.073; and stainless steel, 0.006; and (2) sodium, 0.0016; and nickel, 0.085. For the stainless steel-reflected case, the approximate atomic densities for the two regions are (1) sodium, 0.003; and stainless steel, 0.074; and (2) sodium, 0.0016; and stainless steel, 0.080.

The fine-energy-detailed neutron-flux solutions described in ANL-7577 were used together with the corresponding fine-energy-detailed currents as weighting factors in space-energy collapse of fine cross-section detail to coarse-group cross sections. The fine-detailed energy range from 1.35 MeV down to 2.1 keV was collapsed into eleven half-lethargy intervals and one interval of unit lethargy.

Collapsed coarse-group cross sections corresponding to each of 63 mesh positions in the one-dimensional cylindrical system, to each of 11 subregions (three in the core, three in each of the two reflectors, and two in the blanket) and to four mesh positions (at the center of each of the four regions) were utilized to calculate source-iterative (i.e., k_{eff}) coarse-group solutions.

For comparison, corresponding source-iterative results were obtained through a simplified approach based on the assumption of fundamental mode in the core and of zero buckling in other regions. In this approach, collapsed cross sections were derived by using (1) an assumed, simplified central-point fine-flux solution as a cross-section weighting spectrum for the entire core region and (2) simplified zero-buckling fine-flux solutions as cross-section weighting spectra for the two reflector regions and the blanket region. The extent to which the results obtained by this simplified approach compares with the results obtained by use of 63 coarse-group sets is a measure of whether extensive space-energy analysis is required for a given situation.

Estimates of deviations in reactivity resulting from use of the various set approximations relative to the use of 63 cross-section sets are listed for the two systems in Table I.E.1.

TABLE I.E.1. Percent Deviation in Reactivity
with Number of Cross-section Sets[a]
(coarse-group calculation)

System	11 Sets	4 Sets	4 Sets[b]
Ni-rich Reflected	0.00	-0.10	-0.16
SS-rich Reflected	0.00	-0.11	-0.34

[a]Relative to use of 63 cross-section sets: $[(k - k_{63})/k_{63}] \times 100$.
[b]By approach using simplified weighting.

(iii) Worth of Nickel Reflector (B. R. Sehgal)

A set of calculations was made for ZPR-3 Assembly 6F to gain information on the expected worth of a nickel reflector in EBR-II.

The reactivity of ZPR-3 Assembly 6F, which is similar to EBR-II in composition and size, was calculated first for the cases of a depleted-uranium blanket and of a nickel reflector containing 80 v/o nickel, 7 v/o stainless steel, and 13 v/o sodium. The compositions and sizes of the core and the blanket (or reflector) regions used in the calculations are given in Table I.E.2.

TABLE I.E.2. Specifications for ZPR-3 Assembly 6F

Geometry: Sphere
Radius of Region 1 (core): 22.995 cm
Radius of Region 2 (blanket): 53.495 cm

| Isotope | Region Compositions (atoms/b-cm) | | |
	Core Region 1	Depleted-uranium Blanket Region 2	Nickel Reflector Region 2
^{235}U	0.006727	0.000089	-
^{238}U	0.007576	0.040026	-
^{234}U	0.000069	-	-
Al	0.019019	0.001359	-
Fe	0.007712	0.004539	0.004305
Cr	0.001918	0.001129	0.001134
Ni	0.000839	0.000494	0.073557
Mn	0.00008	-	-
Na	-	-	0.003302

The broad-group cross sections for the core material, the depleted-uranium blanket, and the nickel reflector were obtained through the code MC²* using the ENDF/B data. Zero buckling was assumed for the depleted-uranium blanket and the nickel reflector, and critical buckling for the core material. The SNARG-1D code** was used to calculate the reactivity, and the model of the ZPR Assembly 6F was assumed to be a homogeneous two-region sphere.

The results of the calculations of reactivity are reported in Table I.E.3. For this simple system, the calculated worth of the nickel reflector is $\simeq 4.26\%$ higher than that of the depleted-uranium blanket.

---

*Toppel, B. J., Rago, A. L., and O'Shea, D. M., MC², A Code to Calculate Multigroup Cross Sections, ANL-7318 (1967).
**Duffy, G. J., et al., SNARG-1D, A One-dimensional, Discrete-ordinate, Transport-theory Program for the CDC-3600, ANL-7221 (1966).

TABLE I.E.3. Results of Reactivity Calculations
for ZPR-3 Assembly 6F

System	k_{eff}
With Depleted-uranium Blanket	1.00884
With Nickel Reflector	1.05141
	Δk_{eff} = +0.04257

(iv) Two-dimensional Spatial Variation of Fission Rate in
EBR-II (L. B. Miller and R. E. Jarka)

The EBR-II core loading is changed, on the average, every
ten days. These changes represent insertion, removal, and relocation of
metal-driver-fuel subassemblies, oxide and carbide experimental-fuel
subassemblies, fertile-blanket subassemblies, structural-material experi-
ments, and other experiments and instrumentation.

d – Driver Fuel
C – Control Rod
X – Experiment
S – Safety Rod
½ – ½ Loaded Driver
R – Replacement
Locations for
Calculations
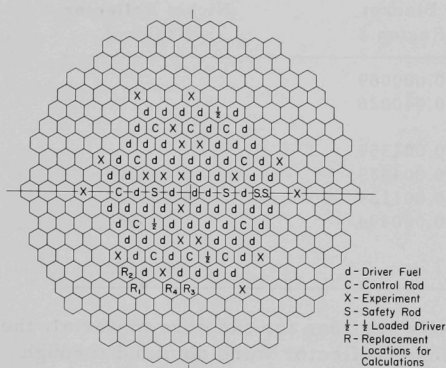
Fig. I.E.4. Core Loading for EBR-II Run 32D

Figure I.E.4 shows the
loading pattern for EBR-II Run 32D.
Each of the driver fuel elements has
a different history of exposure to
neutron flux, and therefore has dif-
ferent atomic densities of ^{235}U, ^{238}U,
^{239}U, and fission products. This
grossly heterogeneous distribution
of fuel and moderating material
produces substantial spatial power
variations in the reactor core and
inner blanket. These variations
must be well understood so that
local overpower can be prevented
by rearranging the core configura-
tion or changing the orifice size on
one or more subassemblies.

Analysis of a core configuration usually involves the execu-
tion of a two-dimensional discrete-ordinate transport calculation. For the
calculation, the hexagonal array of subassemblies is represented as a rec-
tangular array as shown in Fig. I.E.5. Each hexagonal subassembly is
represented by a corresponding rectangle which is then divided into four
volume elements for the calculation. The resulting array of 1764 mesh
points has been found to be sufficient to represent the reactor and yield
reliable values for the power generation in each subassembly.
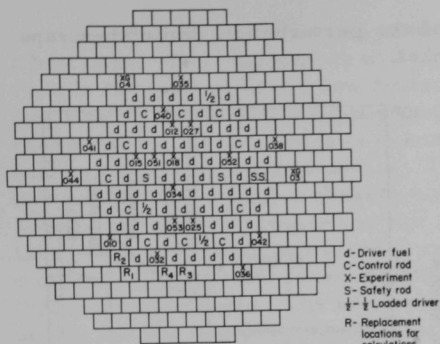
Fig. I.E.5. Rectangular Representation of Run-32D Loading Used in Calculation of Spatial Power Variations

The atomic densities of each subassembly, as calculated from the weights of the subassembly components at the time of fabrication and the subsequent burnup, are used in the calculation. Six-group and 22-group sets of cross sections averaged over the spectra of the core and blanket regions by the MC^2 code are used.

A series of transport calculations were performed to determine the perturbation in local fission rates that would be caused by replacing either one blanket subassembly or two adjacent blanket subassemblies with oxide-fuel experimental subassemblies. The positions of the proposed substitutions are indicated in Fig. I.E.5 as R$_3$ and R$_4$.

The resulting increase in power in the adjacent fuel elements can be seen from plots of the power along the y coordinates 11 and 8 and the x coordinate 21. Figure I.E.6 shows the power along y coordinate 11 with the blanket elements in place, with one blanket element (R$_3$) replaced by an oxide-fuel experimental subassembly, and with two blanket subassemblies (R$_3$ and R$_4$) replaced. This is a plot of the power in the EBR-II driver fuel elements at the edge of the core. The maximum relative power increase occurs at x coordinate 20. The increase is 3.8% when one blanket subassembly is replaced by oxide fuel and 7.7% when two are replaced.

Fig. I.E.6. Power along Y Coordinate 11

The effect on the adjacent blanket elements is much larger. As is shown in Fig. I.E.7, the power in the row of blanket subassemblies adjacent to the row in which the substitutions are made is increased by a factor of 2.0 at x coordinate 23 when one oxide-fuel subassembly is inserted. The power in the adjacent blanket subassembly at x coordinate 21 is increased by a factor of 2.5 when two oxide-fuel subassemblies are inserted.

Figure I.E.8 shows the extent to which the perturbation affects the power in subassemblies farther away from the substitution region

in the radial direction. The effect of the perturbation diminishes rapidly both in the core and in the blanket.
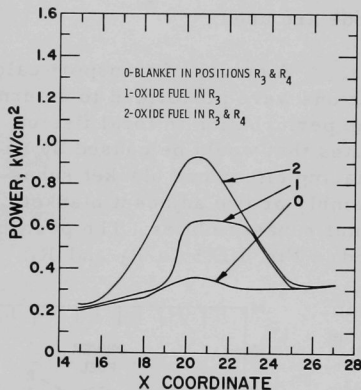
Fig. I.E.7. Power along Y Coordinate 8
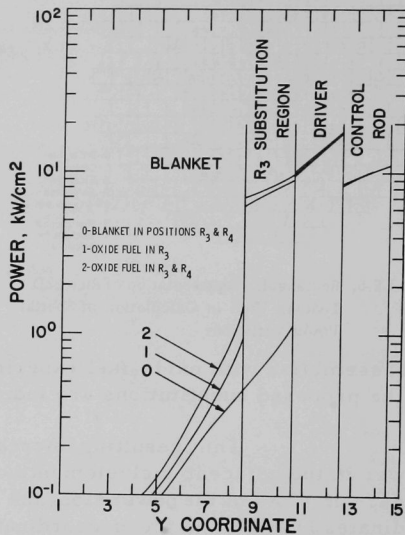
Fig. I.E.8. Power along X Coordinate 21

c. Equipment--Fuel Related (E. Hutter)

(i) Improved Gripper and Holddown Force-limit Devices
(W. M. Thompson, J. Pardini, and G. D. Giorgis)

Last Reported: ANL-7513, p. 56 (Oct 1968).

A prototype of the device to provide continuous measurements of the forces applied by the gripper and holddown mechanisms was designed in 1967 and constructed in 1968. The basic design concepts were previously reported (see Progress Reports for January 1967, ANL-7302, pp. 14-15, and February 1967, ANL-7308, pp. 3-4). Subsequent testing of the prototype to ensure operability, reliability, and integrity of the device has been satisfactorily completed. Certain maximum and minimum force limitations have not been resolved, however, and require actual measurements of packing-gland friction during fuel-handling operations. These measurements will be obtained from a field test. The test also will provide information about the electrical-noise conditions that will be encountered.

Construction of the permanent control console for the device has been started. Circuit diagrams and physical layouts showing

location of control components have been prepared as sketches to expedite fabrication. The components will be located on an instrument-mounting rack in the left bay of the new control cabinet that has been installed a few feet west of the EBR-II fuel-handling control console. All the panel space except the top $8\frac{3}{4}$ in., which is reserved for the instrumented subassembly, will be devoted to the new device. This 48-in.-high panel space will contain five panels with attached chassis for mounting equipment. The top two panels, one for the gripper and one for the holddown mechanism, will contain force-measuring and control amplifiers as well as force-indicating meters. The next two panels will hold the relays that control the timing of the calibration cycle. The bottom panel will contain the common dc power supply for the amplifiers and a spare supply for use if the first power supply fails. Each chassis will be mounted on chassis-track slides for easy accessibility and will be interconnected by flexible multiconductor cables. Cables also will connect this panel rack with the adjacent bay, where the relays and circuits that interface with the fuel-handling control console will be located.

Plans are being made to test this system on line without removing the existing force-limit device. This test will substitute for some of the testing originally planned to be done with a test rig. The console, when completed in Illinois, will be shipped to Idaho and installed in place. The two potentiometers that will be temporarily installed on the gripper carriage for the field test will be permanently installed in the final mechanical modification. These potentiometers will be connected to the console for the test and will produce the same signals that are expected after final installation. The equipment that interfaces with the fuel-handling control console will not be connected for the test; however, recording and alarm devices will be temporarily added in the second bay to monitor the functions of the new systems. After the performance testing, the mechanical modifications, such as replacing the existing force springs with more sensitive springs and removing the calibration components and limit switches, will be made and the interface equipment connected.

(ii) <u>New Control Rod Subassemblies</u> (O. S. Seim, T. Sullivan, and J. Pardini)

Last Reported: ANL-7577, p. 79 (April-May 1969).

(a) <u>Higher-worth Control Rod</u>. A draft of Technical Memorandum 82, "Design and Pressure-drop Characteristics of the EBR-II Higher-worth Control Rod," was completed. Studies are being made to determine if two intermediate-worth control rods should be used with the higher-worth rods in EBR-II. The former would provide regulation, and the latter would provide gross reactivity control.

(iii) <u>Oscillator Rod--Mark II</u> (O. Seim, J. Pardini, and
T. Sullivan)

Last Reported: ANL-7577, pp. 79-80 (April-May 1969).

The handling tool for the storage-basket adapter sleeve
was modified, and the modified tool was tested in sodium with satisfactory
results.

d. New Subassemblies Design and Experimental Support
    (E. Hutter)

(i) Irradiation Subassemblies

Last Reported: ANL-7577, pp. 81-82 (April-May 1969).

(a) Mark-A19A Irradiation Subassembly (O. Seim and
     E. Filewicz)

The Mark-A19A irradiation subassembly for the core
and the inner and outer blanket rows is a Mark-A19 subassembly that has
been modified to achieve higher flow rates and to permit use of standard
lower adapters. Figure I.E.9 shows the Mark-A19A irradiation subassembly
with a core-type lower adapter.

In the Mark-A19A design, the upper filter screen and
lower filter section have been deleted, and an axial reflector has been
added in the space formerly occupied by the lower filter section. An orifice
plate can be mounted below the axial reflector to provide reduced flow. The
capsule bundle is identical to that of the original design; it will contain
nineteen 3/8-in.-OD by 40-in.-long test capsules, each in a shroud tube.

The Mark-A19A subassemblies are expected to be more
economical to build than the Mark-A19 subassemblies, and will therefore
replace the Mark-A19 when the existing stock of nonstandard lower adapters
used by the Mark-A19 is depleted. A model subassembly is being built for
water-flow tests.

(b) Mark-J Irradiation Subassemblies (O. S. Seim and
     W. Ware)

Approval was received from the experimenter (General
Electric) for construction of the Mark-J19 subassembly for their encapsu-
lated high-temperature (1250°F max) fuel-irradiation experiment.

The Mark-J37 subassembly that was intended for high-
temperature irradiation experiments with unencapsulated fuel is being
redesigned. The redesign is necessary because the proposed pitch-to-
diameter ratio of 1.16 (0.250-in.-dia fuel element with a 0.040-in.-dia spiral
spacer wire) does not provide thermal-hydraulic conditions that are typical
of those expected in cores of commercial fast breeder reactors. A pitch-
to-diameter ratio of 1.2 to 1.3 is desired.
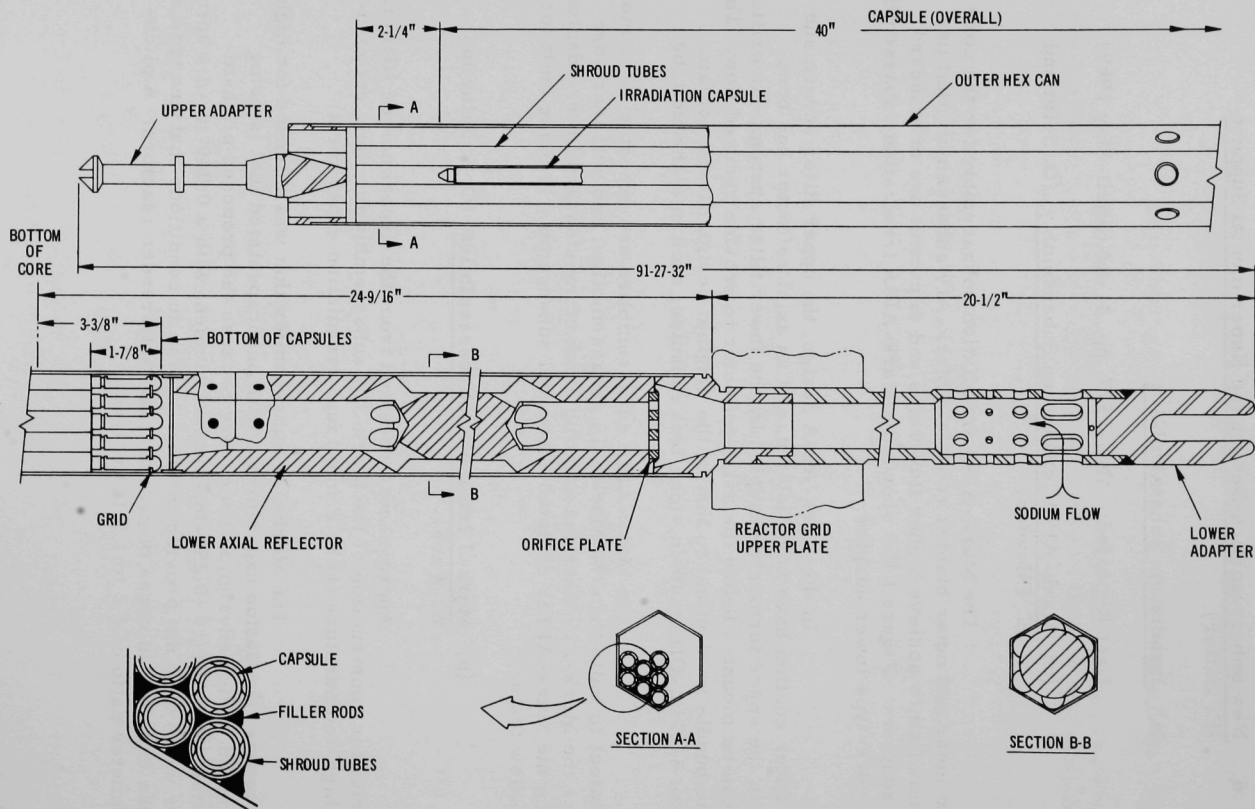
Fig. I.E.9. EBR-II Mark-A19A Irradiation Subassembly

e. Instrumented Subassembly (E. Hutter and A. Smaardyk)

   (i) Research and Development

      (a) Coupling Design (C. Divona and R. Brubaker)

         Previously Reported: ANL-7500, pp. 61-62 (Sept 1968).

            The original design of the instrumented-subassembly
coupling has been modified. In the original design, the coupling was sup-
ported by a spring designed to allow approximately 0.34 in. of differential
expansion between the coupling and the extension tube of the subassembly.
Recent calculations indicate that this clearance should be increased to
0.50 in. to allow the subassembly to be inserted into the reactor at the
normal rate of 15 in./min. The redesigned coupling will use a support spring
that will allow a differential expansion of 0.80 in. between the coupling and
extension tube.

            The additional clearance affected the design of the
coupling seal. The top of the coupling device is now to be sealed by a static
O-ring, a soft rubber gasket, and a movable O-ring. The movable O-ring
seal will accommodate the relative motion between the coupling and the
drywell liner of the subassembly.

      (b) Instrumented-subassembly Test 3 (PNL-17)
           (A. Smaardyk)

         Not previously reported.

            Pacific Northwest Laboratory (PNL) is planning an
irradiation test in EBR-II of 36 plutonium-bearing fuel elements with instru-
ment leads. ANL will do the design and some development that is necessary
for incorporating the experiment in a completed EBR-II instrumented
subassembly.

            Development of a method for anchoring to the sub-
assembly grid the conduit that will carry the flowmeter lead and the inlet-
thermocouple lead has been started.

f. Experimental Irradiation and Testing (R. Neidner)

   (i) Experimental Irradiations

         Last Reported: ANL-7577, pp. 87-89 (April-May 1969).

            Table I.E.4 shows the status of EBR-II experimental irradia-
tions as of June 15, 1969. Following the completion of Run 34 on May 21,

experimental Subassemblies XO53 and XO66 were removed from the grid. Subassembly XO53 contained 37 encapsulated Mark-II fuel pins having a maximum midplane burnup of about 4.4 a/o; XO66 contained two Mark-IA fuel pins having a maximum midplane burnup of about 3.5 a/o.

TABLE I.E.4. Status of EBR-II Experimental Irradiations as of June 15, 1969

Subassembly No. and (Position)	Date Charged	Capsule Content and No. of Capsules ( )	Experimenter	Accumulated Exposure (MWd)	Estimated Goal Exposure (MWd)	Burnup[a]
XG03 (7D1)	7/16/65	UO$_2$-20 w/o PuO$_2$ (2) Stainless Dummies (17)	GE	22,610	23,300	5.8
XG04 (7B1)	7/16/65	UO$_2$-20 w/o PuO$_2$ (2) Stainless Dummies (17)	GE	22,610	45,000	5.8
XA08 (4F2)	12/13/65	UC-20 w/o PuC (8) Structural (9) Structural (2)	ANL ANL GE	18,780	20,700	11.0 8.4 8.4
XO12 (4B2)	8/10/66	UO$_2$-20 w/o PuO$_2$ (19)	NUMEC	15,380	21,400	8.9
XO18A (4E2)	4/23/69	Thermocouple (2) Structural (2) Structural (3)	PNL ANL GE	1,834 12,580	2,700 22,900	0.9 5.6 5.6
XO19 (6D2)	1/13/67	UO$_2$-20 w/o PuO$_2$ (7) UC-20 w/o PuC (3) Structural (8) Graphite (1)	GE UNC PNL PNL	12,160	13,000	5.0 5.5 3.5 3.5
XO20 (6B5)	1/13/67	UO$_2$-PuO$_2$ (9) UC-20 w/o PuC (3) Structural (4) Structural (2) Graphite (1)	GE UNC PNL ANL PNL	12,573	13,000	5.2 5.6 3.6 3.6 3.6
XO21B (2D1)	2/23/69	Structural (6) Structural (1)	PNL PNL	11,974 3,294	23,200 7,200	6.5 1.4
XO27 (4B3)	11/21/67	UO$_2$-25 w/o PuO$_2$ (18) Structural (1)	GE PNL	9,896	16,000	5.6 4.5
XO32 (6E5)	11/22/67	UO$_2$-25 w/o PuO$_2$ (19)	PNL	10,199	11,900	4.2
XO33 (5E2)	12/22/67	UC-20 w/o PuC (19)	UNC	9,043	10,900	4.5
XO34 (2F1)	4/13/68	Structural (7)	ORNL	9,425	14,800	4.7
XO35 (7B4)	4/13/68	Structural (7)	ORNL	9,008	44,800	2.3
XO36 (7E1)	7/25/68	UO$_2$-25 w/o PuO$_2$ (19)	GE	7,294	33,300	2.0
XO38 (7C5)	5/7/68	Structural (7)	INC	8,499	17,700	1.9
XO40 (5B2)	8/14/68	UO$_2$-20 w/o PuO$_2$ (19) UO$_2$-20 w/o PuO$_2$ (16) Stainless Dummies (2)	ANL GE	6,584	7,000	3.2 3.4
XO41 (7A3)	7/24/68	Structural (7)	PNL	6,960	16,700	1.6
XO42A (7D5)	4/2/69	B$_4$C, Ta (7)	PNL	6,773	25,000	1.4
XO43 (4D2)	2/20/69	UO$_2$-25 w/o PuO$_2$ (37)	GE	3,010	5,500	1.6
XO44 (7A1)	9/28/68	Oxide Insulator (1) Stainless Dummies (6)	LASL	5,635	8,100	1.0
XO50 (4C2)	2/23/69	UO$_2$-20 w/o PuO$_2$ (4) UO2-28 w/o PuO$_2$ (4) UO$_2$-20 w/o PuO$_2$ (5) UC-18 w/o PuC (2) Structural (4)	GE GE ORNL W GE	3,010	7,500	1.7 + 7.7[b] = 9.4 1.6 1.6 1.6 1.2 + 5.3[b] = 6.5
XO51 (3A2)	12/16/68	UO$_2$-25 w/o PuO$_2$ (37)	PNL	3,555	16,400	0.7

TABLE I.E.4 (Contd.)

Subassembly No. and (Position)	Date Charged	Capsule Content and No. of Capsules ( )	Experi- menter	Accumulated Exposure (MWd)	Estimated Goal Exposure (MWd)	Burnup[a]
XO54 (4E1)	3/31/69	UO_2-25 w/o PuO_2 (37)	PNL	2,410	10,000	1.3
XO55[c] (6A4 & 7F3)	2/23/69	UC-15 w/o PuC (19)	UNC	3,010	20,000	0.9
XO56 (5C2)	4/2/69	UO_2-25 w/o PuO_2 (37)	GE	2,410	10,600	1.2
XO57 (2B1)	2/23/69	Structural (7)	PNL	3,010	15,000	1.4
XO58[d] (7F3 & 6F1)	4/24/69	UO_2-25 w/o PuO_2 (37)	GE	1,834	16,000	0.6
XO59 (4A1)	4/23/69	UO_2-25 w/o PuO_2 (37)	PNL	1,834	17,500	0.6
XO60 (7C3)	4/3/69	Structural (7)	INC	2,410	5,400	0.6
XO61 (7A5)	4/23/69	Structural (7)	INC	1,834	18,000	0.4
XO62 (6F3)	5/23/69	UO_2-25 w/o PuO_2 (37)	GE	986	12,300	0.4
XO64 (4C3)	5/28/69	UO_2-25 w/o PuO_2 (19)	GE	986	10,000	0.5
XO67 (4A3)	5/28/69	Weldments (4) Structural (1) Structural (1) Oxide Insulator (1)	PNL ORNL GE ORNL	986	2,400	0.4

[a]Approximate accumulated center burnup on peak rod (fuels, a/o; nonfuels, nvt x 10^{-22}).
[b]Previous exposure from another subassembly.
[c]Relocated from 6A4 to 7F3 at start of Run 35 to gain necessary reactor reactivity.
[d]Relocated from 7F3 to 6F1 at start of Run 35 to avert possible overheating of Row 8 blanket elements.

During the fuel handling for Run 35, three experimental subassemblies were loaded into the reactor grid: (1) XO62, a Mark-F37 subassembly containing unencapsulated mixed-oxide elements of the GE-F9B group; (2) XO64, a Mark-A19 subassembly containing encapsulated mixed-oxide elements of the Ge-F5 group; and (3) XO67, a Mark-B7 subassembly containing principally weldment samples from PNL, along with other structural and insulating-material samples from PNL, ORNL, and GE-NSP.

The PNL-7 group of unencapsulated mixed-oxide elements was successfully tagged by the sponsor with a xenon isotopic mixture furnished by ANL. This is the second group of test elements to be xenon-tagged; the first was the GE-F9D group. The 37 tagged PNL elements will be loaded into the first of a series of Mark-H37 experimental subassemblies.

g. FCF Equipment Improvement (M. J. Feldman)

(i) Process Equipment (N. R. Grant, J. P. Bacca, and V. G. Eschen)

Last Reported: ANL-7577, p. 91 (April-May 1969).

The stereomacroscope lens system was returned to the vendor for reworking. One of the lenses would not focus properly and could not be repaired on the site by a vendor representative.

h.   Hot Fuel Examination Facility (HFEF) (N. J. Swanson)

Last Reported: ANL-7513, p. 76 (Oct 1968).

(i)   Shielding Studies   (K. R. Ferguson)

Shielding experiments were conducted in the FCF to obtain experimental data that could be compared with calculated data. The results of the experiments will be used to evaluate the final design of the shielding for the Hot Fuel Examination Facility (HFEF).

The radiation dose rate at the surface of the roofs of the air and argon cells was measured using a source consisting of 365 fuel pins from five driver subassemblies discharged at the end of EBR-II Run 33. The roof of the air cell consists of 48-in.-thick reinforced concrete (288 g/cm^2). The roof of the argon cell consists of a 0.38-in.-thick steel liner and two layers of reinforced concrete, one 48 in. thick (299 g/cm^2) and the other 54 in. thick (334 g/cm^2). The density of the concrete was assumed to be 144 lb/ft^3. The fuel pins formed a plane source approximately 4 ft on a side and one pin diameter thick; measurements were made in a direction perpendicular to the plane so that the effect of self-absorption was reduced.

The measured dose rates, normalized for a source-to-detection distance of 25 ft, were 4.8 mR/hr for the air cell ten days after reactor shutdown, and 2.1 and 0.44 mR/hr for the two shield thicknesses of the argon cell 15 days after reactor shutdown. The change in thickness of 6 in. resulted in an increase in attenuation by a factor of 4.8, which is equivalent to 51 g/cm^2 for a tenth-value layer.

High- and low-level thermoluminescent dosimeters were used to measure the radiation source intensity. The intensity of the source ten days after reactor shutdown (filtered through 0.25 in. of aluminum) was 1.4×10^6 R/hr corrected to a distance of 1 ft.

The RIBD code was used to calculate the quantities of fission products contributing significantly to the penetrating radiation. Based on a decay time of ten days and the irradiation history of the fuel, these quantities were determined to be 11,000 Ci of ^{132}I, 51,000 Ci of ^{140}La, and 10,000 Ci of ^{156}Eu. The ISOSHLD code was to calculate the dose rate resulting from these quantities of fission products. The calculated dose rate was greater than the measured dose rate by an average ratio of 2.9. The determinations for the three shield thicknesses gave values that were within ±15% of this value.

On the basis of measurements made with relatively thin shields, it has been reported that gamma radiation obliquely incident on a slab is more penetrating than would be calculated on the basis of the oblique slab thickness. This effect has been called the refractive effect because its

result is as if the gamma rays were bent toward the normal. The effect is significant for gamma energies and in materials in which considerable Compton scattering occurs.

The refractive effect was observed in the FCF shielding experiments. Doses were measured at points along the shield that were various distances from the point normal to the source, and these doses were compared with the calculated doses based on the measured variation of attenuation with shield thickness. The ratio of observed to calculated dose was 1.02 at a 10° angle of incidence, 1.2 at 20°, and 1.7 at 30° for a 48-in.-thick shield of steel-reinforced ordinary concrete (288 g/cm^2). It is estimated that, under the conditions of these tests, the observed overestimate of penetration associated with the 2.9 buildup factor is adequate to compensate for the refractive effect when radiation is incident up to an angle of about 40°.

i. Feasibility Study of Fuel Failure Detection--Chemical and Mechanical Methods

(i) Trace Elements Analytical Techniques (C. E. Crouthamel)

Last Reported: ANL-7577, pp. 96-97 (April-May 1969).

No further experiments are planned in connection with the sodium-soluble tag program because the project is to be terminated. Only the work deemed necessary for the preparation of a terminal report will be continued.

As was pointed out previously (see ANL-7577), the ^{197}Au-^{198}Pt tagging method seemed more attractive than the ^{197}Au-^{121}Sb method, in that instability of the tag after discharge to the primary sodium would not be expected to alter the activity ratio of the activation products, ^{198}Au and ^{199}Au. However, recent calculations have shown that, during variations in reactor operating conditions, the ^{198}Au/^{199}Au activity ratio would not be as constant as the ^{198}Au/^{122}Sb activity ratio. The reasons for the greater variation in the ^{198}Au/^{199}Au activity ratio are as follows: (1) The half-life of ^{122}Sb (2.8 days) is more nearly equal to the half-life of ^{198}Au (2.7 days) than is the half-life of ^{199}Au (3.15 days). (2) The formation of ^{199}Au is delayed by the 31-min half-life of the intermediate activation product ^{199}Pt.

To gain some insight into how much variation would be produced by reactor startups, shutdowns, and changes in power, calculations were made which permitted comparison of the performance of the ^{197}Au-^{198}Pt tag with that of the ^{197}Au-^{121}Sb tag during a one-month period of operation of EBR-II. The following assumptions were made in performing the calculations:

(1) Each tag is composed of an equal weight ratio of ^{197}Au and the other isotope.

(2) The capture cross sections are 100 mb for ^{197}Au, and 70 mb for both ^{198}Pt and ^{121}Sb.

(3) The time to achieve the power level and the time to shutdown are insignificant.

The results of these calculations are given in Table I.E.5. It is evident from these results that the identification of a Pt-Au tag would be more difficult than the identification of an Sb-Au tag because the variations in activity ratios are greater. However, with adequate fuel-failure detection equipment and a power record of the reactor, identification would still be possible.

TABLE I.E.5. Calculated Activity Ratios of Tags during EBR-II Reactor Operation[a]

Time Interval (days)	Power (MW)	Activity Ratio at End of Period	
		^{198}Au/^{122}Sb	^{198}Au/^{199}Au
3.5	30	1.79	3.19
7.0	0	1.68	2.43
2.5	30	1.78	3.10
1.0	0	1.77	2.95
3.25	30	1.78	3.04
1.25	0	1.76	2.87
3.25	30	1.77	2.98
3.25	0	1.72	2.62
2.5	30	1.76	2.95
3.5	50	1.78	3.02

[a]The period used for these calculations is considered to be a typical EBR-II operating period. (It extended from Oct. 1 to Oct. 31, 1968.)

(ii) Sodium Loop--Tag Confirmation Study (J. T. Holmes)

Last Reported: ANL-7577, p. 97 (April-May 1969).

Assembly of the loop designed for evaluating the stability of isotopic tags in circulating sodium has been completed except for application of secondary insulation. Current efforts involve the installation of tubing connections between the loop and a portable supply drum containing 50 gal of sodium.

The tag study for which this loop was originally constructed has been discontinued. Attention is now being given to the modifications that would have to be made to use the loop for tests of on-line monitoring, sampling, and purifying equipment. Further reports on the use of this loop will appear under Component Development--LMFBR, Sodium Technology Development.

j.   Materials-Coolant Compatibility (D. W. Cissel)

(i)   Examination of Reactor Parts (W. E. Ruther and T. D. Claar)

Last Reported: ANL-7577, pp. 98-99 (April-May 1969).

(a)   Analysis of Roll Pins from EBR-II. Three Type 420 (12-14% Cr) stainless steel roll pins from EBR-II sensing-rod Subassembly No. 2 were subjected to metallographic examination by ANL in Illinois after a similar pin in another subassembly had failed. The pins, each 5/32 in. OD x 0.085 in. ID x 1 in. long, were used to secure a solid shaft within a hollow concentric shaft at three places along the sensing-rod subassembly.

All three pins exhibited surface scales that appeared to be oxides. The reaction layer was more evident at the inner surfaces than at the outer, probably because of the limited access of the environments to the outer surfaces of the pins. The locations of the pins in EBR-II and the depths of the oxide layers in the pins were as follows:

Pin No.	Location of Pinned Joint	Maximum Depth of * Oxide Layer (mils)	
		Inner Surface*	Outer Surface**
2A	Primary Argon (cool)	0.1	0.1
2B	Primary Argon (hot)	0.2	0.1
2C	Primary Sodium (hot)	0.2	0.1

All three pins had the same microstructure, that of partially tempered martensite. Some coalescence of the carbides was observed at 1000X magnification. This microstructure is similar to that observed in three other pins examined by ANL in Idaho.

---

*Scale was continuous on all pins.
**Scale was in isolated areas on all pins.

Microhardness traverses across the transverse sections failed to reveal any hardness gradients from OD to ID. The average microhardness readings for the three pins were in the range from 550 to 580 KHN, which compares closely with the value of 570 KHN obtained for the failed roll pin.

Carbon analyses of the three pins showed an average concentration of 0.36 wt % C, well above the minimum specification of 0.15 wt % C for Type 420 stainless steel.

The three roll pins examined at ANL-Illinois compared very well with those studied at ANL-Idaho with respect to microstructure and hardness. However, the pins examined in Illinois showed less inner- and outer-surface oxidation product than those examined in Idaho and appeared to have less surface flaws (microcracks, microlaps, etc.). No evidence was found of substantial interaction of liquid sodium with the Type 420 stainless steel roll pins.

(b) **EBR-II Coolant-circuit Materials** (S. Greenberg)

(1) **Primary System**. In the Progress Report for April 1968, ANL-7445, p. 88, Monel and nickel were listed as being exposed to sodium in the primary system. This is incorrect. Except for possible experimental objects, neither nickel nor Monel is exposed to primary sodium.

(2) **Secondary System**. The materials exposed to sodium and to argon containing sodium vapor in the EBR-II secondary system are listed in Tables I.E.6, I.E.7, and I.E.8. These materials were identified through the study of drawings of the system.

TABLE I.E.6. Materials Exposed Directly to Liquid Sodium

Material	Approximate Service Temperature (°F)
Inconel	770
Type 304 Stainless Steel	300-860
Type 316 Stainless Steel	590
Type 347 Stainless Steel	560-840
Type 501 Stainless Steel	860
Ferritic Steels: $2\frac{1}{4}$ Cr-1 Mo (ASTM grades A-182, F22; A-213, T22; A-234, WP22; A-335, P22; A-387, D)	580-860
Stellite	590

TABLE I.E.7. Materials Exposed to Argon
Containing Sodium Vapor[a]

Material	Approximate Service Temperature (°F)
Carbon Steel	360-500
Carbon Steel, Galvanized	360
Type 304 Stainless Steel	360-590
Type 316 Stainless Steel	590-700
Type 347 Stainless Steel	590
Stellite	590

[a]Only those materials exposed at temperatures above the
melting point of sodium (208°F) are listed. The concen-
tration of sodium in argon is negligible below 208°F.

TABLE I.E.8. Materials Exposed to Liquid Sodium
if Primary Containment Fails

Material	Primary Containment	Approximate Service Temperature (°F)
Carbon Steel	Inconel Rupture Disks	770
Chromel-Alumel	Type 304 Stainless Steel and $2\frac{1}{4}$ Cr-1 Mo Ferritic Steel Thermocouple Sheaths	300-860
NaK	Type 304 Stainless Steel Pressure Transmitters	590-860

None of the materials listed is of itself of con-
cern with respect to integrity in the service environment. However, possible
problems could arise as the result of carbon transfer from relatively high-
carbon materials to austenitic stainless steel components. Experiments are
in progress to evaluate the possible seriousness of the situation. There is
at present no evidence of any deleterious compatibility effects in the sec-
ondary sodium system.

(ii) Data Development (F. A. Cafasso)

Last Reported: ANL-7561, p. 43 (March 1969).

Sufficient data have been obtained to demonstrate that liquid
sodium at 650°C can leach (tramp) copper from Type 304 stainless steel
(see ANL-7561, p. 43). The main objective of the study having been satisfied,
the experiments are being discontinued.

k. Study of Operation with Failed Fuel (R. R. Smith)

(i) Unbonding of Sodium in Row 8 Blanket Elements
(P. B. Henault)

Not previously reported.

A study was made to determine whether or not a Row 8 blanket element can become unbonded during operation or during a subsequent reactor shutdown after a lower weld has failed. The results of the study indicate that the typical element will lose 4.85 cc of sodium, or about 75% of the bond sodium above the top blanket pin. After pump shutdown, the plenum gas will expand and expel additional bond sodium out of the element, equivalent to about 18% of the original bond inventory. On each subsequent startup, this latter volume of sodium will be sucked back into the element, to be expelled again after the next shutdown.

For the nontypical element that has been filled with sodium to a minimal level, slight unbonding is thought to be likely. For the extreme case (e.g., where sodium and uranium volumes are minimal and jacket volume is maximal), 5.30 cc of sodium, or about 29% of the total bond, will be expelled.

The amount of sodium expelled from a blanket element in Row 8 after each shutdown, once the element has become defective and allows free passage of sodium in and out of the element, was calculated for a number of temperatures. Values were calculated for nominal, maximal, and minimal initial sodium filling (see Table I.E.9).

TABLE I.E.9. Calculated Volumes of Sodium Bond Expelled from Row 8
Blanket Element after Shutdown

Temperature ($°F$)	Volume Expelled (ml)			Initial Bond Expelled[a] (% of Total)
	Nominal Initial Sodium Filling	Maximal Initial Sodium Filling	Minimal Initial Sodium Filling	
800	4.15	4.63	3.68	20
850	3.75	4.18	3.34	18
900	3.35	3.74	2.97	16
1000	2.55	2.85	2.27	12
1100	1.75	1.96	1.56	8.5
1200	0.95	1.06	0.85	4.6
1300	0.15	0.17	0.14	0.7
1319	0.00	-	-	0.0
1400	-0.65[b]	-0.72[b]	-0.57[b]	-3.1[b]

[a]Percent is based on nominal values and with the total bond assumed to be at 850°F.
[b]Negative values indicate that sodium is sucked into element after shutdown.

Basic data for the elements used in the analysis are summarized in Table I.E.10. Plenum temperature was considered to be the same as the coolant exit temperature. From encapsulated melt-wire

experiments conducted in position 8E3, the temperature was found to be between 813 and 845°F. Calculations indicate the hottest average coolant exit temperature to be 893°F for a Row 8 subassembly (the range was calculated to be from 870 to 910°F). For the analysis reported here, an average plenum temperature of 850°F was used.

TABLE I.E.10. Row 8 Blanket-element Data
Used in Unbonding Analysis

Inside tube length (in.)	61
Tube diameter (in.)	0.457
Total pin length (in.)	55
Pin diameter (in.)	0.433
Total uranium weight (kg)	2.513
Sodium level above top pin (in.)	1.5 ± 0.5
Sodium volume[a] (ml)	
Nominal	18.08
Maximal	19.06
Minimal	17.10
Nominal gas volume[a] at 77°F and 14.35 psia (ml)	8.87
Mean atmospheric pressure where filled (psia)	14.348
Volume coefficient of expansion of Type 304 stainless steel	$30.6 \times 10^{-6}/°F$
Volume coefficient of expansion of uranium	$34.2 \times 10^{-6}/°F$
Tolerance in tube volume (%)	0.5
Tolerance in pin volume (%)	0.6
Spring volume (cc)	4.303
Coolant exit temperature (°F)	
Measured	813-845
Calculated	893
Range of coolant exit temperatures (°F)	40
Static pressure (psia)	
Top	17.6
Bottom	19.3
Operating pressure (psia)	
Top	24.0
Bottom	29.6
Burnup (a/o)	
Position 8F3	0.02036
Position 8F4	0.02416
Estimated pin growth (%)	1.0

[a]Excluding effects of tolerances in tube and pin diameters.

From a recently completed study of irradiation growth of blanket elements, it has been estimated that a 0.025-a/o burnup of Row 8 elements corresponds to an overall expansion of approximately 1%.

Row 8 blanket elements were fabricated in Illinois, and the mean atmospheric pressure for that location was used in calculating the actual argon inventories in the elements. A room temperature of 77°F was assumed.

The fission gas released to the plenum was considered to come only from recoil fission products, which would provide 0.05% release. For the present burnup, the volume of released gas was calculated to be about 0.0077 cc (STP) and was therefore ignored in the calculations.

The burnup values reported in Table I.E.10 are the highest average determined for an individual element in the designated subassembly location.

Specific values of the volumes used in estimating bond expulsion are shown in Table I.E.11. The volumes were calculated for the cold and fresh condition, the fresh hot operating condition, and the present estimated pin growth. A nominal 800°F temperature rise was used in estimating the contribution due to thermal expansion.

TABLE I.E.11. Calculated Nominal Volumes Used in Unbonding
Analysis of Row 8 Blanket Element (values in ml)

	Cold (77°F)	Hot Operating	Hot with 1% Expansion	Variation from Nominal (%)
Tube or element	163.966	168.164	168.164	0.5
Uranium	132.718	136.116	137.477	0.6
Total sodium	18.076	20.637	20.637	10.9
Sodium in annulus	15.120	15.506	14.145	9.9
Sodium above pins	2.956	5.131	6.492	56.0
Plenum (gas plus sodium above pins)	11.825	12.127	12.127	0.5
Total void space of plenum plus annulus	26.945	27.635	26.274	5.9
Gas space	8.868	6.996	5.637	64.0
Argon inventory (STP)	7.930	7.930	7.930	40.0
Fission-gas inventory (STP)	0.0	0.0	0.008	0.0
Spring	4.303	4.413	4.413	0.0

The variations from the nominal volumes reported in Table I.E.11 are the maximum possible. For example, the table shows the sodium volume varying by 10.9% from the nominal. An increase of 10.9% would occur for an element having maximal tube volume and minimal pin volume, and which had been filled with sodium to a maximal level. The values reported in Table I.E.9 are based on credible rather than possible variations. Gas volume was considered to vary by 1.0 ml, which is slightly more than the acceptable variations in sodium filling.

The nominal volume of sodium bond expelled after a lower-weld failure was found to be 4.85 cc. From Table I.E.11, it can be seen that this represents about 75% of the bond sodium above the fuel at the time of failure.

Maximum expulsion should occur for the element with maximal argon inventory, minimal sodium filling, and maximal void volume. Minimum expulsion should occur for the element with minimal argon, maximal sodium, and minimal void volume. The maximum and minimum extrusion volumes were found to be 5.30 and 4.42 cc, respectively.

Actual values for the maximum and minimum bond expulsion should be less extreme than those calculated because all tolerances were added in calculating the values.

The additional volume of sodium expelled from an element with a fault after each pump shutdown will depend on the operating temperature and the level of sodium filling. For 850°F and nominal filling, the volume of the expelled sodium was calculated to average 3.75 cc (maximum and minimum values were calculated to be 5.28 and 2.26 cc, respectively). These extremes are considered possible rather than credible; the credible values are reported in Table I.E.9.

1. Systems Engineering (B. C. Cerutti)

(i) Surveillance, Evaluation, and Studies of Systems

Last Reported: ANL-7577, pp. 103-104 (April-May 1969).

(a) Depressurization of Reactor Building (H. W. Buschman)

A partial depressurization (about 0.5 psi) of the reactor building occurred on March 28. The exact cause of the depressurization has been determined, and corrective action has been taken.

On March 28, the electrical solenoid on the exterior-air-supply valve of the building failed and the valve closed. The air-supply fan also automatically tripped off. This action was normal and as designed. What was not normal was that closure of the air-supply valve did not actuate a limit switch on the valve, which in turn would have caused the building exhaust valve to close and thereby prevent depressurization of the building. Since the exhaust valve remained open and the exhaust fans continued to run, air was continuously removed from the reactor building, causing a partial depressurization of about 0.5 psi in approximately 3 min although the automatic vacuum-relief valve had opened during the depressurization, its relief capacity is not large enough to handle the volume of air exhausted by the exhaust fan (about 7000 cfm) without some depressurization of the building. At the end of the 3-min period a partial isolation of the reactor building was manually initiated and the manual pressure-relief valve was opened. Pressure within the building then returned to normal.

The failed solenoid was replaced, but the cause of the abnormal system response could not be immediately determined. Because the consequences of this failure were judged not to be serious and the system appeared to operate normally after the failed solenoid was replaced, operation of the reactor was resumed. Further investigation of the failure was planned for a time when such an investigation would not be plant-controlling.

During the last week of May, the building isolation system was checked out. Operation of the system at first appeared to be normal in all respects. It was decided to fail the solenoid on the air-supply valve manually and observe the system response. When this was done, the subsequent events were identical to those that caused the depressurization on March 28. The cause of the system failure was then quickly traced to the closed limit switch on the air-supply valve. Because of solenoid failure, the switch would not actuate when valve closure occurred, but it would actuate when the valve was closed by ordinary means. Adjustment of the limit switch corrected the situation.

2. Operations

a. Reactor Plant (G. E. Deegan)

Last Reported: ANL-7577, pp. 109-110 (April-May 1969).

The reactor was operated for 998 MWd from May 21 through June 20. This raised the cumulated total of reactor operation to 26,041 MWd. Run 34B was completed on May 21, and Run 35 was begun on May 29.

During the shutdown for fuel handling between Runs 34B and 35, further changes were made in the detection system of the fuel-element-rupture detector. Each of the three channels of the system again have two BF_3 counters, but the counters are now shielded from the sodium piping by 2 in. of lead for gamma attenuation and 1 in. of polyethylene for neutron scattering. Results to date indicate that the shielding has practically eliminated the degradation in count rate that was previously observed.

During Run 34B no evidence of a fission-gas release was observed. At the end of the Run 34B, the test subassembly containing the element with the known upper-weld defect was removed from the grid and placed into the storage basket. Other loading changes made after Run 34B included the following. The stainless steel drop rod was replaced with a new stainless steel drop rod of modified design (see Sect. I.E.1.a). The two silicon carbide temperature-test subassemblies (containing pellets for determining coolant outlet temperature) and the friction-test subassembly (containing a pellet for determining oxygen content of the sodium coolant) had completed their scheduled irradiation and were removed from the grid.

Seventeen surveillance subassemblies were removed. These included seven extended-burnup subassemblies, the last 50-MW Phase II surveillance subassembly, and the seven remaining subassemblies in the cold-line Phase II surveillance program. Two controlled-flow subassemblies were removed and replaced by new controlled-flow subassemblies. Three fresh subassemblies containing samples of vendor fuel were installed. [The fuel handling of experimental subassemblies is reported under Sect. I.E.1.f.(i).]

Routine physics experiments, consisting of reduced-flow and rod-drop tests, were performed at the beginning of Run 35.

b. Fuel Cycle Facility (M. J. Feldman)

Last Reported: ANL-7577, pp. 110-123 (April-May 1969).

(i) Fuel Production

(a) Cold-line Production and Assembly (D. L. Mitchell)

Table I.E.12 summarizes the production activities for May 16 through June 15, 1969, as well as for the year to date.

Eight batches (approximately 800 elements) of Mark-II fuel elements have been completed. The cold-line equipment is being reconverted from Mark-II to Mark-IA fuel-element production. Production of Mark-IA fuel has been resumed.

(ii) Inspection of Vendor Fuel (D. L. Mitchell)

A summary of the data relating to receipt and acceptance of fuel produced by Aerojet-General Corporation is included in Table I.E.12. The acceptance rate for the ANL verification inspection of the fuel was higher than 98% during the reporting period.

(iii) Surveillance (M. J. Feldman, J. P. Bacca, and E. R. Ebersole)

(a) Postirradiation Analysis of EBR-II Fuel (J. P. Bacca)

(1) Surveillance of Vendor-produced Fuel. In attempts to determine the cause of the abnormal irradiation shortening of the vendor-produced Mark-IA fuel, efforts are being directed toward characterizing that fuel and comparing its characteristics with those of fuel produced in the FCF cold line. The areas under investigation are summarized below.

TABLE I.E.12. Production Summary for FCF Cold Line

	5/16/69 through 6/15/69		Total This Year	
	Mark IA	Mark II	Mark IA	Mark II
Alloy-preparation runs				
New fuel	0	1	1	8
Remelts	0	0	5	3
Total	0	1	6	11
Injection-casting runs	2	0	8	10
Pins processed				
Accepted	213	0	971	941
Rejected	7	0	34	53
Elements welded	0	350	1,707	884
Elements rewelded	0	69[a]	0	69
Elements leaktested				
Accepted	0	471	1,705	804
Rejected	0	6	40	21
Elements bondtested				
Accepted	0	609	1,730	791
Rejected	0	5	262	7
Subassemblies fabricated (cold-line fuel)	2	0	12	0
Elements received from vendor	1,497	–	23,635[b]	–
Inspected and accepted	2,092	–	20,546[b]	–
Inspected and rejected	36	–	1,236[b]	–
Subassemblies fabricated (vendor fuel)	3[c]	–	5	–
Total elements available for subassembly fabrication as of 6/15/69				
Cold-line fuel				
Mark IA	864			
Mark II	789			
Vendor fuel (all Mark IA)	19,755			

[a]Visual examination of 64 welds indicated that they were not acceptable for potentially high-burnup experiments.
[b]Total includes figures for 1968.
[c]Each subassembly is made up of a mixture of vendor and cold-line fuel elements.

(A) <u>Metallography</u>. Optical and electron metallography of unirradiated and irradiated vendor fuel are being conducted by ANL, PNL, and LASL to characterize this type of fuel, determine the nature of the irradiation damage done to it, and compare this fuel with FCF-produced fuel.

(B) <u>Gamma Scanning</u>. Elements containing shortened irradiated fuel pins are being gamma-scanned in an effort to select, by nondestructive means, pins that may have increased in diameter at the top rather than at the bottom of the element. This top swelling will be confirmed by measuring the diameters of the dejacketed pins.

(C) <u>Density Measurements</u>. Measurements are being made of the density of FCF and vendor fuel pins as cast and after

gamma-solution treatment to determine the amount of retained gamma phase in the as-cast pins. This effort will help to characterize the FCF and vendor casting processes. The density of irradiated vendor fuel also is being measured to determine the effect of irradiation on density.

(D) Heat Treatment of Cladding Material. An effort has been initiated to determine the effect of heat treating the cladding material in air to 660°C. The effect of time at 660°C on sensitization, oxidation, compatibility with fuel, straightness, and tensile strength will be investigated. This information will be needed for evaluation of various proposed remedial methods that may be used to reclaim this fuel.

(E) Irradiation Experiments. Three subassemblies containing intermixes of vendor-produced, vendor-cast and FCF-bonded, and FCF-produced fuel are being irradiated. Results from postirradiation examination of elements from these subassemblies should confirm or discount the supposition that the shortening of the vendor fuel is connected with the vendor's bonding process. Elements for two additional subassemblies are being processed by the vendor and ANL. These elements will be identified as to casting parameters, casting orientation, bonding conditions, and sample retention. Included in the variables being reviewed is ANL bonding of vendor-cast pins. The vendor has heat treated 30 elements for 1 hr at 500°C before bonding them by his centrifugal bonding process. These elements and 61 cold-line elements will be made into an additional subassembly.

(2) 70%-enriched Fuel Experiment. Postirradiation examination of elements from Subassembly C-2193S, which was irradiated to a total calculated maximum burnup of 1.54 a/o in grid position 4B1, has been conducted. This subassembly contained elements formerly irradiated to 1.23 a/o in Subassembly C-2175S. Table I.E.13 shows the fuel swelling that took place in the elements during irradiation. Swelling of the fuel pins, as determined by eddy-current measurements of bonding-sodium level, averaged 10.1%. (Silicon content of the fuel ranged from 260 to 533 ppm.) Swelling

TABLE I.E.13. Fabrication and Irradiation Data for
70%-enriched Driver-fuel Subassembly C-2193S[a]
(Burnup: 1.55 a/o max; 1.30 a/o avg)

Injection-casting Batch No.	Silicon Content of Fuel (ppm)	Number of Elements	Element-burnup Range (a/o)	Total Volume Swelling of Fuel ($\Delta V/V$, %)	
				Average	Range
0700	260	4	1.45-1.50	11.85	9.83-15.51
0701	533	4	1.45-1.49	11.01	8.84-14.23
0702	362	9	1.42-1.53	10.10	8.33-11.44
0703	407	22	1.41-1.55	14.31	7.41-16.73
0704	409	14	1.42-1.53	8.26	6.20-9.94
0705	437	27	1.41-1.55	7.71	5.97-9.01

[a]Received 1.23 a/o burnup as Subassembly C-2175S.

of individual pins ranged from 6.2 to 16.7%. These data are illustrated in Fig. I.E.10, which indicates that swelling of 70%-enriched fuel has increased slightly over that previously observed and that the swelling ranges are larger than those observed for earlier subassemblies. No jacket strain was found in three elements that were examined.
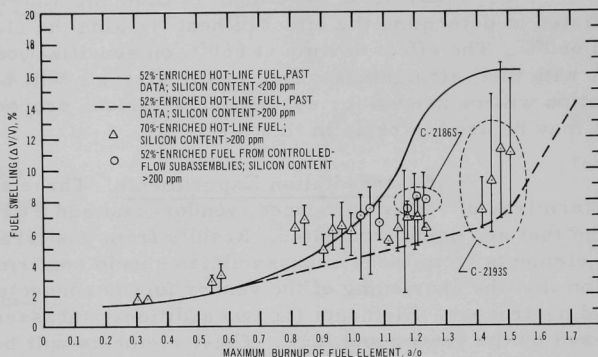
Fig. I.E.10. Swelling of 70%-enriched EBR-II Fuel and 52%-enriched Fuel from Controlled-flow Subassemblies as a Function of Burnup

(3) Controlled-flow Experiment. Table I.E.14 summarizes the results of postirradiation measurement of swelling for Subassembly C-2186S, which achieved a calculated maximum burnup of 1.23 a/o in grid position 2A1. This subassembly contained both Mark-IA and Mark-IB fuel. Average fuel-pin swelling was 8.0%, which is consistent with data previously obtained for the controlled-flow subassemblies at lower burnups. These values, however, are slightly higher than values for average fuel-pin swelling of 70%-enriched fuel of comparable silicon concentrations that was irradiated to similar burnup levels. These data are compared in Fig. I.E.10.

TABLE I.E.14. Fabrication and Irradiation Data for
Controlled-flow Driver-fuel Subassembly C-2186S[a]
(Calculated burnup: 1.23 a/o max; 1.08 a/o avg)

Injection-casting Batch No.	Silicon Content of Fuel (ppm)	Number of Elements	Element-burnup Range (a/o)	Total Volume Swelling of Fuel ($\Delta V/V$, %)	
				Average	Range
Mark IA					
095	290	10	1.17-1.23	6.69	2.05-8.21
096	308	10	1.18-1.23	8.09	6.30-9.92
097	276	26	1.17-1.23	8.08	5.79-9.24
Mark-IB					
095	290	10	1.17-1.23	7.28	6.32-8.42
096	308	10	1.17-1.23	7.93	4.86-9.79
097	276	25	1.17-1.23	8.70	6.45-9.75

[a]Held 46 Mark-IA and 45 Mark-IB elements.

(4) Driver-fuel Extended-burnup Program. Fuel elements from Subassembly B-362 were examined after being irradiated to a calculated maximum burnup of 1.72 a/o in grid position 6B3. This is the first driver subassembly that has been irradiated to the 1.7-a/o level. Table I.E.15 summarizes the results of postirradiation measurement of swelling for B-362. Average fuel-pin swelling for the subassembly was 10.7%; swelling of individual pins ranged from 5.6 to 16.0%. These data show that the slope of the swelling-versus-burnup curve for fuel containing 200 to 500 ppm silicon increases at burnups above approximately 1.5 a/o (see Fig. I.E.11).

TABLE I.E.15. Fabrication and Irradiation Data for
Extended-burnup Driver-fuel Subassembly B-362
(Calculated burnup: 1.72 a/o max; 1.43 a/o avg)

Injection-casting Batch No.	Silicon Content of Fuel (ppm)	Number of Elements	Element-burnup Range (a/o)	Total Volume Swelling of Fuel ($\Delta V/V$, %)	
				Average	Range
4158	290	46	1.51-1.72	11.63	6.88-15.96
4160	370	45	1.50-1.71	9.82	5.63-14.26
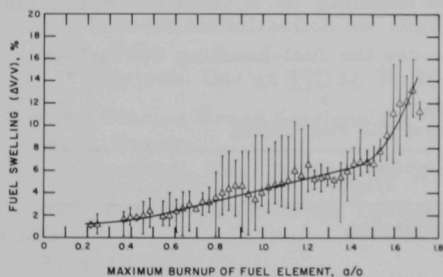
Fig. I.E.11. Swelling of EBR-II U-5 w/o Fs Driver Fuel as a Function of Burnup

No jacket strain was observed in six elements measured, even though eddy-current traces indicated contact between the fuel and jacket.

Fuel elements from Subassembly C-2109 were examined following irradiation to a maximum calculated burnup of 1.53 a/o. Table I.E.16 summarizes the results of postirradiation measurement of fuel swelling. These data are in close agreement with previous data obtained in the 1.5-a/o burnup range. Average fuel-pin swelling for the subassembly was 7.2%; swelling of individual pins ranged from 4.8 to 10.7%.

TABLE I.E.16. Fabrication and Irradiation Data for
Extended-burnup Driver-fuel Subassembly C-2109
(Calculated burnup: 1.53 a/o max; 1.31 a/o avg)

Injection-casting Batch No.	Silicon Content of Fuel (ppm)	Number of Elements	Element-burnup Range (a/o)	Total Volume Swelling of Fuel ($\Delta V/V$, %)	
				Average	Range
4228	260	1	1.51	5.45	-
4230	350	16	1.45-1.51	6.08	4.76-6.79
4231	300	7	1.46-1.47	6.62	5.12-7.57
4232	340	24	1.44-1.46	6.50	5.31-7.16
4233	260	42	1.44-1.51	8.28	5.70-10.69
0449	300	1	1.47	6.82	-

Fuel elements from Subassembly C-2147 were examined following irradiation to a maximum calculated burnup of 1.47 a/o. Table I.E.17 summarizes the results of postirradiation measurement of fuel swelling. These data also are in close agreement with past data obtained at 1.5 a/o burnup. Average fuel-pin swelling for the subassembly was 6.0%; swelling of individual pins ranged from 3.8 to 7.4%.

TABLE I.E.17. Fabrication and Irradiation Data for
Extended-burnup Driver-fuel Subassembly C-2147
(Calculated burnup: 1.47 a/o max; 1.26 a/o avg)

Injection-casting Batch No.	Silicon Content of Fuel (ppm)	Number of Elements	Element-burnup Range (a/o)	Total Volume Swelling of Fuel ($\Delta V/V$, %)	
				Average	Range
022 IH	230	49	1.38-1.46	6.37	3.90-7.37
023 IH	300	42	1.36-1.44	5.54	3.80-6.28

Subassemblies C-2148, C-2085, B-3025, and B-3027 in this program have been irradiated to a burnup of 1.5 a/o and are being received at the FCF for examination.

(iv) Fuel Management and Handling (N. R. Grant and P. Fineman)

Table I.E.18 summarizes the fuel-handling operations during the reporting period.

TABLE I.E.18. Summary of FCF Fuel Handling

	5/16/69 through 6/15/69	Total This Year
Subassembly Handling		
Subassemblies received from reactor		
Driver fuel (all types)	13	53
Experimental	1	7
Other (blanket)	1	2
Subassemblies dismantled for surveillance or examination		
Driver fuel (all types)	13	62
Other (blanket)	1	2
Driver-fuel elements to surveillance	753	2686
Number from subassemblies	13	62
Driver-fuel subassemblies transferred to reactor	5	32
Fuel-alloy and Waste Shipments		
Cans to burial ground	2	15
Skull oxide and glass scrap to ICPP	0	2
Recoverable fuel alloy to ICPP		
Fuel elements	3 (35 kg of alloy)	17 (278.4 kg of alloy)
Subassemblies	1 (2.9 kg of alloy)	3 (14.6 kg of alloy)
Nonspecification material	1 (13.3 kg of alloy)	5 (84.3 kg of alloy)

(v) <u>Experiment Handling and Interim Examination</u> (V. G. Eschen and N. R. Grant)

Subassembly XO66 was received from the reactor and dismantled. It contained two capsules with Mark-IA fuel elements irradiated to 3.75 a/o burnup (3.4 a/o peak burnup in Subassembly XO15 and an additional 0.35 a/o burnup in Subassembly XO66). The capsules were neutron radiographed and are being held for further examination.

The following experimental subassemblies were fabricated with new capsules and transferred to the reactor: XO64 (A-19), containing GE Group 5 mixed oxides; and XO67 (B-7), containing BNWL, ORNL, and GE structural materials.

PUBLICATIONS

Shape Pulse for RTL Circuit Use
    C. E. Cohn
        Electron. Eng. $\underline{28}$(6), 91 (June 1969)

Simple Turn-on Initialization for Digital Systems
    C. E. Cohn
        Electron. Design $\underline{17}$(13), 78-79 (June 21, 1969)

Selected Fission Cross Sections for ^{236}U
    W. G. Davey
        Nucl. Sci. Eng. $\underline{36}$, 434-435 (June 1969)   Note

Hot-Cell Determination of the Thermal Conductivity of Irradiated Reactor Fuels
    R. A. Di Novi
        Thermal Conductivity, Proc. 8th Conf., Purdue University, October 7-10, 1968, Ed. C. Y. Ho and R. E. Taylor. Plenum Press, New York, 1969, pp. 805-814

Accuracy of the Quasistatic Treatment of Spatial Reactor Kinetics
    K. Ott* and D. A. Meneley
        Nucl. Sci. Eng. $\underline{36}$, 402-411 (June 1969)

Detection of Transients in Nuclear Surveillance-Counting Channels
    K. G. Porges
        ANL-7470 (November 1968)

The Subroutine Used to Calculate Design Basis Accidents for the ZPR-6 and -9 Plutonium Safety Analysis Report (ANL-7442)
    G. K. Rusch and J. M. van Doorninck
        ANL-7508 (December 1968)

*Purdue University.

The Laser Microprobe Applied to the Investigation of Sodium Penetration into Stainless Steel
  E. S. Sowa
      Nucl. Appl. 7(1), 100-105 (July 1969)

The following appeared as abstracts in Trans. Am. Nucl. Soc. 12(1) (June 1969):

Performance of EBR-II Driver Fuel
  J. P. Bacca, F. G. Foote, G. C. McClellan, and J. H. Cook
      p. 90

Fission-Gas Release and Thermal Conductivity Measurements on U-5 wt % Fs Irradiated in CP-5
  W. N. Beck and R. J. Fousek
      pp. 78-79

Low Flux Measurements of ^{239}Pu and ^{235}U Capture-to-Fission Ratios in a Fast Reactor Spectrum
  M. M. Bretscher and W. C. Redman
      p. 265

Performance of Mixed-Oxide Fuel Elements with Center Melting
  F. L. Brown, L. A. Neimark, W. F. Murphy, and R. Natesh
      pp. 107-108

Automatic Testing of Analog-Digital Converters
  C. E. Cohn
      p. 313

A Computer-Controlled Microscope for Scanning Fission Track Plates
  C. E. Cohn, R. Gold, and T. W. Pienias
      p. 68

Symptoms Associated with a Loss-of-Bond-Type Defect in an EBR-II Driver Element
  R. M. Fryer, E. R. Ebersole, P. B. Henault, and R. R. Smith
      pp. 179-180

Identification of Failed Fuel Elements by Xenon Tag
  P. B. Henault, G. J. Bernstein, L. F. Coleman, E. R. Ebersole,
  W. J. Larson, and R. R. Smith
      pp. 102-103

Studies of Fast-Neutron Cross Sections through Integral Experiments
  J. M. Kallfelz, W. P. Poenitz, B. R. Sehgal, and B. A. Zolotar
      pp. 186-187

Sodium Void Effects in a 4000-Liter UO_2 Core, Assembly 6 of ZPR-6
  R. A. Karam, J. E. Marshall, L. R. Dates, and G. K. Rusch
      p. 270

Performance in EBR-II of Carbide Fuel Elements Irradiated to 7 at. % Burnup
   T. W. Latimer, F. L. Brown, and L. A. Neimark
      pp. 87-88

Measurement of the ^{239}Pu-to-^{235}U Fission Ratio in the Low keV Region
   W. K. Lehto
      p. 261

Preliminary Investigation of the Neutronic Characteristics of a Mixed-
Oxide Fuel Loading of EBR-II
   J. T. Madell and R. E. Jarka
      pp. 184-185

Linear Components of the Power-Reactivity Decrement of EBR-II
   J. T. Madell and R. E. Jarka
      pp. 277-278

Variance in the Doppler Coefficient due to Statistical Selection of Resonance
Parameters
   L. B. Miller and R. N. Hwang
      p. 274

Doppler Effect Studies as a Function of Reactor Spectra
   R. B. Pond and C. E. Till
      p. 272

Exposed-Fuel Calibration Studies in EBR-II
   R. R. Smith, C. B. Doe, and E. R. Ebersole
      p. 179

Fission Product Release from an Encapsulated U-Pu-Zr Ternary Alloy
Fuel Element
   R. R. Smith, E. R. Ebersole, R. M. Fryer, and P. B. Henault
      p. 180

Techniques for Alpha Measurement Using Null-Reactivity Methods in Fast
Critical Assemblies
   C. E. Till, L. G. LeSage, G. S. Stanford, E. F. Groh, and W. R. Robinson
      p. 266

Modeling Studies of Metallic Fuel; with Application to EBR-II Driver Fuel
Elements
   C. M. Walter and V. Z. Jankus
      pp. 90-91

II. OTHER FAST REACTORS--CIVILIAN--OTHER FAST BREEDER REACTORS

A. Fuel Development

1. Fuel Jacket Alloy Studies

   a. Fabrication Development of Fuel-jacket Alloys
   (N. J. Carson, Jr.)

   Last Reported: ANL-7561, p. 60 (March 1969).

   The effort to complete and consolidate data on the fabricability of vanadium alloys continued. Cooling-rate experiments were run with V-15 w/o Ti-7.5 w/o Cr alloy and with V-20 w/o Ti alloy; work-hardening and heat-treating experiments were run with V-10 w/o Cr alloy.

   In the cooling-rate experiments pairs of samples were heat treated for one hour at temperatures between 1000 and 1500°C. One sample of each pair was cooled slowly from the heat-treating temperature, whereas the other was cooled by oil quenching. The hardness values of the samples were measured with an Avery Hardness Tester on metallographically prepared specimens, and were plotted as a function of the temperature of heat treatment.

   The effect of cooling rate on the hardness of V-20 w/o Ti alloy is shown in Fig. II.A.1. Cooling rate has no effect on hardness for heat treatment at 1100°C and below; at higher temperatures the oil-quenched samples are slightly harder. The photomicrographs show the changes that occur in the nature of the second-phase particles. The sample slow-cooled from 1000°C has small second-phase particles distributed throughout the grains. In the sample slow-cooled from 1400°C, much of the second-phase material is in the form of small

Fig. II.A.1. Effect of Cooling Rate on Hardness of Heat-treated V-20 w/o Ti Alloy

platelets. The grain size produced by 1000°C heat treatment was between 6 and 7, and increased linearly to between 0 and -1 for 1500°C heat treatment for both the quenched and the slow-cooled samples.

The effect of cooling rate on the hardness of the V-15 w/o Ti-7.5 w/o Cr alloy is shown in Fig. II.A.2. The hardness increase on quenching was slightly greater and began at a slightly lower temperature than for the V-20 w/o Ti alloy. The grain size, which was between 7 and 8 after one hour at 1000°C, increased linearly to between 0 and -1 after one hour at 1500°C for both the quenched and the slowly cooled samples.
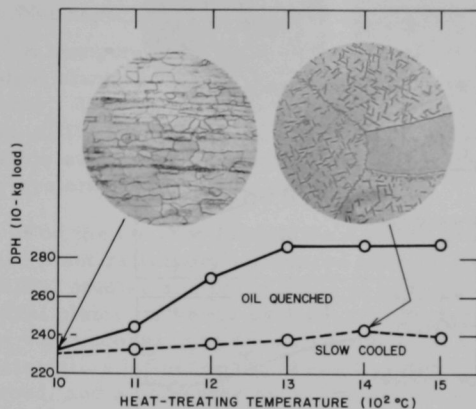
Fig. II.A.2

Effect of Cooling Rate on Hardness of Heat-treated V-15 w/o Ti-7.5 w/o Cr Alloy

Figure II.A.3 shows the hardness of the V-10 w/o Cr alloy as a function of reduction at room temperature. Reduction is in percent by area and was measured on rod stock that had been reduced by rolling. Hardness measurements were made with an Avery Hardness Tester on metallographically prepared specimens. The V-10 w/o Cr alloy, which had a relatively high initial hardness, did not harden extensively on working. Most of the hardening that did occur took place in the first 10% reduction. One anomalous hardness value was obtained at 60% reduction, but was not used in drawing the curve.

Fig. II.A.3.
Hardness of V-10 w/o Cr Alloy vs Degree of Reduction at Room Temperature
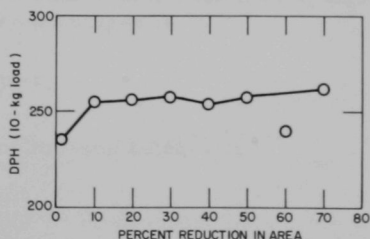
The effect of heat treatment on the hardness of the cold-reduced V-10 w/o Cr alloy is shown in Fig. II.A.4. The hardness slowly decreased with increasing heat-treatment temperature. Minimum hardness

was reached at about 1000°C. Photomicrographs of samples reduced 50% and heat treated at 900 and at 1100°C are included to show recrystallization behavior.
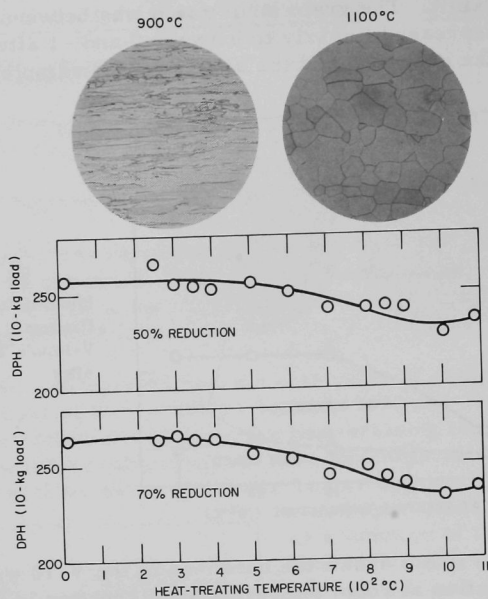
Fig. II.A.4. Hardness of V-10 w/o Cr Alloy Reduced 50 and 70% at Room Temperature and Heat Treated for One Hour

III. GENERAL RESEARCH AND DEVELOPMENT--
CIVILIAN--STUDIES AND EVALUATIONS

A. Evaluation of Fast Reactor Analysis Methods and Data

1. Model for Electrical-generated-system Reliability Analyses
(M. E. Stephenson)

Not reported previously.

A computer code is being constructed that uses characteristics of individual plant and utility electrical systems to assess system failure frequency. This code will: (1) provide a tool for investigating LMFBR impact on utility systems and guide LMFBR R&D activities by providing a means for evaluating plant characteristics, and (2) be incorporated into power-system projection analyses.

For the current 1000-MWe LMFBR studies reliability is important. Because plant reliability influences overall electric-generating-system reliability, studies are being made of how the unavailability parameters of individual plants influence overall-system reserve requirements. However, it first was necessary to develop a model of how individual-plant outage characteristics influence the overall system. An initial model has been developed, and a computer program written to perform many of the calculations involved in the model.

a. Method and Computer Program

The model makes use of a probability approach. The overall generating system is divided into subsystems. A number of plants are usually assigned to subsystem; however, the number of plants in the subsystem can be one if a single plant of special characteristics is to be considered. Each subsystem is characterized by a forced-outage rate p (forced down-time divided by scheduled operating time), an average repair time τ, the average plant capacity M, and the number n of plants in the subsystem. For the plants of a subsystem, the following equations apply; the probability of r simultaneous outages is

$$P_r = \frac{n!}{r!(n-r)!} p^r (1-p)^{n-r},$$

the average duration of r simultaneous outages is*

$$\tau_r = \frac{\tau(1-p)}{r + p(n-2r)},$$

and the magnitude of r simultaneous outages is

$$M_r = rM.$$

---

*Halperin, H., and Adler, H. A., Determination of Reserve-Generating Capability, Trans. AIEE, pp. 530-544

For each subsystem, p_r, τ_r, and M_r are calculated for all values of r from 0 to n. The subsystems are then progressively meshed together in combinations of possible outages according to the equations

$$M_{ab} = M_a + M_b,$$

$$p_{ab} = p_a p_b,$$

$$\tau_{ab} = \frac{\tau_a \tau_b}{\tau_a + \tau_b},$$

and

$$F_{ab} = \frac{p_{ab}}{\tau_{ab}},$$

where a and b represent the subsystems being meshed into the combination ab, and F_{ab} is the frequency of occurrence of an outage combination having a magnitude M_{ab}, a probability p_{ab}, and a duration τ_{ab}. The meshing is continued for all possible combinations and results in a set of M, F pairs for the entire system. These are then grouped in increments of outage magnitude according to the equations

$$F_g = \Sigma F, \quad p_g = \Sigma p, \quad \text{and} \quad M_g = \frac{\Sigma Mp}{p_g},$$

resulting in values of outage frequency F_g as a function of outage magnitude M_g. The increment of outage magnitude is approximately equal to the average size of all units in the system, as recommended by Adler.

So far this method is similar to the "loss-of-capacity" method used by some utilities. This part of the program was checked against results obtained in a similar way* and was found to be in good agreement.

Both the loss-of-capacity method** and the loss-of-load methods†️ use a probability approach in calculating forced-outage magnitudes. The loss-of-capacity method has the advantage that the actual frequency of forced outages is calculated, based on both probability and duration. In the loss-of-load method, only the probability is calculated; for example,

---

*National Power Survey, Federal Power Commission, 1964, Part I, p. 189.

**Ciesielski, E. E., and Lynskey, J. P., Application of Method: Probability of Loss of Generating Capacity, IEEE Winter Power Meeting, 1968; 68CP54-PWR.

†Electric Power in the Northeast, 1970-1980-1990, a report to the Federal Power Commission by the Northeast Regional Advisory Committee, December 2, 1968, Ch. V.

a loss of load of 1 day in 5 yr does not mean an actual frequency of once in 5 yr, but rather a probability of $1/(365 \times 5)$ (that is, it is assumed in the loss-of-load method that the combined forced-outage duration is 24 hr). It was felt desirable to use the frequency approach here, so the forced-outage magnitudes were calculated as in the loss-of-capacity method. With the above equations, the forced-outage frequency can be obtained as a function of the generating capacity forced out of the system. However, in the loss-of-capacity method, the computer program ordinarily does not take into account the variations in the load, as is done in the loss-of-load method.

It is believed that the variation in loads should be taken into account. The second part of the system-reliability-analysis model accounts for system load demand. Thus, from utility load curves, values of monthly peak loads as a fraction of the annual peak load are estimated. The daily peak loads over a month are also variable, and are taken into account by a probability or statistical approach.* Because weekend and holiday loads usually are considerably less than weekday loads, a month was considered to be composed of 21 weekdays. For these 21 days, equal probabilities were assigned corresponding to 21 equal areas under a normal (Gaussian) proba-bility curve of daily peak-load distribution over a month. Then 21 values of daily peak load were calculated based on the centers of each of these 21 areas. For example, 1 day a month the daily peak load is taken to be the monthly mean or average of the daily peaks. This load will last 1 day, and is represented by the center $1/21$ of the area under the bell-shaped normal distribution curve. For a second day, the load is taken to be the center of the next $1/21$ of the area under the curve to the right, or $m + 0.119\sigma$, where m is the mean of the daily peaks and σ is their standard deviation. For a third day, we use the center of the next $1/21$ of the area under the curve to the left, or $m - 0.119\sigma$. For a fourth and fifth day, the daily peak loads are taken to be $m + 0.241\sigma$ and $m - 0.241\sigma$, etc., until finally, for the 20th and 21st days, the daily peak loads are $m \pm 1.980\sigma$.

The highest of all the daily peak loads, $m + 1.980\sigma$, can now be set equal to the monthly peak for the month under consideration. To cal-culate each of the 21 daily peak loads, a value of σ must be used. Some studies* indicate that σ/m for utility daily variations is about 0.02 to 0.04.

The program calculates the 12 months of the year separately, not only because each monthly peak is different and the amount of capacity out for scheduled overhauling changes from month to month, but also because the system of plants whose forced outages are to be considered is different depending on which plants are out for scheduled overhaul. The distribution of scheduled overhauling is determined by placing relatively more of the overhauling in the "valleys" of the monthly load curve over a year, so that

---

*Miller, Andrew L., Details of Outage Probability Calculations, Trans. AIEE, pp. 551-557 (Aug 1958).

the total of monthly load and monthly scheduled overhauling is approximately constant over the year, except for the peak load months, in which there may be no scheduled overhauling assigned.

The final step is the calculation of system failure frequency. The critical value of forced-outage magnitude for any day, M_c, is obtained as the system capacity less the daily load and less any scheduled outage due to overhauling for the month being considered:

$$M_c = C_{system} - L_{daily\ load} - O_{planned\ outage}.$$

From this value of critical forced-outage magnitude, the frequency of occurrence is obtained from the frequency-outage function obtained previously. Then, a sum of all the daily values of frequency over all the months of the year is obtained. This can be expressed as the average interval between system failures, in years. For the "reference" system calculated below, this was approximately 5 yr.

b. Application to a Reference System and Parameter Studies

The program has been applied to a "reference" system, and certain parameters of the reference system were then varied to observe their effect. The reference system is composed of the following plants:

3 plants of 800 MW each;

5 plants of 600 MW each;

7 plants of 400 MW each;

9 plants of 200 MW each,

giving a total system capacity of 10,000 MW. The annual peak load was taken as 8,000 MW. A factor, f, by which this annual peak load can be multiplied was 1.00 for the reference case, but values of 1.01, 1.02, and 1.03 were also considered. The factor f takes into account lack of accuracy in estimating future peak loads. The reference case used a 2-2-2-4 week overhauling schedule, in which a plant would be on 2 wk/yr scheduled overhaul for 3 yr and then on 4 wk/yr scheduled overhaul for 1 yr. This was treated by assuming that, in the year being considered, approximately 3/4 of all the plants of a certain size would be on 2-wk scheduled overhaul, and 1/4 of the plants would be on 4-wk scheduled overhaul. The value of p, the individual-plant forced-outage probability, was taken to be the same for all plants, and was 0.05 for the reference case, but values of 0.04 and 0.06 were also considered. The value of σ/m, the ratio of standard deviation to mean for the daily peak load variation over a month, was taken to be 0.03 for the reference case, but values of 0.02 and 0.04 were also considered. A value of 150 hr was used for average repair time for a plant. The results are shown in Figs. III.A.1, III.A.2, and III.A.3.
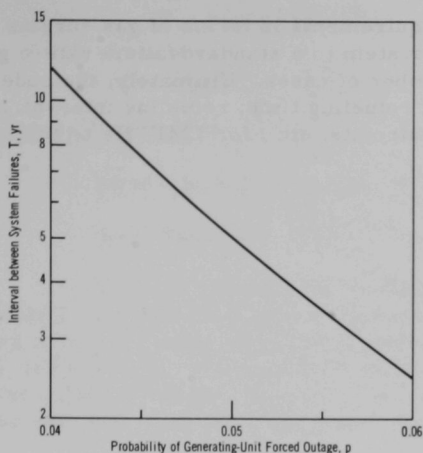
Fig. III.A.1. Effect of Plant Forced-outage Probability on Interval between System Failures. There is a shorter interval between system failures as the plant forced-outage rate, p, is increased.
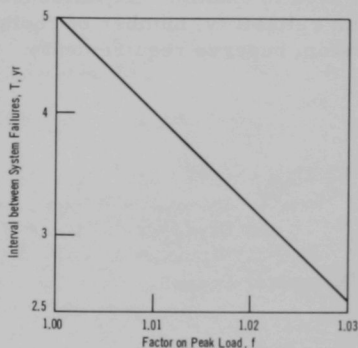
Fig. III.A.2. Effect of Factor Applied to Peak Load on Interval between System Failures. Even a small percentage increase in annual peak load decreases the interval between system failures rather sharply.
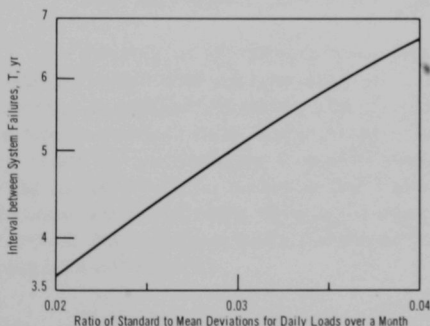
Fig. III.A.3

Effect of σ/m for Daily Load Variation over a Month on Interval between System Failures. It takes a fairly large percentage change in σ/m, from 0.03 to 0.02 (a decrease of 33%) or to 0.04 (an increase of 33%), to make any important change in the interval between system failures.

c.   Further Work.

A system is being calculated in which the individual-plant forced-outage probabilities are varied, with larger values of p assigned to the larger-size units and smaller values of p assigned to smaller units, in accordance with utility experience. Also being considered is a case with a "long" overhauling schedule, corresponding to 4-4-4-8 instead of 2-2-2-4 wk.

A review of reserve requirements in terms of gas-turbine units that will be required to return the system to a standard failure rate (e.g., once in 5 yr) will be calculated for a number of cases. Ultimately, the code will be used to examine the influence of refueling time, refueling interval, component reliability, number of coolant circuits, etc., for LMFBRs on the utility-system reserve requirements.

IV. GENERAL REACTOR TECHNOLOGY

A. Applied and Reactor Physics Development

1. Theoretical Reactor Physics

    a. Cross Section Data Evaluation (D. Meneley)

Last Reported: ANL-7577, p. 128 (April-May 1969).

Current versions of the ENDF/B codes CHECKER, CRECT, DAMMET, and SLAVE 3 have been received from Brookhaven. These codes have been made operational with both the CDC-3600 and the IBM 360 systems. The new CHECKER, CRECT, and DAMMET codes replace older versions. SLAVE 3 is a new code that averages tabulated cross sections from ENDF/B File 3 over various spectra.

A version of U-238 having inelastic scattering consistent with the cross sections of the old Set 224 has been added to the 3600 MC^2 library. This version has a smaller inelastic scattering cross section than that of ENDF/B over much of the energy range. The present MC^2 library for the 3600 contains 77 materials.

    b. Reactor Computation and Code Development (B. J. Toppel)

Last Reported: ANL-7577, pp. 128-134 (April-May 1969).

Testing of the two-dimensional diffusion perturbation module of the ARC system and its driver module began. Because other two-dimensional perturbation codes are unavailable, the perturbation computations are compared with diffusion computations. To reduce discrepancies arising from the limitations of perturbation theory, only small perturbations resulting in $\Delta k/k^2$ of the order of 10^{-4} are considered. The diffusion-theory calculations were run with very tight convergence criteria so that such small reactivity changes were calculated with a minimum accuracy of three significant figures.

The first batch of problems tested the module with respect to changes in the assignment of compositions to regions. The configurations considered are described in Table IV.A.1. Regions 1-4 represent the unperturbed configuration; regions 5-9 are portions of these regions in which the composition is changed from that given in the table to another composition. These compositions are the same as those used in the testing of the one-dimensional perturbation module (see Progress Report for February 1969, ANL-7553, pp. 77-80). For both the radial and axial directions, the boundary conditions are zero current at the lower boundary and zero flux at the upper boundary.

TABLE IV.A.1. Unperturbed Configuration for Testing of
Two-dimensional Perturbation Module

Region	Composition	r_{lower}	r_{upper}	z_{lower}	z_{upper}
1	1	0.0	56.80	0.0	52.220
2	2	56.80	137.60	0.0	52.220
3	3	137.60	181.80	0.0	52.220
4	4	181.80	227.60	0.0	52.220
5	1	51.12	56.80	0.0	4.5125
6	2	56.80	60.84	31.5875	36.10
7	3	137.60	142.02	31.8575	36.10
8	3	164.12	181.80	0.0	4.5125
9	4	181.80	190.96	0.0	4.5125

The perturbation calculations were made with the perturbation in the diffusion coefficient D defined in two ways. In the first definition the perturbation in D is simply the difference in D between the perturbed and the unperturbed system:

$$\delta D_1 = D' - D = \frac{-(\Sigma'_{tr} - \Sigma_{tr})}{3\Sigma'_{tr}\Sigma_{tr}}, \tag{1}$$

where Σ'_{tr} and Σ_{tr} are the transport cross sections for the perturbed and the unperturbed systems, respectively. The second definition is linear in the change in the transport cross section:

$$\delta D_2 = \frac{D}{D'}\delta D_1 = \frac{-(\Sigma'_{tr} - \Sigma_{tr})}{3\Sigma_{tr}\Sigma_{tr}}. \tag{2}$$

The comparison of perturbation with diffusion computations for changes in the assignment of composition to regions is given in Table IV.A.2. There is significantly better agreement between perturbation theory and diffusion theory when δD is defined by Eq. (2). With this definition the discrepancy is less than 1% for perturbations 1 and 2, and less than 2% for perturbation 4. Only for perturbation 3 is there serious disagreement between diffusion theory and the perturbation calculation using δD_2.

TABLE IV.A.2. Comparison of Two-dimensional Perturbation and
Diffusion Computations for Composition-Region Assignment Changes

		Composition		$\Delta k/k^2$		
Problem	Region	Unperturbed	Perturbed	Diffusion	Pert (δD_1)	Pert (δD_2)
1	5	1	4	3.624×10^{-4}	2.667×10^{-4}	3.629×10^{-4}
2	6	2	3	-5.210×10^{-4}	-5.385×10^{-4}	-5.189×10^{-4}
3	7	3	4	-3.12×10^{-5}	-1.165×10^{-4}	-8.194×10^{-6}
4	8	3	2	1.154×10^{-4}	1.119×10^{-4}	1.134×10^{-4}

Problems were also run to test the perturbation module with respect to changes in the concentration of isotopes. In each problem, the

concentration of one isotope in a different composition was changed. The results of these calculations along with a comparison with diffusion theory is given in Table IV.A.3. From the table it is seen that for the first two problems, in which the concentration of a fissile isotope is changed, the agreement between diffusion theory and the perturbation module is good. Here the change in leakage is minor, so both approximations to δD give essentially the same result. In the third problem, in which a nonfissionable isotope is removed from region 3, the change in leakage is more important, the agreement between diffusion theory and the perturbation module is somewhat poorer, and the use of δD_2 gives better agreement than the use of δD_1. In the last problem, the change in leakage is the dominant effect. Here there is serious disagreement between diffusion theory and perturbation theory, but again the use of δD_2 yields better results than the use of δD_1.

TABLE IV.A.3. Comparison of Two-dimensional Perturbation and Diffusion Computations for Isotope Concentration Changes

| Problem | Composition | Material[a] | Isotope | Concentration $(10^{24}/cm^3)$ | | $\Delta k/k^2$ | | |
				Initial	Perturbed	Diffusion	Pert (δD_1)	Pert (δD_2)
1	1	1	53 (^{235}U)	0.00003156	0.00003748	1.154×10^{-4}	1.1708×10^{-4}	1.1708×10^{-4}
2	2	2	55 (^{239}Pu)	0.0010974	0.0010970	-1.718×10^{-4}	-1.6988×10^{-4}	-1.6988×10^{-4}
3	3	8	38 (Ni)	0.0012822	0.0	-1.775×10^{-4}	-1.8850×10^{-4}	-1.8269×10^{-4}
4	4	9	35 (O)	0.0	2.0	2.37×10^{-5}	-3.3591×10^{-4}	7.9499×10^{-5}

[a]See Progress Report for February 1969, ANL-7553, Table IV.A.2, p. 78.

In both cases (problem 3 of the region-composition assignment changes and problem 4 of the isotope changes) where there was serious disagreement the dominant perturbation was the change in leakage. When the composition becomes more opaque, δD_2 yields larger reactivity effects for the change in leakage than δD_1, and when the composition becomes more transparent, δD_2 yields smaller reactivity effects. The true reactivity effect lies somewhere between the two, and when the change in leakage is the dominant perturbation the disagreement between diffusion theory and the perturbation module may be serious. However, at least from the comparisons that have been considered thus far, the use of Eq. (2) for the perturbation in the diffusion coefficient yields much better results than the use of Eq. (1).

2. Nuclear Data

    a.   Cross Section Measurements (C. E. Crouthamel and N. D. Dudey)

    (i)   Monoenergetic Neutron Cross Section Measurements

    Last Reported: ANL-7527, p. 95 (Dec 1968).

Cross-section values for the $^{89}Y(n,\gamma)^{90m}Y$, $^{85}Rb(n,\gamma)^{86m}Rb$, and $^{87}Rb(n,\gamma)^{88}Rb$ reactions have been determined, and the errors in the

absolute cross section for each datum point have been evaluated. These cross sections (see Tables IV.A.4, IV.A.5, and IV.A.6) have been measured relative to both ^{235}U(n,f) and ^{197}Au(n,γ) reaction cross sections. A detailed report on these measurements is being prepared for publication.

TABLE IV.A.4. Cross Sections for the ^{89}Y(n,γ)^{90m}Y Reaction

Neutron Energy (keV)	Energy Spread[a] (keV)	Cross Section[b] (mb)	Neutron Energy (keV)	Energy Spread[a] (keV)	Cross Section[b] (mb)
162	42.9	0.334 ± 0.023	783	38.2	0.511 ± 0.032
245	40.5	0.344 ± 0.018	843	37.8	0.535 ± 0.032
259	33.3	0.297 ± 0.021	853	91.8	0.572 ± 0.045
314	36.0	0.352 ± 0.021	899	31.2	0.495 ± 0.026
354	47.4	0.417 ± 0.029	943	42.9	0.401 ± 0.027
426	35.6	0.394 ± 0.029	976	45.4	0.417 ± 0.026
472	45.4	0.407 ± 0.032	1043	46.0	0.385 ± 0.024
509	74.1	0.409 ± 0.031	1106	44.9	0.324 ± 0.020
577	39.4	0.452 ± 0.028	1182	49.9	0.286 ± 0.018
636	35.8	0.466 ± 0.033	1230	76.2	0.264 ± 0.022
649	85.2	0.499 ± 0.039	1330	69.7	0.284 ± 0.020
723	39.7	0.486 ± 0.022	1449	51.3	0.297 ± 0.019

[a]One-half the full neutron energy spread.
[b]Errors quoted are the standard deviations in the absolute value of the cross section.

TABLE IV.A.5. Cross Sections for the ^{85}Rb(n,γ)^{86m}Rb Reaction

Neutron Energy (keV)	Energy Spread[a] (keV)	Cross Section[b] (mb)	Neutron Energy (keV)	Energy Spread[a] (keV)	Cross Section[b] (mb)
156	49.2	17.3 ± 1.69	827	65.4	8.19 ± 0.84
174	65.0	16.1 ± 1.72	889	56.3	8.72 ± 0.77
231	48.8	15.8 ± 1.82	904	56.4	7.68 ± 0.71
284	65.0	13.4 ± 1.30	922	81.9	8.46 ± 0.80
290	31.0	13.8 ± 1.26	980	69.0	7.45 ± 0.91
323	50.0	13.5 ± 1.38	1064	86.1	6.63 ± 0.62
413	51.7	13.4 ± 1.22	1070	81.3	7.20 ± 0.66
425	44.8	13.3 ± 1.56	1111	72.2	6.74 ± 0.90
456	57.4	13.5 ± 1.47	1141	88.4	7.15 ± 0.68
503	59.3	13.5 ± 1.28	1201	80.3	6.58 ± 0.61
546	52.6	11.3 ± 0.95	1220	90.8	6.78 ± 0.70
611	53.5	10.7 ± 1.07	1385	86.1	6.69 ± 0.65
649	63.7	10.1 ± 1.12	1393	89.6	6.41 ± 0.59
714	62.7	9.9 ± 1.03	1484	87.1	5.50 ± 0.52
776	54.3	9.56 ± 0.92			

[a]One-half the full neutron energy spread.
[b]Errors quoted are the standard deviations in the absolute value of the cross section.

TABLE IV.A.6. Cross Sections for the ^{87}Rb(n,γ)^{88}Rb Reaction

Neutron Energy (keV)	Energy Spread[a] (keV)	Cross Section[b] (mb)	Neutron Energy (keV)	Energy Spread[a] (keV)	Cross Section[b] (mb)
156	49.5	8.23 ± 0.81	776	54.3	2.97 ± 0.31
231	48.8	7.11 ± 0.71	827	65.4	2.63 ± 0.26
290	31.0	6.55 ± 0.66	904	56.4	2.64 ± 0.26
323	50.0	5.65 ± 0.57	980	69.0	2.71 ± 0.27
379	31.2	5.19 ± 0.49	1070	81.3	2.78 ± 0.27
425	44.8	5.24 ± 0.58	1111	72.2	2.63 ± 0.26
456	57.4	3.81 ± 0.38	1201	80.3	2.46 ± 0.25
467	59.8	4.20 ± 0.40	1297	50.1	2.47 ± 0.43
503	59.3	3.78 ± 0.38	1385	86.1	3.17 ± 0.32
572	55.3	3.59 ± 0.36	1393	89.6	2.64 ± 0.27
649	63.7	4.18 ± 0.43	1484	87.1	2.52 ± 0.25
714	62.7	2.99 ± 0.30	1561	89.4	2.84 ± 0.29

[a]One-half the full neutron energy spread.
[b]Errors quoted are the standard deviations in the absolute value of the cross section.

(ii) Low-mass Fast-neutron Fission Yields

Last Reported: ANL-7561, p. 67 (March 1969).

A series of experiments to measure the fission yield of tritium for the $^{232}Th(\alpha,f)$ reaction has been attempted with the tandem accelerator. Although no definitive results were obtained, the experiments provided information that will be very useful in designing future experiments.

Firstly, the experiments demonstrated that the particle identification system functioned according to expectations. Each low-mass particle up to ^6He was clearly resolved, and its energy spectrum was determined from a lower energy of 3 to 10 MeV (depending on the particle) to an upper energy level of about 40 MeV.

Secondly, the experiments pointed out several problems that must be solved before reliable fission-yield data can be obtained. In the presence of the high backscatter of the bombarding alpha particles, a fast coincidence (~ 10 nsec) between a tritium particle and a fission fragment was required to establish unambiguously that the observed tritium atoms were fission-produced. Further, the extremely low yield of tritium made it difficult to measure the timing of the coincidence system adequately. (It is necessary to detect about 10^7 fissions per detected tritium event.) As a result, the fission detectors deteriorated from radiation damage before a sufficient number of tritium events were recorded; therefore, a reliable tritium fission yield could not be obtained.

It is possible that such stringent timing requirements may not be necessary for measurements with fast neutrons. However, to prepare for the fast-neutron experiments, methods of off-line timing of the coincidence system and alternative methods of detecting fission fragments are being investigated.

b. Burnup Analysis and Fission Yields for Fast Reactors
    (R. P. Larsen)

(i) Determination of the Absolute Fast Fission Yields of
     Burnup Monitors and Nonfission Nuclear Transformations
     in a Fast Reactor

Last Reported: ANL-7561, pp. 65-67 (March 1969).

An experiment has been designed to measure the effective capture-to-fission ratio (alpha) for the three isotopes ^{239}Pu, ^{233}U, and ^{235}U in a neutron spectrum that emphasizes the 10-keV region. It is in this region that the greatest uncertainties in alpha exist. The basic concept is to perform an irradiation of sufficient length (~ 5 days) to produce (1) a change in ^{240}Pu, ^{234}U, and ^{236}U contents that can be adequately measured

mass spectrometrically (determination of the number of captures) and (2) an amount of the fission product isotope ^{140}Ba that can be adequately measured gamma spectrometrically (determination of the number of fissions). This irradiation will be carried out in the critical facility ZPR-3. The special loading of samples for the irradiation has been completed, and preliminary irradiations are now being carried out. The irradiation to measure alpha will be performed early in July.

(ii) Supplemental Determination of Absolute Fission Yields of Burnup Monitors for Fast Reactor Fuels

Last Reported: ANL-7561, p. 67 (March 1969).

The techniques that have been developed for the measurement of the number of fissions in the alpha experiment (see Sect. (i) above and ANL-7561, p. 66) are being evaluated for the determination of fast-fission yields of burnup monitors for fast reactor fuels. The evaluation will be made by determining the yield of ^{137}Cs from the thermal fission of ^{235}U. This method of evaluation was chosen because (1) the ^{137}Cs yield from the thermal fission of ^{235}U has been more accurately measured than any other fission yield, (2) reliable methods for determining ^{137}Cs are well-established (see below), and (3) an excellent ^{137}Cs standard is available. Preparations of the various materials required for this irradiation have begun.

The accuracy with which ^{137}Cs can be determined in samples of irradiated nuclear fuel is demonstrated by the results obtained as a part of a recent ASTM round-robin. Two irradiated fuel samples (one cooled 6 months, the other 2 years) were supplied to each participating laboratory along with a reference standard (Nuclear Chicago-ASTM ^{137}Cs standard). Three laboratories (Gulf General Atomics, Los Alamos Scientific Laboratory, and Argonne) chose to analyze the two samples by gamma spectrometry using lithium-drifted germanium diode-multichannel analyzer systems. The reported values* for the ^{137}Cs contents of these solutions, given below, show the excellent agreement of results of the three laboratories.

	^{137}Cs Content x 10^{-13} (atoms/ml)	
Laboratory	Sample 1	Sample 2
GGA	7.288	1.330
LASL	7.319	1.338
ANL	7.317	1.334
Average	7.308	1.334

---

*The results obtained by Gulf General Atomics and Los Alamos Scientific Laboratory were supplied through the courtesy of G. Buzzelli (GGA) and G. M. Matlack (LASL).

c.   Determination of Nuclear Constants (A. B. Smith)

(i)   Fast Neutron Cross Sections and Other Nuclear Constants

Last Reported: ANL-7548, pp. 85-86 (Jan 1969).

(a) Fast Neutrons Incident on Vanadium. The LMFBR-RDT program has expressed an explicit need for fast-neutron cross sections of vanadium. In direct response to this need a program of measurements has been completed and a formal report prepared (ANL-7564, to be published). The results are summarized here.

Total neutron cross sections and elastic and inelastic neutron scattering cross sections of vanadium have been experimentally studied. The total neutron cross sections were determined with good resolution ($\gtrsim 1$ keV) from 0.1 to 1.45 MeV. Differential elastic and inelastic scattering angular distribution have been measured at incident neutron-energy intervals of ≤ 10 keV from 0.3 to 1.5 MeV with incident neutron resolutions of ~20 keV. The inelastic excitation of states at 330 ± 10 keV and 926 ± 10 keV was observed. The experimental results have been interpreted in terms of the optical model and statistical concepts, inclusive of resonance-width fluctuations and correlations. The observed intermediate structure has been considered in the context of strongly overlapping resonances, distributions in resonance widths and spacings, and in terms of an intermediate optical model. Comparison has been made with previously reported experimental values and with the pertinent contents of the evaluated data file, ENDF-B.

(b) Fast-neutron Scattering Cross Sections of Hafnium, Gadolinium, and Samarium. This work, carried out in direct response to an RDT request, has been completed and a formal report prepared for publication.*

Elastic and inelastic neutron-scattering cross sections of elemental hafnium, gadolinium, and samarium were measured at incident neutron energies of 0.3 to 1.5 MeV. The experimental resolution was sufficient to resolve elastic and inelastic processes reasonably and to define individual inelastic cross sections for the most appreciably excited states. The total neutron cross sections were determined up to 1.5 MeV with resolutions of $\gtrsim 2.5$ keV. Within the precisions of the measurements all observed cross sections were relatively smooth functions of energy. The experimental results were compared with those obtained from calculations based upon both spherical and deformed optical potentials and statistical theory, inclusive of fluctuation corrections. The calculated results were descriptive of measured total, elastic scattering, and, to a lesser extent, inelastic scattering cross sections. Experimental and calculated results

---

*Submitted to Nuclear Science and Engineering.

were compared with previously reported measured values and with the contents of several evaluated neutron data sets employed in reactor design.

(ii) Fission Process Data

Last Reported: ANL-7548, p. 87 (Jan 1969).

Resonance Interpretation of the ^{239}Pu Fission Cross Section. A set of multilevel parameters for the fission cross section of ^{239}Pu has been obtained from the analysis of the Petrel fission data between 4 and 100 eV. The analysis was actually extended up to 150 eV, but it is believed that between 100 and 150 eV the parameters are very uncertain because of the poor resolution of the experimental data. Using the aforementioned parameters as a starting point, the analysis of the Saclay fission data between 40 and 100 eV has been taken up. The objective is to arrive at a consistent set of parameters for the fission cross section of ^{239}Pu.

A set of single-level R-matrix parameters has been obtained from the analysis of the Petrel fission data for ^{239}Pu between 90 and 230 eV. The analysis was performed using the Adler-Adler code. The R-matrix parameters were obtained from the Adler-Adler single-level parameters by assuming the same capture width ($\Gamma_\gamma = 0.040$ eV) for all levels. The analysis has yielded 56 levels as compared to the 37 levels listed in ENDF/B in the same interval. There are serious uncertainties associated with these parameters, however, mainly because of the poor resolution of the data. These single-level parameters will subsequently be used in self-shielding calculations.

d. Reactor Code Center (M. Butler)

Last Reported: ANL-7577, pp. 138-139 (April-May 1969).

Twelve additional program packages were incorporated in the Center library during June. Eight were for new programs, three were new or revised versions of existing library programs, and one was received from the ENEA Computer Programme Library.

The new codes include the RELAP2 program, which calculates flow, mass inventories, temperature, pressure, reactivity and transient power for the primary system of a water reactor during a reactivity excursion or loss-of-coolant accident. The Phillips Petroleum Company submitted an IBM-7044 version of this program (ACC No. 369). The Bettis Atomic Power Laboratory supplied two of the new programs: NOW1G to solve one-dimensional two-group diffusion and delayed-precursor equations using a shape-specified point kinetics approximation (ACC No. 371), and BL47, a plotting routine for plane structures for stress analysis studies (ACC No. 373). These are both operable on the CDC-6600. The Battelle-Northwest Laboratory 1DX one-dimensional diffusion code for generating

effective cross sections and fast reactor analysis on the UNIVAC 1108 has been incorporated as ACC No. 374. Brookhaven National Laboratory supplied ACC Nos. 376 and 377, the AVERAGE and SIGPLOT programs designed to calculate average cross sections from S- and P-wave data of the ENDF/B file 2 unresolved parameters and to calculate cross sections from resolved resonance parameter data using the multilevel Breit-Wigner formula, respectively. Both CDC-6600 and IBM-7094 versions of the BNL codes are available.

A CDC-6600 version of the MACH1 program (ACC No. 262) and an IBM-360 version of the TWOTRAN program (ACC No. 358) have been received from ANL. The ENEA program incorporated during June is the SPANDE code (E219) written for the IBM-7090 by UKAEA to analyze three-dimensional structures and piping systems.

During the first quarter of 1969, 245 program packages were distributed by the Argonne Center.

B. Reactor Fuels and Materials Development

1. Fuels and Cladding

a. Behavior of Reactor Materials

(i) Fuel Element Behavior Modeling

(a) Bubble Migration Analysis (R. W. Weeks and R. O. Scattergood)

Last Reported: ANL-7577, p. 140 (April-May 1969).

The line tension model used to predict bubble break-away size from dislocations due to the influence of a thermal-gradient driving force (see, for example, Eyre and Bullough[*]) can be refined by a more precise statement of the dislocation self-energy, and by approximately accounting for the elastic interaction between the two dislocation segments. When this is done, the estimated breakaway sizes for escape of a bubble from screw and edge dislocations are smaller than those previously predicted for a given thermal-gradient driving force. These models, however, implicitly assume that bubble breakaway is achieved only when the dislocation segments come together. Alternatively, the bubble breakaway sizes can be established from the results of the interaction-energy analysis between a bubble and a straight dislocation previously reported (see ANL-7577). When this is done, sizes for bubble breakaway from screw and edge dislocations are found to be larger than

---

[*]Eyre, B., and Bullough, R., J. Nucl. Mater. 26, 249 (1968).

predicted by the previous models. It thus appears that the interaction between a bubble and a dislocation is strong enough to stretch the dislocation considerably before bubble breakaway occurs.

(b) Swelling Mechanisms and Models for Oxide Fuel
(R. W. Weeks)

Last Reported: ANL-7577, pp. 140-142 (April-
May 1969).

The new computer model for predicting the in-pile behavior of cylindrical oxide-fuel elements (see Progress Report for January 1969, ANL-7548, p. 88) has been programmed in FORTRAN for the ANL IBM-360, and is now being debugged.

The program, called the Life in a Fast Environment code (LIFE) computes the temperature distribution, fuel and clad swelling, U-Pu migration, fuel-clad elastic and creep deformations, and the resultant stress-strain history of the element. The program formulation is based on a three-ring model for the fuel and allows inclusion of an initial fuel-cladding gap.

LIFE also models friction between the fuel and the clad in an approximate manner, checking whether stick or slip occurs at each time step, and allowing different amounts of axial strain of the fuel and clad.

b. Metal Fuels

(i) Fuel-element Performance (H. V. Rhude)

Last Reported: ANL-7577, p. 152 (April-May 1969).

Fission-gas samples from fuel Elements ND24, ND23, BA01, BC02, NC17, and NC23 have been submitted for analysis. The data on the fuel elements and their estimated burnups have been reported in ANL-7577.

Elements ND24, ND23, and BA01 were sectioned transversely; Elements ND24 and ND23 were sectioned longitudinally across areas where neutron radiography revealed a separation in the fuel column. A section from the area calculated to have the highest burnup in each fuel column has been submitted for burnup analysis. Metallographic examination has been completed on several of the sections, and specimens have been prepared for microprobe analysis.

Metallography showed that the fuel in Elements ND24 and ND23 swelled to the inside of the cladding, but there appeared to be no reaction between the fuel and the V-20 w/o Ti cladding. The fuel formed annular, but not concentric, zones. The central zone is pear-shaped, porous, and is surrounded by a less porous zone that extends to roughly three-fourths of the radius. The fuel in the outer fourth of the radius is extremely porous. These zones will be analyzed with the microprobe to determine the distribution of uranium, plutonium, zirconium, and selected fission products.

2. Techniques of Fabrication and Testing

a. Nondestructive Testing--Research and Development

(i) Development of Nondestructive Testing Techniques (C. J. Renken)

(a) Neutron Radiography (J. P. Barton)

Last Reported: ANL-7548, pp. 95-98 (Jan 1969).

(1) Test Standards. Because neutron radiography is fundamentally different from X radiography, a new and independent system of test standards needs to be developed. The requirements for test standards in neutron radiography are (1) to provide a measure of the characteristics of a neutron-radiography facility, and (2) to indicate the capability of neutron radiography to detect particular details in a given object. However, the range of objects that can be examined by neutron radiography is so varied that to satisfy the second requirement a special test would be required for each particular application. This study, therefore, deals only with the first requirement.

The characteristics of a neutron-radiography facility are as follows: (1) geometric unsharpness due to imperfect beam collimation, (2) inherent unsharpness of the detector system, (3) ratio of effects of neutron and gamma radiations, (4) ratio of thermal neutron to resonance-energy neutron effects, (5) fast-neutron influences, (6) beam intensity, (7) beam uniformity, and (8) presence of other influences, such as radiation scattered from surrounding objects.

A proposed standard test object that permits the measurement of neutron-facility characteristics has been designed. The test object consists of a frame with various absorbers mounted both adjacent to and at spaced intervals in front of the image plane. The area of the object perpendicular to the neutron beam measures 100 by 75 mm; the effective thickness is either 60 or 104 mm, depending on the choice of spacers.

Characteristics (1) and (2), together with the overall visibility of detail, are indicated by the images of cadmium absorber strips that have been drilled with holes of different known diameters and spacings, and by the images of sets of plastic and of cadmium wires. The strips and the wires are located both near and at intervals in front of the image plane. Densitometer readings from the neutron radiograph of the object provide a measure of characteristics (3), (4), and (5).

This standard test object has been evaluated by using a variety of neutron-radiography systems, the details of which are listed in Table IV.B.1. Figure IV.B.1 shows the correlations between the radiographic contrasts obtained with the standard test object and four beam facilities. These data were obtained with gadolinium direct-exposure radiography. A similar plot for the indium transfer method showed that when gamma effects are eliminated, the points lie more nearly on a single straight line. As an illustration of beam collimation effects and actual detail visibility, Fig. IV.B.2 shows a plot of visibility on the radiograph of

TABLE IV.B.1. Neutron Beams Used to Evaluate Test Standard

| Beam Designation	Input Aperture Dimensions (cm)	Beam Length (cm)	Dimension of Uniform Beam Area at Output (cm)	Thermal-neutron Flux (n/cm^2-sec)	Cadmium Ratio, Au (Bare) / Au (Cadmium)	Gamma Intensity (R/hr)
A	1.27[a]	224	15[a]	2.3 x 10^6	1.4	280
B	2.54[a]	224	15[a]	8.9 x 10^6	1.7	370
C	5.08[a]	224	15[a]	3.5 x 10^7	2.1	560
D	10.16[a]	224	15[a]	1.4 x 10^8	2.2	1,700
E	15.24[a]	224	15[a]	3.6 x 10^8	2.5	2,200
F	2.54[b]	229	10.16 by 6.35[b]	5 x 10^6	2.6	32
G	10.16 by 6.35[c]	229	10.16 by 6.35[b]	2.4 x 10^7	3.2	50

[a]Diameter.
[b]Square.
[c]Rectangular.
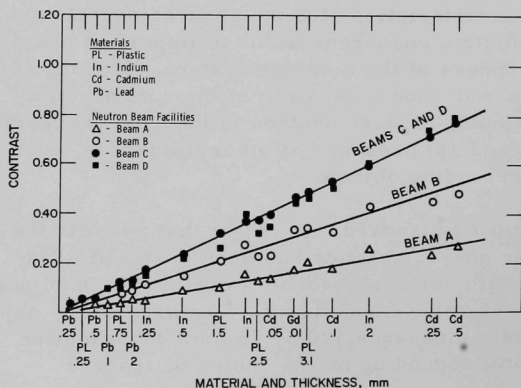
Fig. IV.B.1

Radiographic Contrast for Different Absorber Materials and Thicknesses, and for Different Neutron Beams. (Gadolinium foil, Kodak Single R film, direct exposure.) The locations of the materials along the abscissa axis were chosen so as to make the plot for Beam C linear.
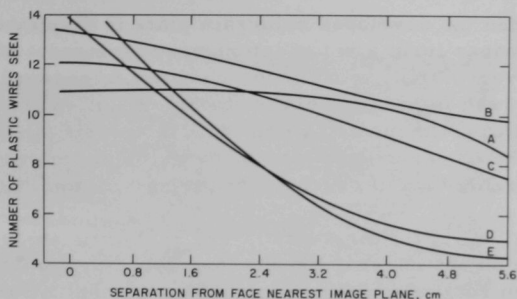
Fig. IV.B.2. Visibility on a Neutron Radiograph of Plastic Wires
             as a Function of Separation of the Wires from Face
             Nearest Image Plane for Different Neutron Beams.
             (Gadolinium foil, Kodak Single R film, direct
             exposure.)

plastic wire versus separation of the wires from the imaging plane. The
figure clearly shows that for small separations (corresponding to small
object thicknesses), low collimation is preferable, whereas for large
separations, high collimation is necessary. The high visibility for small
separations that is provided by low-collimation beams is due to the advan-
tageous neutron spectrum and neutron-to-gamma ratio. High collimation
is necessary for large separations in order to overcome geometric
unsharpness.

        Extensive graphs and analyses of results for this
test object are now available, and this should enable workers in the field
to assess the value of the system. The long-term goal is to have a universal
test standard that can serve to relate work done under different conditions.
No doubt, other laboratories will propose their own suggestions and modifi-
cations, and eventually an acceptable standard can be chosen. This test
standard is, therefore, presented, as a first suggestion, with this approach
in mind.

        (b) Laser Studies and Holography (N. Fernelius)

                Last Reported: ANL-7500, pp. 100-101 (Sept 1968).

                Holography is a means of recording a three-dimensional
image on a two-dimensional photographic plate. Holography is unique in
that it can provide a means for three-dimensional interferometry.

                Holographic interferometry can be accomplished either
by the double-exposure method or by the single-exposure real-time analysis
method. In the double-exposure method, a hologram of the object is recorded,
the surface of the object is displaced slightly (for example, by either mechan-
ical movement or thermal expansion), and a second exposure is made on the

same plate. When the developed hologram plate is displayed with laser light, the two images form a set of interference fringes. Where the displacement was very slight, broad, widely spaced fringes occur; where the displacement was greater, the fringes are finer, and may even exceed the resolution limit of the display system. The fringe pattern is not located at the surface of the object image, but somewhere else in space. Hence, there may be considerable parallax between the fringe system and the object.

In the single-exposure real-time analysis method, a hologram of the object is recorded and the photographic plate is developed. The plate is then returned to its original position relative to the object, with an accuracy to within a fraction of the wavelength of the recording light. If the hologram is sufficiently bright and the repositioning is done correctly, fringes are produced by interference between the object and the hologram image as the object surface is displaced.

Applications of these methods are shown in Figs. IV.B.3 and IV.B.4. Figure IV.B.3a is a photograph of a single-exposure hologram of a fuel-rod jacket that has been placed in front of a mirror. Figure IV.B.3b is a photograph of a double-exposure hologram; 20-psig air pressure was applied inside the capped jacket to expand it before the second exposure. Since the jacket tubing had been run through a tubing straightener, there was less strain along regions of work hardening. This may account for the helical fringe pattern that was formed. Another double-exposure hologram that was made of the same object in a horizontal position also showed a helical pattern. Therefore, the pattern must be caused by changes in the rod and not by some optical peculiarity.
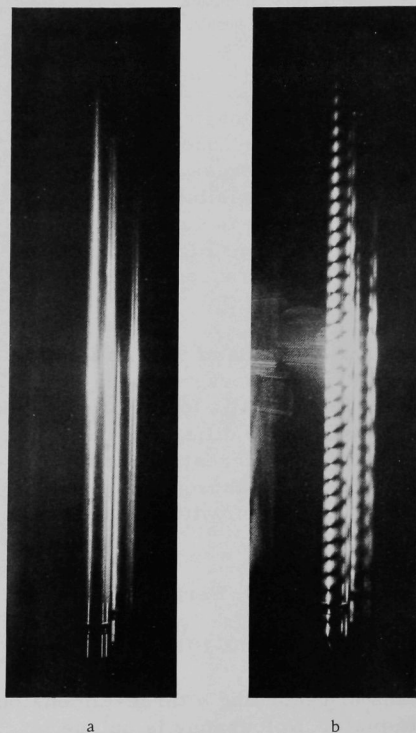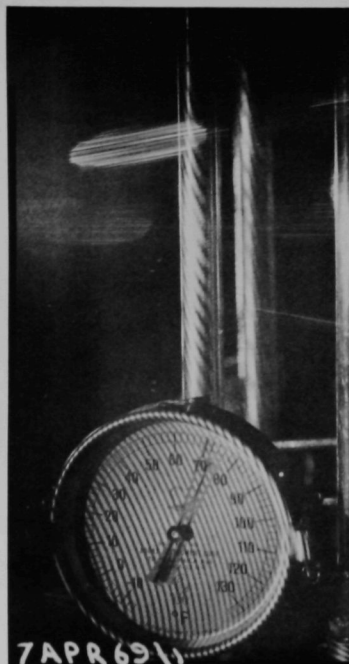

Fig. IV.B.3

Photographs of Holograms of a Capped Fuel-rod Jacket Placed in Front of a Mirror. (a) Single-exposure hologram; (b) double-exposure hologram with 20-psig pressure inside the jacket during the second exposure.

An alternative way of shifting the surface position of an object is to heat it. A heater consisting of a platinum wire run through a ceramic holder was inserted inside a jacket tube. Figure IV.B.4a shows a tube
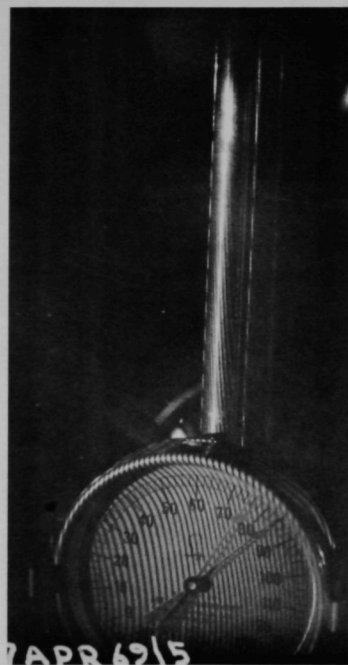
a   b   c

Fig. IV.B.4. Photographs of Double-exposure Holograms of a Jacket Heated between Exposures.
Temperature change between exposures (a) $\Delta T = 5^\circ F$; (b) $\Delta T = 8^\circ F$; and
(c) $\Delta T = 16^\circ F$.

that was heated from 70 to 75°F (ΔT = 5°F) between exposures. Note that under proper exposures the beginning and final temperatures of the attached thermometer can be recorded on the hologram. A fairly coarse set of fringes was observed. Figure IV.B.4b (ΔT = 8°F) shows a finer fringe system, indicating a larger displacement between exposures. In Fig. IV.B.4c (ΔT = 16°F) the fringes have disappeared almost completely. The tubes contained artificial defects used in calibrating eddy-current and ultrasonic testers; however, the effect of the flaws on the fringe system was negligible.

Real-time holographic interferometer studies were also made. No special precautions were taken to prevent shrinkage of the hologram emulsion during the developing process, yet we were readily able to reposition the hologram so that only a few widely spaced fringes were seen. Perfect repositioning would result in no fringes. Thus, the precautions to prevent emulsion shrinkage that are mentioned in some reports appear to be unnecessary. After the developed plate was repositioned, heat was applied to the tube and a conventional photograph was taken. Although the fringes were readily visible to the eye, considerable difficulty was encountered in photographing them. One difficulty was that the fringe system is not necessarily located in space at the surface of the object, and a large depth of field is required to get both the object and the fringe system in focus. At the low level of illumination provided by our laser, large apertures were necessary, which resulted in a small depth of field. Another difficulty encountered was that the fringe system drifted slowly during the photographic exposure (1/2 to 5 min), blurring the image of the fringes on the film.

For real-time analysis the problem of shrinkage of the hologram emulsion was much less severe than expected; the problem of making permanent conventional photographs of the readily visible real-time fringes was more severe than expected. The latter difficulty could be overcome by using a more powerful laser or by taking more stringent precautions to keep the plate holder and the object rigid.

C. Engineering Development

1. Development of Master-Slave Manipulator Systems (R. C. Goertz)

Last Reported: ANL-7548, p. 98 (Jan 1969).

a. <u>Mark-E4A Test and Modification</u>. Work on the Mark-E4A manipulator system concentrated on improving the reliability and ease of repair of the slave arm. Changes made included: (1) a better method of attaching a new Pitman arm to the hub of the large Y-motion drive gear (the old arm worked loose several times and had high stresses); preliminary tests indicated satisfactory performance; (2) new supports with eccentrics were designed and are being fabricated for the pinions at the output of the two servo drives for the Y- and Z-motions, which will make it possible to remove the drives without disturbing the gear meshes; with a few additional modifications on other components, any of the seven servo drives can be removed by another pair of Mark-E4As, thus reducing the cost and time required to repair the slave arm when it is "hot;" (3) the Y-motion pushrod is being redesigned to reduce backlash, reduce the torque it puts on the lower arm casting, and make it easier to remove and install (stress and deflections on the lower arm casting were too high with the old pushrod); (4) a new brake for the servo drives has been designed (it will hold the torque setting better and be easier to replace). Because the heat the present seven servo motors generate (about 440 W each) causes their load capacity to diminish, consideration is being given to replacing them with new motors of the types being developed, described below.

b. <u>High-performance Servomotor and Servo-system Studies and Tests</u>. The designs of several dc motors are being studied for possible use in the Mark-E4A or in future electric master-slave manipulators. Two motor sizes are of interest: for 50-lb-capacity and for 75-100-lb-capacity manipulators. Most of the motors are of the moving-coil type, but an inverted design (in which the rotor has a permanent magnet) also is being studied.

A motor of the moving-coil type was designed and built for testing design concepts. Only one layer of winding was used, and the flux density was low; otherwise, the motor worked well. The experience aided the solution of design and fabrication problems for subsequent models.

A second moving-coil motor has been designed and is being fabricated. Although it is smaller and lighter (weighs 12 lb) than the first model, it should have the needed high-performance merit factor of greater than 2000/sec (ratio of torque squared to inertia/watt), which will give a low effective mass (caused by the motor rotor inertia) at the manipulator arm and will keep heat generation moderately low. For example, use of a dc motor having a merit factor of 2000/sec in a manipulator having a load capacity of 95 lb would give a mass of about 2 lb due to the motor inertia

and generate a maximum heat (I^2R) of 100 W. This motor would not be the ultimate model needed, but would be an improvement and would be very useful in a practical manipulator.

Preliminary studies were made of inverted-motor designs using Alnico-9 or the new samarium-cobalt magnet material developed by Raytheon Co. Both materials show promise, but the studies show that the samarium-cobalt material looks better. Its availability is being investiaged.

    c.   Study of Remote Handling for LMFBR Facilities. Although the Mark-E4A manipulator system offers sufficient overall performance and reliability to be an economical investment for early LMFBR facilities, studies show that improvements would be desirable to provide: (a) better capability to perform remote maintenance and repair on complex machinery, which would require features such as higher load capacity, better grasping capability, and wider dynamic range of "feel," (b) different arm lengths to accommodate different facility needs, (c) smaller and lighter slave-arm assemblies that would be easier to support and move around the facility, (d) a need for less cooling at the slave arm so that it can be covered to reduce contamination, (e) demonstrated and proven greater reliability and ease of repair, and (f) a lower price.

Although no manipulator system can be made 100% reliable, a manipulator system (which includes a pair of manipulators, a slave-TV, support system, electric cabling, and a crane) can be made 100% dependable by designing the facility, support, and electrical cables such that the manipulator system can be removed readily for repair, or by providing multiple manipulator systems to obtain redundancy an interrepair capability. A larger facility (costing about $10,000,000) that is used for general-purpose remote handling can be made 100% dependable by installing several pairs of slave arms, each with slave-TV, a crane, and a support system designed such that one pair of manipulators can repair or remove all parts of another manipulator. The large facility might have three pairs of manipulators for triple redundancy, interrepair capability, and a service cell above one end of the main hot cell so that one slave system (arms, support boom, slave-TV, and the carriage with its crane) can be removed for repairs.

The use of general-purpose electrical master-slave manipulators in an LMFBR facility can permit economies in special-purpose equipment and time to accomplish new remote-handling tasks, as well as leading to facility simplifications, higher plant factor, and shorter schedules for designing and building the plant.

2. Instrumentation and Control

    a.   Boiling Detector (T. T. Anderson, R. H. Selner, and S. L. Halverson)

    (i)   Acoustic Method

        Last Reported: ANL-7561, pp. 75-76 (March 1969).

        (a) High-temperature Detector Development. An experimental high-temperature acoustic sensor has been evaluated for bond integrity of the crystal-metal surfaces and for transducer sensitivity in liquid sodiu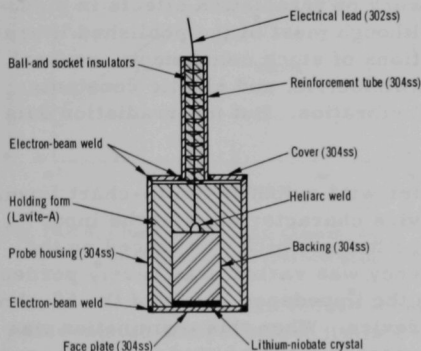m. The sensor is composed of a 1-cm^2 lithium niobate plate sandwiched between a stainless steel diaphragm and a stainless steel backing member (see Fig. IV.C.1). The lithium niobate was first coated with a fired frit composition of platinum, palladium, and gold, then brazed into the assembly with the eutectoid alloy of 82% gold and 18% nickel. A solid wire brazed to the top of the backing member carries the electrical signal; the sheath of the transducer functions as the signal return path.

Fig. IV.C.1. Cross Section of High-temperature Acoustic Sensor

The transducer was calibrated in sodium by indirect methods because equipment for absolute calibration has not been constructed. The acoustic signal to the high-temperature sensor was provided by a 1-MHz-resonance PZT-4 crystal mounted on the cool end of a 1/2-in.-dia stainless steel rod that extended into the sodium pot. A radiofrequency generator drove the PZT-4 crystal to produce an acoustic signal that propagated down the rod into the sodium. Immersed in the sodium, the high-temperature sensor picked up this acoustic signal and converted it to an electrical signal. After considerable charge amplification (8 V/pC), the signal was displayed on an oscilloscope.

        Simultaneously with the acoustic calibration, leakage resistance was measured from the sensor center wire to the sheath. The resistance decreased in the usual exponential manner with increasing temperature, but a large step change occurred after an overnight thermal soak at 320°C. There was evidence of acoustic response up to 670°C, after which response became intermittent and the electrical resistivity indicated that open circuits were occurring. Cooling to 350°C returned the transducer to an operating condition, although rapping the sodium container could induce

intermittent operation. Over the next 3 days, one thermal cycle was performed between 120 and 550°C. Then the sensor was operated satisfactorily for 5 days at 400°C. After removal from the sodium pot, the sensor was neutron- and X-radiographed, which showed a large gap (3/16 in.) between the backing member and the fragmented crystal. Differential thermal expansion is suspected as contributing to the failure, since forces were evidently sufficient to break a ceramic-to-metal feedthrough joint at the top of the sensor. Subsequent disassembly showed that the crystal bonding strength had been adequate despite incomplete wetting by the braze alloy.

(b) <u>Irradiation Tests of Piezoelectric Materials</u>. Problems associated with experimental evaluation of lithium niobate as a piezoelectric transducer material in a liquid-metal ($>650°C$) high-gamma ($>10^8$ R) environment are being defined. Previous work on irradiation effects in piezoelectric materials is being studied. Although most of the published literature concerns before-and-after evaluations of stock components, several papers report effects on piezoelectric, dielectric, and elastic constants, and on annealing defects by mechanical vibration. But no irradiation data were available for lithium niobate.

An impedance meter with output in Smith-chart format was evaluated to determine crystal-device characteristics at the input terminals. The motion of the impedance locus, which was traced on the Smith-chart presentation unit as frequency was varied, was barely perceptible because of the great difference in the impedance levels of the 50-ohm reference termination and the crystal device. When this termination was replaced by a 100-pf capacitor, the impedance locus shifted from the periphery of the Smith chart to the center, where the locus gyrations (characteristic of resonances) were clearly visible. The first resonance-circle maximum occurred at the predicted 3.4-MHz longitudinal crystal resonance. No assurances could be given by the vendor as to the interpretation of the readout with a variable reactance reference termination.

As a first step in evaluating the effect of radiation on lithium niobate, it was decided to perform before-and-after irradiation tests to establish the dose required to damage very-high-grade crystals. Crystals were irradiated with electrons from a Van de Graaff accelerator to simulate gamma-ray damage. The electron energy was 1.3 MeV, sufficient to penetrate the volume of 0.975-mm-thick by 1-cm-dia crystals. Laser-grade crystals of two compositions were tested: (a) stoichiometric, and (b) excess lithium-content for high-phase-match temperature of the $1.08-\mu$ He-Ne laser.

Electrical measurements with the crystals included dielectric constants, and resonance and antiresonance frequencies to obtain an electromechanical coupling coefficient. Two disks of Z-cut lithium niobate, high-phase-match material, were subjected to the irradiation by

1.3-MeV electrons in decade steps from 2.86 MR to 2.86 x 10^3 MR. All irradiations and measurements were performed at ambient temperatures of approximately 24°C. The electrical measurements were made with an impedance bridge. The measurement variables were constant-stress dielectric constant ϵ_T, limiting dielectric constant ϵ_{lim}, antiresonant frequency f_{ar}, and resonant frequency f_r. An electromechanical coupling coefficient k was obtained from the transcendental expression: $k^2(1 - k^2)^{-1} = \pi/2(1 - \Delta f/f_r)$ $\tan(\pi\Delta f/2f_r)$, where $\Delta f = f_{ar} - f_r$. The square of k is a measure of the
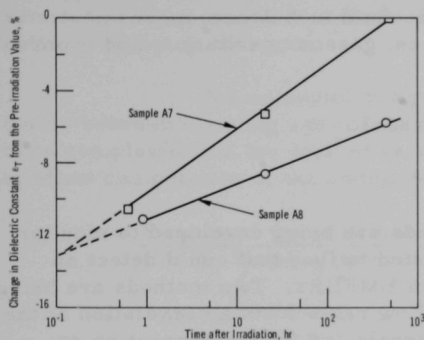

Fig. IV.C.2. Change in Dielectric Constant ϵ_T at Room Temperature after Beta Irradiation

interaction between elastic and electric energy by the crystal. The k remained relatively constant at 11% with accumulated dose up to 2.86 x 10^3 MR. The lowest compressional-mode resonant frequency remained constant at 3.679 MHz. Immediately after irradiation, the dielectric constant ϵ_T decreased about 14% and then returned toward the initial value with time, as shown in Fig. IV.C.2. These electrical measurements suggest that the piezoelectric properties are preserved under beta irradiation, although some changes might be occurring in crystal dimensions or structure.

To induce local strain, a third disk of the Z-cut, high-phase-match temperature, lithium niobate was subjected to the electron irradiation on half its surface, while the rest was shielded by an aluminum absorber. Optical examinations of strain, changes in birefrigence, optical path, reflectivity and optical transmission, evidence of cracking, discharge, and other destruction were made. After 28.6- and 286-MR irradiations, the material colored only slightly, turning a barely noticeable mauve. Development of strain was indicated by a slight dimensional change. Both optical transmission and apparent reflectivity decreased, but no evidence was found of any gross destruction within the crystal.

If lithium niobate had behaved as a salt, radiation would have caused rapid deterioration. But these preliminary data indicate that it is quite stable to radiation, and in this way behaves more like the stable oxides; rapid destruction does not occur.

Additional irradiation tests with the Van de Graaff are extending these results, operating lithium niobate as a transducer in a radiation environment to determine the tolerable dose rate for noise rejection, and comparing the behavior of stoichiometric lithium niobate with that of quartz.

For future gamma-irradiation tests, a cobalt-60 facility will be used. It will provide a maximum dose rate of 40 MR/hr in a 3-in.-dia cylindrical region. Thus it can simulate the ~1-MR/hr gamma dose rate in the EBR-II upper plenum, as well as the ~10^{-3}-MR/hr dose rate in the sodium coolant outside the reactor vessel.

(c) <u>Sound Measurements in EBR-II</u>. The data from flow-induced acoustic tests in hydraulic systems are being evaluated. Typical noise sources that could be involved are fluid turbulence, mechanical vibration, edgetones, quadrupole sources, gaseous cavitation, and vaporous cavitation.

b. <u>Flow Monitor</u> (T. T. Anderson)

Not previously reported.

New and imaginative methods are being developed to monitor in-core coolant flow or phenomena related to flow that could detect an imbalance between cooling and power in LMFBRs. Two methods are being investigated: (1) deduction of in-core flow rates from a correlation of the time shift between two thermocouple signals and (2) the generation or transmission of audio or ultrasonic frequencies proportional to flow by orifice or fluid-amplifier techniques. Measurement of flow by acoustic methods and transmission of the acoustic information within liquid-metal-cooled fast reactors are being investigated. One method employs a hydrualically driven fluidic device to measure and to telemeter acoustically the flow information to be sensed remotely from the core region. This type of device has the advantage of requiring no electrical leads at the measurement location in the reactor environment. A subcontract was awarded to Genge Industries to determine the feasibility of producing prototype flowmeters.

3. <u>Heat Transfer and Fluid Flow</u>

a. <u>Heat Transfer in Liquid Metal Cooled Reactor Channel</u> (R. P. Stein and J. V. Tokar)

Last Reported: ANL-7577, pp. 163-164 (April-May 1969).

(i) <u>LMFBR High-flux Operation and Its Consequences</u>. The superstructure for the loop is completely finished. All the components required for the loop have been completed and delivered, except the vacuum chamber, which has been fabricated but requires vacuum testing. The heat exchanger has been located within the loop structure; the air blower for the heat exchanger has been mounted in place.

The detailed piping flexibility analysis (see Progress Report for November 1968, ANL-7518, p. 97) has been completed and is being evaluated.

4. Engineering Mechanics

a. Anisotropic Thermoelasticity Studies (R. A. Valentin)

Last Reported: ANL-7577, p. 165 (April-May 1969).

(i) Isotropic Solutions for Comparison. The computer code needed to evaluate the stress and displacement expressions for the axially symmetric deformation of a finite-length, traction-free, heat-generating cylinder is being debugged.

The computer program needed to study the pressure distribution between cladding and fuel in the region near the end of the fuel has been completed (for the case of zero interface shear). It is being modified to allow computation of the complete stress state within the fuel in this region.

b. Structural Dynamics Studies--Parallel-flow-induced Vibrations (M. W. Wambsganss, Jr., P. L. Zaleski, and S. S. Chen)

Last Reported: ANL-7577, pp. 166-169 (April-May 1969).

(i) Structural Dynamics Test Loops

Last Reported: ANL-7577, p. 166 (April-May 1969).

The piping of the small loop has been completed; the support structure for the test section and the control system are under construction.

(ii) Flowtest Single Cylinders

Last Reported: ANL-7561, pp. 78-79 (March 1969).

Displacement- and pressure-time data obtained from single-element flowtests were processed on a spectrum analyzer and the results presented as mean-square-value spectral densities. These representations were used to determine the frequency distribution of the mean-square value and, by integration, the mean-square value (see Progress Report for November 1968, ANL-7518, pp. 101-102). Such representations also permit identification of frequency bands of energy that often in turn can be associated with various excitation sources. Although this information is very useful, to complete the description of the random signal, the amplitude distribution must be studied. For example, two random motions can have the same rms value, but one could have extreme peak amplitudes relative to the other. The probability law can describe the signal to the degree required by computation of a sufficient number of moments. Amplitude analysis also presents data in a form directly useful and meaningful in the study of stress and fatigue.
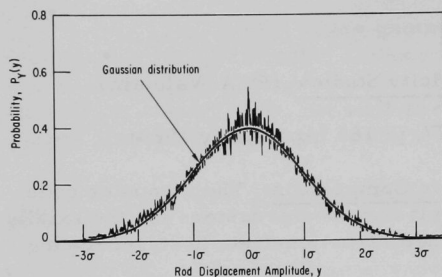
Fig. IV.C.3. Typical Probability-density Representation of Displacement of Single Tube Vibrating in Parallel-flowing Fluid (σ = rms value = 2.34 mils, and $\bar{u}$ = 16 ft/sec)

Data stored on tape from earlier tests were processed on an amplitude-distribution analyzer to gain insight into the law of statistical distribution of amplitudes measured in single-element tests in parallel flow. The shapes of the curves that were obtained suggest a normal or Gaussian distribution. As shown in Fig. IV.C.3, which is a typical probability density representation of tube vibration, the Gaussian probability law approximates the data quite well.

If, based on this agreement, we assume a Gaussian distribution for the distribution of vibration amplitude in a given direction in parallel-flow excitation of a cylindrical rod, we can write the probability law as

$$p_Y(y) = \frac{1}{\sqrt{2\pi} \, \sigma_y} \exp\left[-\frac{1}{2}\left(\frac{y}{\sigma_y}\right)^2\right],$$

which assumes a mean value of zero (σ_y is the standard derivation). The further assumption that motion in all directions is equally probable implies that the variables w and y (w presents rod motion in a direction perpendicular to the y direction) are independent random variables. Their joint probability function can be written as the product of their individual probability-density functions. This result is useful in determining the probability law governing the vector displacement (r, θ), where $r = (w^2 + y^2)^{1/2}$ and $\theta = \tan^{-1}(y/w)$.

Under the assumption that all directions are equally probable, the angle θ follows a uniform probability law

$$p_\theta(\theta) = \begin{cases} \dfrac{1}{2\pi}, & 0 < \theta < 2\pi \\ 0, & \text{otherwise.} \end{cases}$$

If we assume the standard deviations to be the same for motion in the two orthogonal directions, viz., $\sigma_w = \sigma_y = \sigma$, the integration required to compute $p_R(r)$ is greatly simplified and we obtain a Rayleigh distribution:

$$p_R(r) = \begin{cases} (r/\sigma^2 \exp\left[-\frac{1}{2}\left(\frac{r}{\sigma}\right)^2\right], & r > 0 \\ 0, & r \leq 0. \end{cases}$$

Its mean, mean-square, and variance in terms of the standard deviation σ are, respectively,

$$\bar{r} = \sqrt{\frac{\pi}{2}}\, \sigma; \qquad \bar{r}^2 = 2\sigma^2; \qquad \sigma_r^2 = \left(2 - \frac{\pi}{2}\right)\sigma^2.$$

The probability of the rod displacement exceeding a specified value $\lambda\sigma$ can be written as

$$P[r > \lambda\sigma] = \int_{\lambda\sigma}^{\infty} dr\ (r/\sigma^2)e^{-\frac{1}{2}(r/\sigma)^2}.$$

The integral has the following numerical values:

λ	$P[r > \lambda\sigma]$, %
0	100
1	60.7
2	13.5
3	1.2

A vibration amplitude greater than 3σ is attained only 12 times in 1000. Nevertheless, a rod vibrating at a frequency of 50 Hz will experience 360,000 peaks per hour, hence will attain a vibration amplitude greater than 3σ, 4320 times per hour. Such amplitudes can contribute to wear and impacting of adjacent elements.

(iii) Damping Analysis

Last Reported: ANL-7577, p. 166 (April-May 1969).

The effect of flow velocity on the damping of a cylindrical rod in parallel flow is being studied analytically. With an equation of motion derived by Paidoussis* and employing a one-mode approximation, the relationship between the damping factor ζ and mean axial flow velocity $\bar{u}$ was obtained as

$$\zeta = \zeta_0 + NU, \tag{1}$$

---

*Paidoussis, M. P., Dynamics of Flexible Slender Cylinders in Axial Flow; Part I. Theory, J. Fluid Mech. 26(4), 717-736 (1966).

where

$$N = \frac{\epsilon C_N \beta}{4\left\{\omega\left[\omega - \left(1 - \frac{1}{4\epsilon C_T}\right)U^2 + \frac{1}{2} - \Gamma\right]\right\}^{1/2}};$$

$$\epsilon = \ell/d;$$

$$\beta = \left(\frac{M}{M+m}\right)^{1/2};$$

$$U = \left(\frac{M}{EI}\right)^{1/2}\bar{u}\ell;$$

$$\Gamma = \frac{T\ell^2}{EI},$$

and where ζ_0 is the damping factor for zero flow velocity, ℓ is cylinder length, d is cylinder diameter, m is the mass of cylinder per unit length, M is added mass of fluid, EI is the flexural rigidity of the cylinder, T is axial tensile force, C_T and C_N are drag coefficients, and ω is nondimensional frequency of the fundamental mode.

For a relatively small flow velocity and a "representative" value of ϵC_T (say, $\epsilon C_T = 1$), N can be considered a constant:

$$N \approx \frac{\epsilon C_N \beta}{4[\omega(\omega + \frac{1}{2} - \Gamma)]^{1/2}}. \tag{2}$$

This implies that the damping factor is proportional to mean axial flow velocity and agrees with the experimental results in Fig. IV.C.4, discussed in ANL-7577.

For the experiment setup we have $\epsilon = 72$, $\beta = 0.574$, $U = 1.34 \times 10^{-2}\bar{u}$, $\Gamma = 0$, and $\omega = 22.4$. Substitution in Eqs. (2) and (1) yields

$$\zeta = \zeta_0 + (6.1 \times 10^{-3}C_N)\bar{u}, \tag{3}$$

where u has units of ft/sec. The value of the normal drag coefficient C_N is not known. Paidoussis suggests 0.018 as a "reasonable" value. Use of the experimental results in Fig. IV.C.4 to calculate C_N from Eq. (3) gives C_N equal to 0.087 and 0.24 from the bandwidth and modal-magnification methods of measuring damping, respectively. To obtain agreement with Paidoussis' damping model requires a drag coefficient approximately an order of magnitude greater than the value he suggests as reasonable.
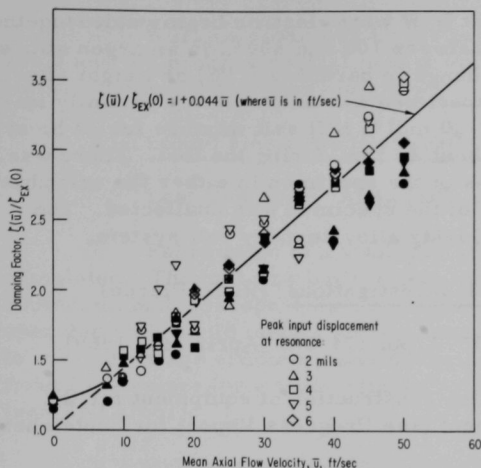
Fig. IV.C.4

Damping Factor as a Function of Mean Axial Flow Velocity (open symbols show values computed by modal-magnification method, $\zeta_{EX}(0) = 0.033$; solid symbols show values computed by bandwidth method, $\zeta_{EX}(0) = 0.012$)

The exact explanation for the flow-velocity dependence of the damping is not fully understood. It is likely that the damping model is more complex than that derived from Paidoussis' equation of motion. A study to identify the damping mechanism and significant parameters is continuing.

D. Chemistry and Chemical Separations

1. Closed Cycle Processes--Compact Pyrochemical Processes

a. Laboratory Process Development (I. Johnson)

Last Reported: ANL-7561, pp. 84-85 (March 1969).

A liquid Cu-Mg-Ca alloy is used in the reduction step of the salt-transport process for the recovery and purification of fast breeder reactor fuels. The phase relations of this alloy are being investigated to provide more complete information on the factors influencing the reduction reaction. Electron-microprobe examination of the Cu-Mg-Ca alloy indicated the presence of two intermetallic compounds: $CaCu$ and Ca_2Cu.

b. Process Engineering Studies (R. D. Pierce)

Last Reported: ANL-7577, p. 174 (April-May 1969).

Various materials of construction are being tested for use in vessels and other components for pyrochemical processing of fast breeder reactor fuels.

Two pieces of Mo-30 wt % W were electron-beam welded together, and thermally cycled three times between 100 and 800°C in an argon atmosphere. There was no significant change in hardness (~1%) or weight after the thermal cycling. The welded specimen was subsequently partially immersed in a $MgCl_2$-30 mol % NaCl-20 mol % KCl salt mixture for 24 hr at 700°C. The melt was agitated at about 25 rpm during the test. There was no detectable effect on the hardness of the specimen in either the salt phase or the vapor phase, and the weight of the specimen was unaffected. The specimen will be tested next in a Cu-Mg alloy/ternary salt system.

c.   Experimental Flowsheet Investigations   (R. D. Pierce)

Last Reported: ANL-7577, pp. 174-175 (April-May 1969).

Work is continuing on the construction of equipment for the Plutonium Salt Transport Experiment (see Progress Report for September 1968, ANL-7500, p. 115).

The stainless steel outer shells for the three transfer lines for glovebox 3 are being fabricated, and machining of Mo-30 wt % W parts, such as couplings for the lines, is continuing. A Hastelloy X vessel has been ordered for the high-temperature vacuum operations in box 3.

Preliminary induction-heating tests of the vessels in glovebox 3 have been completed. The heating tests provided information on the number of coils that are required to couple properly to each vessel and also demonstrated that the cooling water provided to the vessels' flanges was adequate. The vessels have been bolted to the mating flanges of the glovebox and insulated. The induction coils have been wound and installed.

Electrical work inside box 3 has been completed, and all process equipment except the transfer lines has been installed. The windows are being installed, and leak checking of the box, purification system, and associated piping will follow.

Drafting work for the inlet air-filter panel for box 3 is under way, and drafting for the filter panels for the ends of the subbox enclosure is nearly complete. The drawings for the outlet air panel and plenum were completed, and sent to the shops for fabrication.

A mechanism is being designed for moving an 80-kg processing crucible of tungsten through the lock (7) between boxes 3 and 4. The crucible will be placed on a cart that will move on portable rails extending from the lock into both boxes. The crucible can then be lifted on and off the cart with the hoists inside the gloveboxes.

Work is under way on the processing piping manifolds under box 3 and the process control panels for box 3. All of the electrical work inside glovebox 4 has been completed.

d. Liquid Metal-Molten Salt Contactors (R. D. Pierce)

Last Reported: ANL-7561, pp. 86-87 (March 1969).

Fabrication of a stainless steel mixer-settler unit has been completed. The unit was built to test the design proposed for use in the Plutonium Salt Transport Experiment (see Sect. c above). The unit will be operated with liquid metals and molten salts at 650°C, and will be used to measure stage efficiency and to verify operating parameters projected from low-temperature tests with water and water-organic systems (see ANL-7561).

Orifice sizes for the pump inlet and metering cup have been selected, and calibration of the apparatus with water has been completed. The unit was heated to 670°C to check the alignment of the moving parts at temperature, and was degassed in preparation for the addition of the metal and salt charges that are being prepared. After the unit has been charged with salt and metal, shakedown runs will be performed, which will be followed by metal-salt extraction experiments.

e. Decladding and Fuel Resynthesis (R. D. Pierce)

Last Reported: ANL-7577, pp. 175-176 (April-May 1969).

Recent laboratory experiments (see ANL-7577) have indicated that a Sb-17.3 at. % Cu alloy may be an attractive alternative to zinc as the decladding solvent in the pyrochemical process currently under development.

In the latest experiment, a sample of Type 304 stainless steel was exposed to a Sb-18 at. % Cu alloy at 900°C for one hour. The experimental conditions were identical to those used in a previous set of experiments (see Progress Report for September 1968, ANL 7500, pp. 117-118) in which Zircaloy-2 and Types 304 and 316 stainless steel were dissolved in zinc at 800°C by holding them in a tantalum enclosure attached to the bottom of an agitator. The tantalum enclosure prevents the changing configuration of the dissolving specimen from altering the mixing characteristics.

Inspection of the stainless steel specimen after one hour of contact showed that it had completely dissolved, and preliminary analytical data indicated complete dissolution in less than 10 min. These results suggest that the Sb-Cu alloy dissolves stainless steel at a much higher rate than liquid zinc with moderate agitation. This fact, coupled with the much

higher solubility of the stainless steel constituents in the Sb-Cu alloy, indicates that active consideration of the alloy for use in the process is well-merited. Further investigations will be made to identify any problems associated with corrosion, entrainment, and interfacing with other process steps.

2. General Chemistry and Chemical Engineering

    a. Sodium Chemistry

        (i) Studies of the Formation and Stabilization of Carbon-bearing Dispersions in Sodium (F. A. Cafasso)

        Last Reported: ANL-7561, p. 87 (March 1969).

        Efforts to prepare stable dispersions of elemental carbon in liquid sodium have not proven fruitful. For this and other reasons, work in this area has been discontinued.

        (ii) Determination of the Solubility of Helium in Sodium (F. A. Cafasso)

        Last Reported: ANL-7561, p. 88 (March 1969).

        Information concerning the temperature and pressure coefficients of helium solubility in liquid sodium is important to the selection of a cover gas for sodium-cooled reactors. Accordingly, the solubility of helium in liquid sodium has been measured as a function of temperature (350-550°C) and pressure (2-7 atm). The temperature-dependence study was recently completed, and the results are summarized below; the pressure-dependence experiments are still in progress.

        The experimental procedure was adapted from a method* previously used to determine the solubility of rare gases in eutectic mixtures of fused fluorides. Approximately 2.5 liters of sodium in a stainless steel vessel was saturated with ^{3}He-enriched helium gas at a preselected temperature and pressure by circulating the gas through the metal for 2 hr. The saturated metal was allowed to stand overnight at the same temperature and pressure. Approximately 2 liters of this equilibrated sodium was transferred into another stainless steel vessel, where the dissolved helium was stripped from the sodium by recirculating argon through the metal. The argon-helium mixture was then drawn by a Toepler pump through a liquid-nitrogen-cooled Molecular Sieve trap into a bulb of known volume. The helium passed unadsorbed through the trap,

---

*Grimes, W. R., Smith, N. W., and Watson, G. M., J. Phys. Chem. 62, 862 (1958).
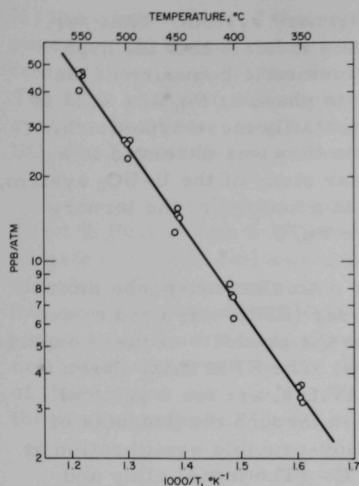
Fig. IV.D.1. Solubility of Helium in
Liquid Sodium

whereas the argon was retained. Finally, the contents of the bulb were assayed for helium isotopes and other gases with a mass spectrometer. The inclusion of ^{3}He in the saturating gas enabled a distinction to be made between soluble helium and helium introduced as a contaminant during the stripping step.

Helium solubilities were measured at approximately 50° intervals between 350 and 550°C at 6-7 atm pressure of helium. The results of four measurements at each temperature are shown graphically in Fig. IV.D.1. The data were fitted by the method of least squares to a linear equation of the form log solubility versus 1/T. The regression line can be represented by:

(350-550°C) Log He solubility (ppb/atm) = 5.11 - 2850 T^{-1}.

The error in the helium solubility at the 95% confidence level is 4%. The heat of solution calculated from this equation is 13.0 ± 0.6 kcal/mol.

b. Chemistry and Engineering

(i) Phase-diagram Study of the Ternary System U-Pu-O (P. E. Blackburn and A. E. Martin)

Last Reported: ANL-7561, pp. 88-89 (March 1969).

An attempt is being made to utilize an equilibration technique to establish the hypostoichiometric boundary of the fluorite phase in the U-Pu-O system. Liquid uranium-plutonium alloys are equilibrated with mixed-oxide crucibles at elevated temperatures. The analyses of the product crucibles should provide data on the hypostoichiometric boundary, if the study is confined to regions of the system where the desired two-phase equilibrations are possible. This is likely to include regions as high as Pu/U = 1 in the temperature range from 1600 to 2300°C; however, the first experiments are being conducted at the section where Pu/U = 0.25.

A number of problems associated with the operation of the new plutonium glovebox and its high-temperature furnaces were revealed during the initial experimentation. Most of these problems are now under reasonable control. In addition, these experiments revealed some of the problems of the equilibration technique which are inherent in its application
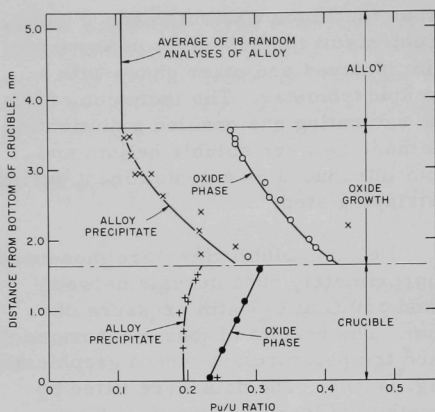
Fig. IV.D.2. Electron Probe Microanalyzer Analyses of Products (Alloy, Oxide Growth, and Crucible) of Equilibration between Liquid Uranium-Plutonium Alloy and Mixed-oxide Crucible at 2000°C

to a ternary system. Thus far, the data indicate that the hypo-stoichiometric boundary of the fluorite phase at $Pu/U = 0.25$ is substantially more hypostoichio-metric than was observed in a similar study of the $U-UO_2$ system, i.e., at a section of the ternary where $Pu/U = 0$.

An electron-probe micro-analyzer (EPM) was used to examine the products of these experiments. The EPM data, shown in Fig. IV.D.2, are for a vertical section through the products of an alloy-crucible equilibration at 2000°C. (The initial alloy and crucible had Pu/U compositions of 0.243 and 0.246, respectively. The initial and final O/M compositions of the crucible were 2.0

and 1.62, respectively.) The EPM analytical data in Fig. IV.D.2 are given in Pu/U ratios as a function of the distance from the bottom of the crucible. The existence of concentration gradients in both the oxide growth and the crucible was revealed by the data. In addition, from the data in the region of contact between the oxide growth and the alloy, it was established that at the temperature of the experiment the Pu/U ratio of the fluorite phase is 2.2 times greater than that of the liquid alloy with which it is in equilibrium. This tie-line information allows an adjustment to be made in the composition of the initial alloy for future experiments at this temperature so that the composition of the initial oxide growth will be essentially the same as that of the crucible. In this way, the establishment of a Pu/U concentration gradient in the crucible should be avoided. However, to finish the experiment with an alloy of the proper composition, it will be desirable to conduct the experiment in two stages. In the first stage, the crucible would be reduced nearly to the hypostoichiometric boundary. The alloy and oxide growth would then be removed and be replaced by fresh alloy. During the second stage, the final, but relatively minor, adjustment of the crucible composition would occur.

(ii) Vapor Species Partial Pressures in the Ternary U-Pu-O System (J. E. Battles and P. E. Blackburn)

Last Reported: ANL-7561, pp. 89-91 (March 1969).

Mass-spectrometric studies of the volatilization behavior of the uranium-plutonium-oxygen system are being made to determine

(1) the composition of the vapor phase in equilibrium with the condensed phase(s), (2) the partial pressures of the vapor species as a function of temperature, and (3) the thermodynamic properties of the vapor species. The first phase of this study, which was devoted to the plutonium-oxygen system, has been completed. The study of the volatilization behavior of UO_2-PuO_2 material was recently initiated.

Two preliminary experiments on the volatilization of 20 wt % PuO_2-80 wt % UO_2 material at ~2260°K have been conducted. A tungsten effusion cell was used in the first experiment, whereas a rhenium effusion cell was used in the second experiment. The starting material had an oxygen-to-metal (O/M) atom ratio of 2.01_3. In these experiments, vapor species of W-O (tungsten effusion cell) and Re-O (rhenium effusion cell) were observed during the initial heating of the sample. The intensity of these vapor species decreased rapidly, thus indicating a reduction in the oxygen potential (O/M) of the samples.

In the second experiment, the sample (374 mg) was heated at about 1400°C until the Re-O vapor species were no longer detectable. The sample was then heated at about 2260°K for 20.5 hr. The variation of the ion intensities as a function of time is shown in Fig. IV.D.3. At point A in Fig. IV.D.3, a temperature decrease (10-15°) occurred, and at point B, a momentary high-voltage failure occurred. The points R_1 and R_2 indicate reheats after cooling the sample to room temperature. At point R_1 (9.5 hr), a sample was removed for oxygen analysis. The analysis yielded
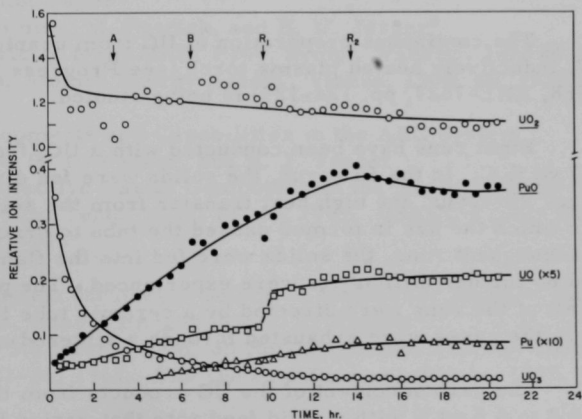

Fig. IV.D.3. Variation of the Ion Intensities of UO_2^+, UO^+, UO_3^+, PuO^+, and Pu^+ as a Function of Time at Constant Temperature (~2260°K)

an O/M atom ratio of 1.92$_0$. The remainder of the material ($\sim$53 mg) was
then reheated to 2260°K for an additional 11 hr. From point R$_1$ to the point
marking the conclusion of the experiment, the ion intensities of the vapor
species appear to have reached an approximate steady-state condition. The
residual material at the conclusion of the experiment (after 20.5 hr) had
an O/M atom ratio of 1.86$_5$. Although PuO$_2^+$ was detected in the vapor phase
in a minor amount, its concentration could not be evaluated because the
mass spectrometer does not completely differentiate between PuO$_2^+$ and
UO$_2^+$. The ion intensities of UO$_2^+$, UO$^+$, PuO$^+$, and Pu$^+$ were determined
using an ionizing-electron energy of 11 eV, whereas 15 eV was used in the
measurement of the ion intensity of UO$_3^+$.

Although considerable scatter exist in the data shown in
Fig. IV.D.3, the experiment did fulfill its purpose of establishing the rela-
tive abundance of the vapor species and the variation in the concentration
of the species as a function of time at a constant temperature.

Batches (25-g each) of 5 wt % PuO$_2$-95 wt % UO$_2$,
10 wt % PuO$_2$-90 wt % UO$_2$, and 20 wt % PuO$_2$-80 wt % UO$_2$ material using
97% ^{235}U will be prepared. This material should eliminate the difficulty
in the present experiments in resolving the UO$_2^+$ and PuO$_2^+$ peaks that
resulted from the use of ^{238}U and ^{239}Pu.

(iii) <u>Preparation of Nuclear Materials</u> (P. A. Nelson)

Last Reported: ANL-7561, p. 91 (March 1969).

The continuous preparation of UC from uranium oxides
with a 25-kW, inductively heated plasma torch (see Progress Report for
December 1968, ANL-7527, pp. 124-125) is being studied.

Eight runs have been conducted with a UO$_2$ feed material
containing 8.7 wt % C. In the first run, the solids were fed directly into
the plasma arc. However, the high heat transfer from the solids to the
quartz tube in which the arc is formed caused the tube to crack. Therefore,
in the seven subsequent runs, the solids were fed into the flame downstream
of the arc and no further difficulties were experienced. The product powder
and gases in all of the runs were directed by a ceramic tube into the product
receiver where the gases were exhausted through a sintered metal filter.

The carbon content of the UC products from the seven runs
varied from 5.0 to 6.5 wt % with a solid feed rate that varied from 10 to
15 g/min and plate power that ranged from 15.0 to 16.8 kVA (power to the
plasma is estimated to be 40-50% of the plate power). The results of these
runs are being analyzed to determine the effects of all the variables. Sub-
sequent runs will be conducted when complete analytical results are available
for the product material.

PUBLICATIONS

Foreseeable Application of ^{252}Cf to Neutron Radiography
    J. P. Barton
        Californium-252, Proc. Am. Nucl. Soc. Symp., New York,
        October 22, 1968. USAEC Report CONF-681032, pp. 303-319

Television Systems for Nondestructive Testing
    Harold Berger
        Proc. 5th Intern. Conf. on Nondestructive Testing, Montreal,
        May 21-26, 1967. The Queen's Printer, Ottawa, 1969, pp. 118-124

Ultrasonic Imaging Systems for Nondestructive Testing
    Harold Berger
        J. Acoust. Soc. Am. $\underline{45}$(4), 859-867 (April 1969)

Argonne Code Center: Compilation of Program Abstracts
    M. K. Butler, Marianne Legan, and L. Ranzini
        ANL-7411 Supplement 2 (April 1969)

Fast-Neutron Effects on Type-304 Stainless Steel
    R. Carlander, S. D. Harkness, and F. L. Yaggee
        Nucl. Appl. $\underline{7}$(1), 67-75 (July 1969)

Condensing Injector Experiments and Analysis of Performance with
Supersonic Inlet Vapor
    M. A. Grolmes, M. Petrick, and E. W. Jerger*
        Electricity form MHD, Proc. Symp., Warsaw, July 24-30, 1968.
        Intern. Atomic Energy Agency, Vienna, 1968, pp. 1521-1544

Recent Developments and Capabilities in the ARC System
    L. C. Just, P. L. Walker, and B. J. Toppel
        The Effective Use of Computers in the Nuclear Industry, Proc. Conf.,
        Knoxville, Tenn., April 21-23, 1969. USAEC Report CONF-690401,
        pp. 337-343

A Thermoluminescent Image-Detection Method for Neutron Radiography
    J. Kastner, Harold Berger, and I. R. Kraska
        Proc. 5th Intern. Conf. on Nondestructive Testing, Montreal,
        May 21-26, 1967. The Queen's Printer, Ottawa, 1969, pp. 132-134

Cadmium-Neptunium--A Partial Phase Diagram of the System
    M. Krumpelt, I. Johnson, and J. J. Heiberger
        J. Less-Common Metals $\underline{18}$(1), 35-40 (May 1969)

---

*University of Notre Dame.

The Influence of Precipitates on the Formation of Helium Bubbles in Irradiated Copper-Boron Alloys
S. R. Pati and P. Barrand
J. Nucl. Mater. 31, 117-120 (1969)

Analtyical and Experimental Studies of Liquid-Metal Faraday Generators
M. Petrick and J. J. Roberts
Electricity from MHD, Proc. Symp., Warsaw, July 24-30, 1968. Intern. Atomic Energy Agency, Vienna, 1968, pp. 1501-1520

The Application of Pulsed-Electromagnetic Field Methods to Liquid-Metal Fast Reactor Nondestructive Test Problems
C. J. Renken
Bull. Inform. Sci. Tech. (Paris) 136, 15-26 (April 1969)

The following appeared as abstracts in Trans. Am. Nucl. Soc. 12(1) (June 1969):

Void Formation in Fast-Neutron Irradiated Type-304 Stainless Steel
S. D. Harkness, D. G. Letzring, and C. Y. Li
p. 115

Numerical Comparison of Data Processing Codes for Fast Reactors
W. W. Little,* R. W. Hardie,* R. E. Schenter,* E. M. Pennington, B. Hutchins,** and L. N. Price**
p. 144

Swelling Behavior of Vibratorily-Compacted Mixed Carbides
L. C. Michels and L. A. Neimark
pp. 88-89

The Ratio $\sigma\gamma(^{238}U)/\sigma_f(^{235}U)$ in the Neutron Energy Range 30 to 900 keV
W. P. Poenitz
p. 279

Some Considerations of Radiation-Enhanced Creep
J. A. Tesk and C. Y. Li
p. 133

---

*Battelle Northwest Laboratory.
**General Electric Co., Sunnyvale.

V. NUCLEAR SAFETY

A. Reactor Kinetics

1. Accident Analysis and Safety Evaluation (G. J. Fischer)

Last Reported: ANL-7577, p. 181 (April-May 1969).

a. Special Systems Analysis

Preliminary analyses of proposed experiments on failures of fast fuel pins with the Mark-II TREAT loop have been performed with the help of the SAS1A code. The fuel pin considered here is a 12-in.-long stack of 13% enriched UO_2 pellets of 0.246-in. outer diameter, contained inside a Type 304 stainless steel jacket of 0.290-in. outer diameter with a clearance of 2 mils filled with helium gas at atmospheric pressure. The fuel pin (93% theoretical density) is surrounded by a ring of six hollow dummy pins separated by 0.056-in.-diameter, spiral spacer wire. All seven pins are placed in the test region of the Mark-II loop in which liquid sodium at 450°C is circulated at the rate of 4 m/sec. The loop is then exposed to two different power transients in TREAT reactor. These transients, shown in Fig. V.A.1, are equivalent to a total energy production of 1760 and 2070 J/g UO_2, respectively.
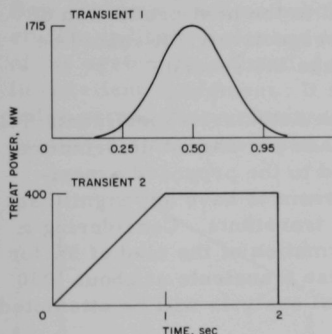

Fig. V.A.1. Power Shapes for Two TREAT Transients

SAS1A is used to calculate the temperature and stress profiles as a function of the energy produced in the pin, assuming an equivalent single fuel-pin geometry. The clad rupture, thought to be due to the excessive loading on the clad, is predicted based on the permanent deformation. The chain of events leading to the permanent deformation of the cladding consists of filling the clearance between the fuel and the cladding due to thermal expansion of UO_2, and the elastic deformation of the clad, primarily due to the thermal expansion of the fuel (including ~10% volume change due to the melting of UO_2) until the loading exceeds the yield point, when clad undergoes plastic deformation. The percentage plastic deformation is defined as

$$\text{Percentage Plastic Deformation} = \frac{r_c(t) - r_c(t_0)}{r_c(t_0)} \times 100,$$

where $r_c(t)$ is the outer radius of the clad at any time t. Time t_0 is taken to be the time when loading exceeds the yield point. The plastic flow
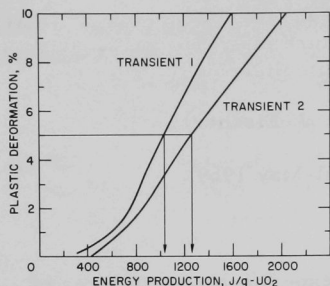
Fig. V.A.2. Percentage Plastic Deformation of Cladding as a Function of the Energy Production in a Test Pin for the Transients of Fig. V.A.1

depends explicitly on the rate and the magnitude of the transient; we show in Fig. V.A.2 a plot of this quantity as a function of the energy production in the test pin for both power transients.

A sharp increase in the permanent deformation observed at the energy production of about 750 J/g UO_2 is attributed to the onset of the melting of the fuel near the centerline. Additional melting of UO_2 during the remaining of the power transient causes more plastic deformation, although the rate of deformation is somewhat slower. The plastic deformation of the clad depends not only on the magnitude but also on the rate of loading. This point is illustrated in Fig. V.A.2, where a 5% plastic deformation is found to correspond to the heat production of 1030 and 1260 J/g UO_2 for transients 1 and 2, respectively. It should be remembered that the first transient is faster than the second.

From some previous analyses of the autoclave experiments S-2 and S-3 it appears that the cladding ruptures when permanent deformation exceeds 4%. This result can be usefully applied to the proposed experiments as well, since the coolant flow does not seem to have any significant influence on the pin performance for these fast transients. Considering a somewhat optimistic value for the plastic deformation of the clad of 5% for failure, the clad is expected to rupture for these transients at about 1030 and 1260 J/g UO_2, respectively. A more critical analysis will be attempted.

2. Reactor Control and Stability

a. Reactor Stability and Stability Design Criteria for Spatially Dependent Systems (L. Habegger and C. Hsu)

Last Reported: ANL-7577, p. 182 (April-May 1969).

(i) Nonlinear Model. Investigations of the quasilinearization iterative procedure for obtaining solutions to nonlinear, one-dimensional, steady-state reactor equations are continuing. This numerical procedure has proven to be effective in computing solutions to nonlinear equations of the form

$$\frac{\partial}{\partial x} D(x) \frac{\partial}{\partial x} \phi(x) + \alpha A(x)\phi(x) + B(x)\phi(x) + a_1(x)\delta T_c(x)\phi(x) = 0;$$

$$\frac{\partial \delta T_c(x)}{\partial x} = c(x)\phi(x); \quad \phi(0) = \phi(\ell) = 0; \quad \delta T_c(0) = 0; \quad \delta T_c(\ell) = \Delta T_c.$$

These equations are a model of a reactor system with coolant-temperature feedback; the critical flux and coolant temperature distribution, $\phi(x)$ and $\delta T_c(x)$, and the parameter α are determined simultaneously.

Extension of the computational procedure to a diffusion equation containing control-rod simulation, fuel-temperature feedback, and coolant-temperature feedback is being investigated.

3. Coolant Dynamics

a. Critical Flow (H. K. Fauske and M. A. Grolmes)

Last Reported: ANL-7577, p. 183 (April-May 1969).

(i) Sonic Velocity and Pressure-wave Propagation. The determination of the propagation velocity of pressure pulses in both one- and two-component, two-phase media has been studied over a wide range of flow regimes, such as bubble, slug, annular and droplet flows.* These studies indicate a marked change in the characteristic propagation velocity of the system as a function of flow regime. Experiment and analysis are in excellent agreement. It is suggested that measurement of the pressure-pulse propagation velocity in known flow regimes can be employed to identify a given two-phase flow regime. Figure V.A.3 shows the characteristic propagation velocity as a function of flow regime and void fraction with approximate flow-regime bounds indicated. The large difference in propagation velocity with flow regime is apparent and suggests that only modest experimental accuracy is required to identify regions of discrete flow regimes.
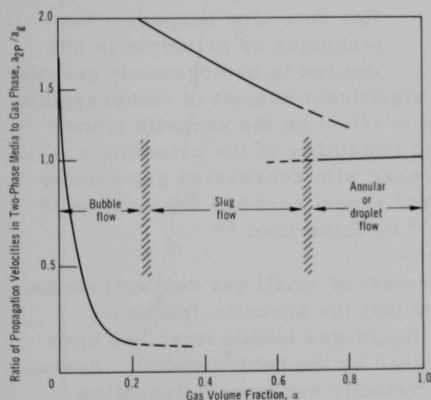
It is important in the LMFBR safety program to detect the presence of minute quantities of inert gas in the sodium coolant. This information is important in regard to (1) the problem of superheat and (2) the early detection of fuel-pin failure. Whether the incipient superheat of the sodium should be considered as a wall-cavity nucleation-site problem depends

Fig. V.A.3. Characteristic Pressure-pulse Propagation Velocity in Various Two-phase Flow Regimes as a Function of Volume Fraction

---

*Henry, R. E., Grolmes, M. A., and Fauske, H. K., Propagation Velocity of Pressure Waves in Gas-Liquid Mixtures, Proc. Int. Symp. on Research in Co-current Gas-Liquid Flow, University of Waterloo, Ontario, Canada (September 18-19, 1968); Grolmes, M. A., and Fauske, H. K., Propagation Characteristics of Compression and Rarefaction Pressure Pulses in One-component Vapor-Liquid Mixtures, submitted for publication to J. Nuclear Science and Engineering.

on the presence or absence of inert-gas bubbles in the coolant. Much research in pool-boiling systems, where gas bubbles are not believed to be present in the bulk of the sodium, indicates large incipient superheats. However, some designers* believe that such experiments are not applicable to reactors, in which inert-gas bubbles are likely to be present. To resolve this question, a technique is needed that is sensitive to very small concentrations of gas in the coolant.

Gas in the system is likely to be distributed in the form of bubbles or regions of small bubble clusters. For a homogeneous distribution of argon gas in a sodium liquid at 1600°F and 1 atm, Fig. V.A.4
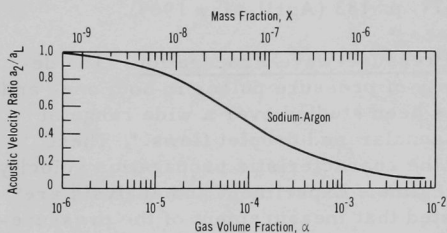

Fig. V.A.4. Propagation Velocity in a Homogeneous Two-phase Sodium-Argon System at 1600°F and 14.7 psia as a Function of Mass or Volume Fraction

shows the ratio of the propagation velocity in the two-phase mixture to that in pure sodium as a function of gas concentration. In principle, this ratio is very sensitive to extremely low gas concentrations. A technique based on this principle could conceivably be used to determine the first appearance of trace amounts of gas in a liquid system or to monitor continuously the level of gas entrainment. For detection purposes, the technique or principle is not limited to homogeneous gas distribution, because the presence of any significant amount of compressible gas in a channel would have a measurable effect on the acoustic transit time for the channel. The accuracy and reliability of the principle are believed to be good and, in fact, to increase with decreasing gas concentration. Agreement between analysis and experiment has been shown to be excellent to void fractions of 5×10^{-4} by Silberman.**

Related to the measurement of small gas concentrations, Silberman and Walle et al.† have shown that the acoustic-frequency response characteristics of two-phase liquid-gas bubble mixtures have resonance peaks at frequencies determined by the bubble radius. Again, in principle, analysis of the acoustical velocity and wave-attenuation characteristics of a bubble mixture as a function of wave frequency can lead to a determination of bubble size. This is indicated as a potential

---

*Schmidt, D., "Sodium Boiling in Fast Reactors--A Review with Reference to the ISPRA Conference, October 1968," Proc. Conf. Sodium Technology and Large Fast Reactor Design, ANL-7520.

**Silberman, E., "Sound Velocity and Attenuation in Bubbly Mixtures Measured in Standing Wave Tubes," J. Acoust. Soc. Am. 29, 925-933 (Aug 1957).
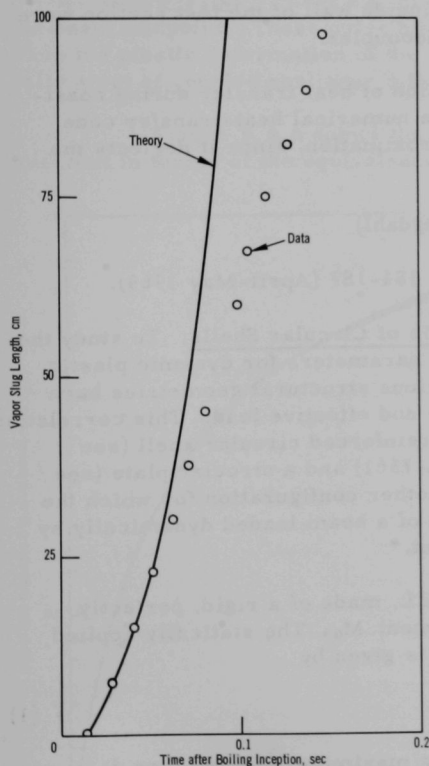
†Walle, F., Verheugen, A. J., Haagh, V. J. M., and Bogaardt, M., A Study of the Application of Acoustical Methods for Determining Void Fractions in Boiling Water Systems, Proc. of Symp. on Dynamics of Two-phase Flow, Univ. Eindhoven, The Netherlands, September 4-8, 1967.

benefit to development of acoustical techniques; however, system background noise might interfere with meaningful frequency analysis. Even so, the techniques involved in flow-regime detection and gas-concentration measurement do not appear to be hindered by background noise. A single pulse of amplitude larger than background noise or a single frequency outside the range of system noise, or both, could be used.

b. **Coolant Dynamics** (R. M. Singer and R. E. Holtz)

Last Reported: ANL-7577, pp. 183-184 (April-May 1969).

(i) **Coolant-expulsion Experiments.** The test section used with the initial sodium expulsion tests is being replaced with a new, more fully instrumented section. During this downtime, the preliminary data are being reduced and analyzed. The measurements have indicated that the flow regime during the initial expulsion for incipient superheats greater than about 10°C is that of a single vapor bubble expanding against the liquid column. Thus, the data are being compared with a single-slug-type expulsion model, based on the acceleration of a liquid mass by a constant pressure difference arising from the initial superheat. As shown in Fig. V.A.5, the results for one run agree surprisingly well with theory, especially at small times. This indicates that the rate of vaporization, and thus the rate of expulsion, is controlled by the inertia of the liquid column.

Earlier data with water and methanol are being compared with this new sodium data to determine similarities in the phenomena. In the future, this experimental data will be compared to the more sophisticated models of ejection that have been or are being developed.

Fig. V.A.5. Data for Sodium Initial Expulsion from 94-cm-high Sodium Column, with 65.3-W/cm² Wall Heat Flux, 169°C Incipient Liquid Superheat, and 855°C Saturation Temperature

(ii) **Transient Experiments.** Tests of an oscillating plugging meter for use in measuring the dissolved-oxide content in sodium in the transient test loop is continuing. The

principle of operation has been reconfirmed. After the tests of the meter are completed, the system will be installed in the main loop. A modified-design cold trap is being fabricated.

   c.   Convective Instability (R. M. Singer)

      Last Reported: ANL-7548, p. 119 (Jan 1969).

      (i)   Flow-coastdown Experiment. Assembly of the test loop has begun; completion of the 1-in. NaK loop awaits delivery of several components, including the test section. In the meantime peripheral equipment is being designed and constructed, including the argon cover-gas system, some of the instrumentation, and the power supplies. Difficulties with the 20-mil thermocouples on the inside wall of the test section were resolved by switching to 40-mil thermocouples.

      An analytical description of heat transfer during coast-down is being pursued with the use of a numerical heat-transfer code. This will give a "first" numerical approximation, since it neglects the effects of free convection.

4.   Core Structural Safety (C. K. Youngdahl)

      Last Reported: ANL-7577, pp. 184-187 (April-May 1969).

      a.   Dynamic Plasticity Analysis of Circular Shells. To study the generality of the proposed equivalence parameters for dynamic plastic deformation, existing solutions for various structural geometries have been reformulated in terms of impulse and effective load. This correlation has been shown to be successful for a reinforced circular shell (see Progress Report for March 1969, ANL-7561) and a circular plate (see ANL-7577) under dynamic loading. Another configuration for which the correlation has been tested is the case of a beam loaded dynamically by a concentrated force $F(t)$ at its midpoint.*

      Consider a beam of length $2L$, made of a rigid, perfectly plastic material and having a yield moment M_0. The statically applied force F_s required to produce yielding is given by

$$F_s = 4M_0/L. \tag{1}$$

Let the dynamic load $F(t)$ increase to a maximum F_M and then decrease monotonically to zero. If $F_s \leq F_M \leq 5.722\, F_s$, a plastic hinge forms at the center of the beam and the resultant final deformation u_f there can be solved in closed form. In terms of the equivalence parameters, this solution is

---

*Symonds, P. S., Dynamic Load Characteristics in Plastic Bending of Beams, J. Appl. Mech. 20, 475-481 (1953).

$$u_f = \frac{3I^2}{2\gamma LF_s} \left[1 - \frac{F_s}{F_e}\right], \tag{2}$$

where γ is the mass per unit length, and I and F_e are the impulse and effective force, defined by

$$I = \int_{t_y}^{t_f} F(t) \, dt; \qquad F_e = I^2/2 \int_{t_y}^{t_f} F(t) \, dt. \tag{3}$$

Consequently, for the given load range the proposed correlation is exact.

For $F_M > 5.722 \, F_s$, additional plastic hinges appear when $t = t_h$, where $F(t_h) = 5.722 \, F_s$, at the locations $\pm 0.404 \, L$, measured from the beam midpoint. These outer hinges move as the loading progresses. Then the plastic deformation of the beam must be found by solving numerically a set of coupled nonlinear differential equations.

Figure V.A.6 shows the final plastic deformation of the beam midpoint in terms of the equivalence parameters for various families of
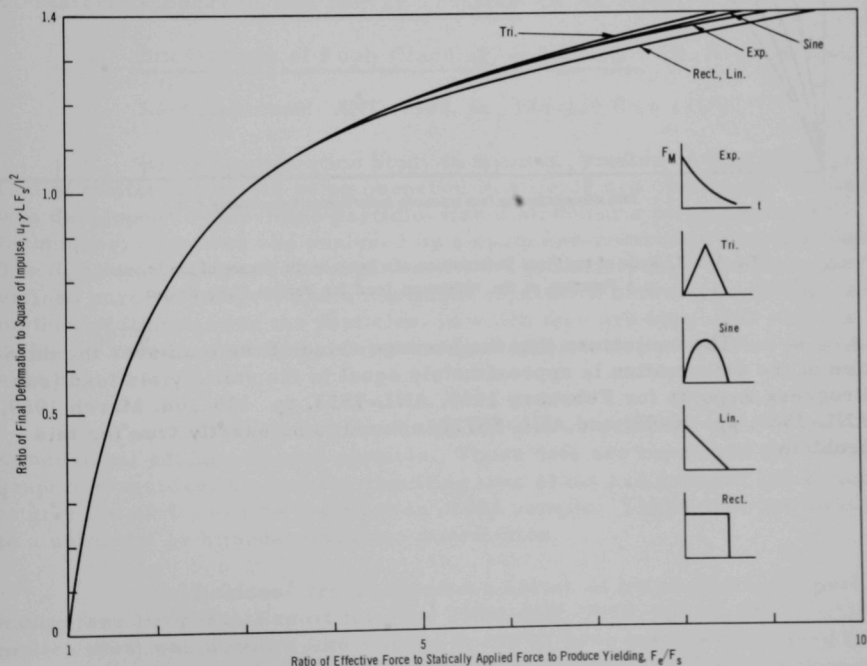

Fig. V.A.6. Ratio of the Final Deformation of a Beam to the Square of the Impulse as a Function of the Effective Load for Various Pulse Shapes

load-time history. For comparison, the same results are plotted in Fig. V.A.7, with the maximum force replacing the effective force as a parameter. It is apparent that the impulse and effective load provide an excellent means of correlating results for widely differing load functions.

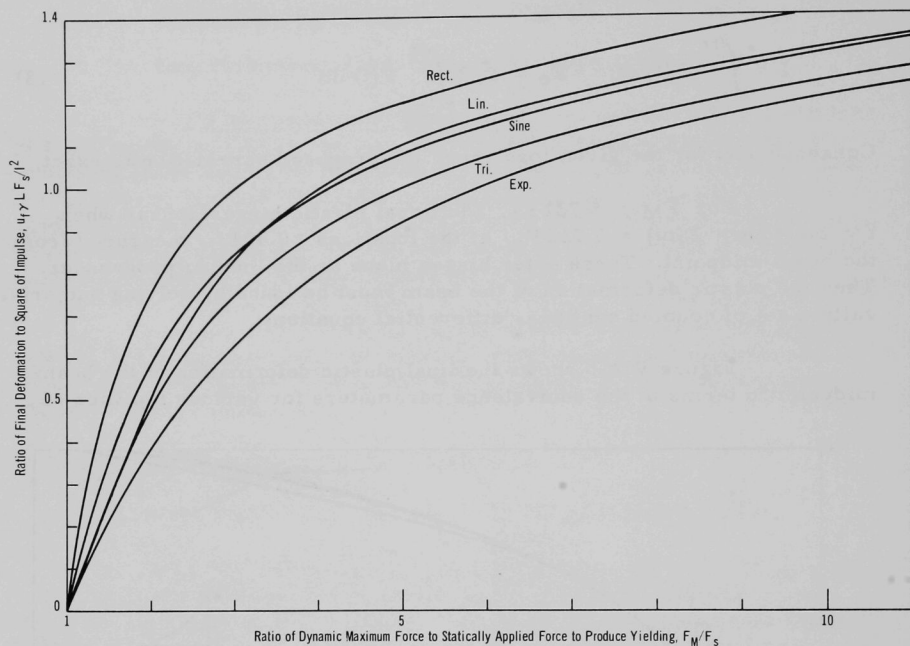Fig. V.A.7. Ratio of the Final Deformation of a Beam to the Square of the Impulse as a Function of the Maximum Load for Various Pulse Shapes

The conjecture that the average value of the load over the duration of the deformation is approximately equal to the static yield load (see Progress Reports for February 1969, ANL-7553, pp. 106-108; March 1969, ANL-7561, pp. 96-98; and ANL-7577) is found to be exactly true for this problem.

5. Fuel Meltdown Studies with TREAT

a. Development of Experimental Methods (C. E. Dickerman)

Last Reported: ANL-7561, pp. 97-99 (March 1969).

Preparations were made for checkout experiments with the Mark-II integral sodium loop in TREAT. The specifications for this experiment include sodium flow through the test section at 4 m/sec, and a total energy input to the samples of approximately 1.77×10^3 J/g. The loop was carried through its startup operation and shutdown sequence as a final check of the loop-operating manual, and the manual was put into final form for transmittal to Idaho. The loop and its auxiliary equipment were packaged and shipped from the Illinois Site on June 19. Included in the shipment were a control and instrumentation console rack assembly, the silicone cooling oil module, and the electrical power unit. The apparatus was assembled in Idaho, checked out, and the loop was run successfully with sodium flow on June 25. Reactor loading and instrumentation hookup preparations are underway.

6. Materials Behavior and Energy Transfer (R. O. Ivins)

a. Interactions of Fuel, Cladding, and Coolant (D. R. Armstrong)

Last Reported: ANL-7548, pp. 128-129 (Jan 1969).

(i) Fragmentation Study in Sodium. Studies of the fragmentation of molten materials being quenched in a liquid are continuing. A method was developed to determine particle-size distributions by photographic techniques; negatives are analyzed by a computer-controlled film digitizer. The digitizer requires film negatives with a uniformly high contrast, sharply defined particle images, and a minimum separation between particles. A method of illuminating the particles, in which they are supported above a diffusion screen, provided sufficient edge definition for production of suitable negatives.

The output from the film digitizer provides the two-dimensional surface of each particle. These data are corrected for photographic magnification, and the resulting true areas are grouped and summed to give the particle-size distribution of the sample. These data can be fitted to a unimodal or bimodal Gaussian distribution.

Residues from a previous series of fragmentation experiments (see Progress Report for June 1966, ANL-7230, pp. 69-70), in which molten steel was dropped into sodium at 250°C, have been re-examined by screening techniques because the method that had been used to calculate the

particle-size distribution was in error. In the experiments, drops of molten steel at 1600-2400°C were dropped from a height of 2 ft into molten sodium. Because of the violence of the interaction and fragmentation, some of the steel and sodium was ejected from the crucible. Therefore, because of the incomplete samples, detailed particle-size analysis was not possible, so the mean diameter of the fragments was calculated using the volume-surface mean particle size, d_{vs}, which is defined by the following equation, assuming all particles to be spherical and of a size midway in a particular sieve range:

$$d_{vs} = \frac{\Sigma f_i d_i^3}{\Sigma f_i d_i^2},$$

where f_i is weight fraction of particles in group i, and d_i is mean particle diameter in group i. (Note: In ANL-7230, the Sauter mean diameter was incorrectly defined, so the mean diameters reported were wrong. Correct values are given here.)

Table V.A.1 illustrates that the diameter of the fragments, d_{vs}, decreases as the temperature of the molten-steel drop is increased above 1600°C.

TABLE V.A.1. Mean Diameter of Fragments
Resulting from Dropping Molten Stainless
Steel into Sodium at 250°C

Sodium Temp (°C)	Sample-drop Temp (°C)	Volume-Surface Mean Diameter (mm)
250	1600	1.26
250	1800	0.67
250	2150	0.43
250	2250	0.27
250	2400	0.45

Similarly, the data from experiments in which the temperature of the molten sodium was increased while the temperature of the molten steel was held constant at 2200°C were re-evaluated. The results in Table V.A.2 indicate that the mean particle size of the fragments decreases as the temperature of the sodium is increased from 250 to 820°C.

TABLE V.A.2. Mean Diameter of Fragments
Resulting from Dropping ~2200°C Stainless
Steel into Sodium

Sodium Temp (°C)	Sample-drop Temp (°C)	Volume-Surface Mean Diameter (mm)
250	2250	0.27
720	2200	0.23
800	2200	0.26
820	2300	0.19

b. High Temperature Physical Properties (M. G. Chasanov)

Last Reported: ANL-7561, pp. 99-100 (March 1969).

(i) Total Pressure over Liquid UO_2. An important input
parameter for equation-of-state calculations for reactor fuels is vapor
pressure of the fuel. Presently available data must be extrapolated over
many orders of magnitude to obtain vapor-pressure values at the tempera-
tures of interest in reactor-safety calculations. Consequently, a program
has been initiated to measure vapor pressures over liquid reactor fuels by
means of transpiration techniques so as to reduce the extent of the extrapo-
lation. The data to be obtained will allow the calculations to be made with
greater confidence.

The first material to be studied will be uranium dioxide.
The transpiration technique has previously been successfully applied to
vapor pressure measurements with uranium dioxide up to about 2600°C.[*]
In the experiments planned in this study, it is expected that measurements
will be made up to about 3250°C. The transpiration equipment will be oper-
ated in an induction furnace with suitable radiation shielding included to
insure temperature uniformity.

To date, vapor pressure measurements have been performed
for testing purposes at about 2350°C. Satisfactory agreement has been found
with literature values.[*,**] Further tests of reproducibility and of several
experimental parameters are planned before proceeding to higher
temperatures.

---

[*]Alexander, C. A., Ogden, J. S., and Cunningham, G. W., Thermal Stability of Zirconia- and Thoria-Base Fuels, BMI-1789 (Jan. 6, 1967).
[**]Tetenbaum, M., and Hunt, P. D., Transpiration Studies of the Total Vapor Pressure of Uranium-bearing Species over Urania, in Chem. Eng. Div. Semiannual Report, January-June 1965, ANL-7055, p. 165 (Oct 1965).

7. Fast Reactor Safety Test Facility Study (C. N. Kelber)

Last Reported: ANL-7577, pp. 196-197 (April-May 1969).

   a. Program Definition and Justification

   The preliminary (Phase I) draft of the report on Program Definition and Justification was distributed to industrial contractors, RDT (with copies for transmission to regulatory groups), and cognizant individuals at ANL and other AEC laboratories. Recipients of the report were asked to make a critical review and return their comments, which will be utilized in preparing a revised (Phase II) draft.

   A preliminary judgement on the probable need for "whole subassembly" (STF-type) experiments and "whole core" (ETF-type) experiments is being formulated and documented.

   b. Facility Definition and Utilization

   (i) Loop Capabilities. Predicting the response of in-pile loops to potential molten fuel-sodium interactions requires knowledge of an equation of state for sodium covering both liquid and gaseous phases.

   Work on the use of the Himpan equation of state for sodium (see Progress Report for March 1969, ANL-7561, p. 104) has continued. The Himpan equation was printed incorrectly in ANL-7561: its correct form is

$$\left[P + \frac{a}{(V - b)(TV - c)} \right] (V - d) = RT.$$

   The most accurate way of calculating material properties is to use a purely empirical correlation of experimental data. Such correlations have two disadvantages, however. They do not necessarily give a reliable basis for extrapolation beyond the region where experimental data are available, and they may not be thermodynamically consistent. For these reasons it is convenient to use an equation of state which can easily be checked for thermodynamic consistency, and which, as its form is based on theoretical considerations, should be a reasonable basis for extrapolation. But it is obviously desirable that such an equation should predict reasonably well the properties for which we have experimental data.

   A study of the predictions of the Himpan equation with the adjustable constants chosen to fit a critical-point estimate of $T_c = 2733°K$, $P_c = 408.2$ atm, $V_c = 5.501$ cm^3/g, as described in ANL-7561, has been completed. The vapor properties are predicted well, but the agreement for

the liquid properties, especially differential properties such as the thermal expansion coefficient and the velocity of sound, is poor. As pointed out in ANL-7561, such properties are important in a vapor explosion.

This result is not unexpected, as the constants were not chosen to give close agreement in the liquid region. At present work is continuing to see whether better agreement can be obtained by fitting the constants to a wide range of liquid densities, for example, rather than to a critical-point estimate. It is planned to test such a method by using it for a similar material, such as cesium, for which experimental data closer to the critical point are available.

It may be, however, that it is not possible to predict these highly sensitive differential properties from an equation of state. In this case we shall have to use the purely empirical type of formula and accept the possibility that our calculations may violate the laws of thermodynamics, in hope that such violations are small.

The objectives of this work are:

1. Give as accurate an estimate as currently is readily available of the safety problems and loop pressure suppression needs associated with in-pile LMFBR safety tests using a large number of fuel elements.

2. Estimate the degree of conservatism in current loop safety analysis and hence estimate the possible improvements possible in facility utilization as more knowledge of molten fuel-sodium interactions is obtained.

(ii) Neutronic Needs. Use of the ARC system for one-dimensional survey calculations has become routine. Use of the two-dimensional diffusion-theory path (for estimating feedback from the test region to the driver core) has run into a snag; convergence is exceedingly slow. Work is being carried out to determine the source of the difficulty. If necessary, the cross-section set will be revised to permit use of an option in the two-dimensional diffusion module that past experience has shown to be very fast. Current surveys are aimed at determining the neutronic needs for tests involving large numbers (greater than 37) of LMFBR fuel elements. (Detailed surveys for tests involving fewer pins have been performed in conjunction with programs such as Fuel Element Failure Propagation, and investigation at TREAT and PBF.) These considerations limit the parameter range as follows:

1. To accommodate tests well above the boiling point of the test element, the driver fuel either has to be able to withstand a large ΔT (center to surface) or must have high heat removal capacity per unit volume.

2. In medium fast transients it will be necessary to allow boiling in the test zone well before the coolant in the driver starts to boil. Thus the driver fuel has to have a low heat conductivity. Such a fuel is an oxide fuel, although insulating sleeves, as in the PBF fuel, may also be effective.

3. In a superprompt critical test, a prompt shutdown coefficient is required. In concept one may consider a system with preaccelerated, fast-acting rods to shut the reactor down following a planned reactivity insertion. Such a system is in use in SNEAK. If the insertion is the result of a meltdown following, for example, the simulation of a loss of flow with delayed scram, the time of the insertion will probably be uncertain by a large enough margin that a prompt shutdown coefficient in the driver will be required to clip the burst. Fast-acting rod systems could not detect, accelerate, and insert fast enough.

The prompt shutdown coefficient should not be too large, however, or the burst will be prematurely terminated. It may well be that the shutdown capacity limits the test size. Survey calculations indicate that the most pessimistic estimate of insertion from meltdown of a normally enriched test element is of the order of a few dollars. If the element and the driver are fully enriched, very large insertions ($\sim 25\% \ \Delta k/k$) are potentially available. Of course, the prompt shutdown need not completely compensate for the reactivity. It need only prolong the period to a manageable size.

Thus it may be necessary to "boot strap" the larger experiments by running progressively larger tests to get better estimates of the maximum reactivity insertion. Also, it may be useful to vary the Doppler coefficient in order to get the right burst peak and width. One way to do this may be by using BeO inserts which may be replaced by inert (e.g., ZrO_2) inserts when a reduction in Doppler coefficient is required.

4. Although the fission cross section suffers, it will probably be desirable to avoid the use of plutonium in the driver; nevertheless, the possibility of Doppler feedback from ^{240}Pu and ^{242}Pu should be considered.

5. Finally, to keep the driver small and have the total power within range, the power should be flattened. This requires zoning with, perhaps, BeO inserts in the nickel reflector.

It is thus concluded that the driver should have a UO_2 (possibly UC with insulating sleeve) core with some BeO both to soften the spectrum and to increase the Doppler coefficient.

In order to get the right figure of merit (power density in test to power density in the driver) it will be necessary to enrich the test zone and minimize enrichments in the driver. Enriching the test zone is limited by:

   a.   the need to test irradiated fuel,

   b.   the increased feedback from the enriched test zone, and

   c.   the changed heat transfer characteristics of high enriched fuel.

(iii) Preliminary Study of Potential Utilization of Existing Facilities. Visits have been made to PBF and SEFOR to gather detailed information needed for completing the preliminary survey. Another visit to each of these facilities is anticipated before completing this phase of the work.

Other facilities are included in the survey: TREAT is an ANL facility and informal discussions have been held with cognizant ANL personnel; after the Mark-II loop is checked out and TREAT personnel are available for consultation, formal study of TREAT capabilities will be initiated. Other facilities to be included in the survey include EBR-II, FFTF, ETR, and ATR. The survey made by the Fuel Element Failure Propagation study will be our point of departure.

B. TREAT Operations

1. Reactor Operations (J. F. Boland)

Last Reported: ANL-7577, pp. 197-198 (April-May 1969).

A partially bonded EBR-II fuel element was subjected to a constant-power transient designed to simulate the fission rate in EBR-II at a power level of 75 MW. The element was contained in a Mark-I sodium loop. Data from this test will be compared with data previously obtained from a similar test on an unbonded EBR-II element (see Progress Report for June 1968, ANL-7460, p. 119).

A Zircaloy-clad pelleted UO_2 sample with flux-depressing spacers in the top and bottom ends of the cladding was subjected to steady-state irradiation to determine if the spacers would reduce heating in the end pellets below that of the center pellets. During previous metal-water-reaction tests, cladding failure at the ends of the rods was caused by high temperature in the end pellets.

A calibration experiment was run on the experimental capsule to be used for TREAT experiments on prototype FTR fuel. The capsule was returned to PNL for disassembly and radiochemical determination of the number of fissions in the fuel samples.

Neutron radiographs were made of six groups of capsules from EBR-II, the partially bonded EBR-II element in a Mark-I sodium loop, and an oxide pin in a Mark-II sodium loop.

2. Development of Automatic Power Level Control System (J. F. Boland)

Last Reported: ANL-7577, p. 198 (April-May 1969).

A contract was awarded to the Progress Electronics Co. of Oregon Inc. for the stored-program digital-controller system to program the hydraulic control-rod-drive system. Delivery of the system is scheduled for September 1969.

C. Chemical Reaction--Chemical and Associated Energy Problems (Thermal)

1. Pressure Generation due to Particle-Water Energy Transfer

a. Steam Explosion Experiments

Last Reported: ANL-7577, pp. 200-201 (April-May 1969).

Small-scale experiments of water injection into molten materials are continuing. A high-speed photographic test was conducted with molten sodium chloride in a transparent quartz tube to observe the course of the steam-explosion phenomena. For the first time, this test enabled detailed observation of the behavior of the injected water in the molten material until the explosion occurred.

A 100-g sample of sodium chloride was melted by torch heating in a rectangular quartz tube ($1\frac{1}{4}$ in. by $1\frac{9}{16}$ in. and $\frac{1}{16}$ in. wall). When the molten sodium chloride reached about 900°C, 3 cm^3 of water at room temperature was forcibly injected into the melt, and a high-speed motion-picture camera photographed the subsequent events.

Water injection resulted in a violent explosion, a loud noise, and the quartz tube was completely disintegrated and displaced from the original location. Figure V.C.1 shows selected frames from the motion picture. Before the explosion, the sequence of significant events was: (a) when the water was injected into the molten mass, it was immediately surrounded by a cloud of water vapor, which spread through the molten mass
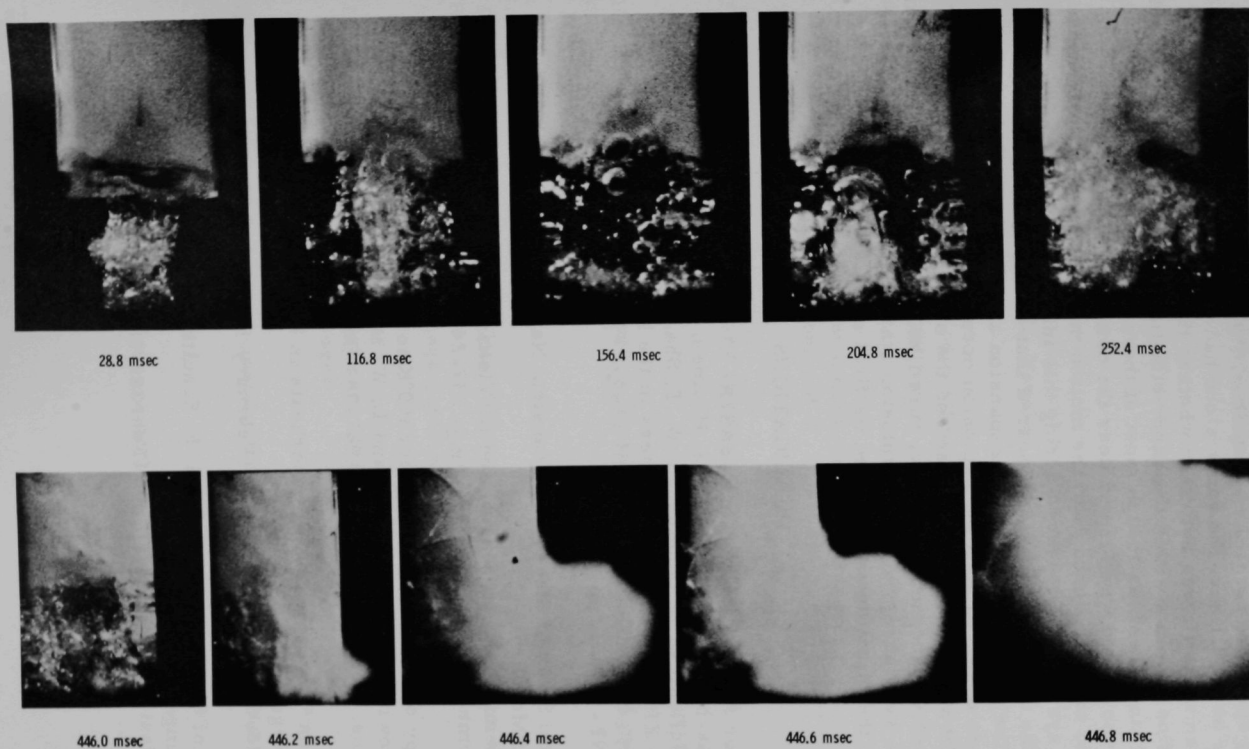
Fig. V.C.1. Events after 3 ml of Room-temperature Water were Injected into Molten Sodium Chloride at 900°C (at various times from start of injection)

with small, sporadic, burstlike expansions, (b) when the injection was completed after about 0.1 sec, the vapor cloud had penetrated about two-thirds of the molten mass (it was not clear whether the water as liquid was dispersed as fine droplets within the vapor cloud), (c) the molten mass became relatively transparent, as though most of the vapor cloud had disappeared, (d) a new vapor cloud was formed near the bottom of the quartz tube, and (e) the cloud expanded throughout the molten mass. No appreciable expansion of the system was observed during this interval, except for slight bulging of the upper surface. It appeared that the injected water was entrapped in the molten mass and its expansion arrested. No significant changes were observed until the explosion occurred. During the interval of about 0.19 sec between 252.4 msec and the start of the explosion sequence at 446.0 msec, only sporadic, burstlike, expansions and small-scale turbulences were observed. The explosion started at about 0.45 sec after the start of the injection and reached its final stage about 0.6 msec later.

PUBLICATIONS

Fast Reactor Accident Study Code, SAS1A
    G. J. Fischer, J. C. Carter, T. J. Heames, D. R. MacFarlane,
    N. A. McNeal, C. K. Sanathanan, W. T. Sha, and C. K. Youngdahl
        The Effective Use of Computers in the Nuclear Industry, Proc.
        Conf., Knoxville, Tenn., April 21-23, 1969. USAEC Report
        CONF-690401, pp. 51-54

Experimental Study of Steady and Transient Natural Convection Heat
Transfer of Mercury
    R. P. Heinisch, R. M. Singer, and R. Viskanta
        Wärme- und Stoffübertragung 1, 237-245 (1968)

The Enthalpy of Solid Tungsten from 2800°K to Its Melting Point
    L. Leibowitz, M. G. Chasanov, and L. W. Mishler
        Trans. Met. Soc. AIME 245, 981-984 (May 1969)

Comments on "Incipient Boiling Superheats in Liquid Metals"
    R. M. Singer and R. E. Holtz
        J. Heat Transfer 91(1), 199 (February 1969)

Discussion of Comments Made by G. F. Schultheiss and D. Smidt
    R. M. Singer and R. E. Holtz
        J. Heat Transfer 91(1), 200 (February 1969)

The following appeared as abstracts in Trans. Am. Nucl. Soc. <u>12</u>(1) (June 1969):

Slow Neutron Scattering from Water Vapor
    A. K. Agrawal
        p. 194

Simplified Model for Sodium Coolant Expulsion and Reentry
    A. W. Cronenberg,* H. K. Fauske, and S. G. Bankoff*
        p. 364

Data of Liquid Fraction in Sodium Liquid-Vapor Flow
    H. K. Fauske, D. J. Quinn, and W. C. Jeans
        p. 305

Critical Flow Data of Sodium Liquid-Vapor Mixtures
    H. K. Fauske, D. J. Quinn, and W. C. Jeans
        pp. 354-355

Fast Reactor Safety Status and Problems
    G. J. Fischer
        p. 11

Heat Transfer from an Aluminum/Uranium Fuel Plate in a Subcooled Pool during a TREAT Transient
    L. J. Harrison
        p. 346

Transient Free-Convection Heat Transfer in Liquid Metals in Vertical Rectangular Channels
    R. P. Heinisch, R. M. Singer, and R. Viskanta
        pp. 303-304

An Experimental Study of Incipient Sodium Superheats
    R. E. Holtz and R. M. Singer
        pp. 304-305

Determination of Stability Domain of Nonlinear Reactor Dynamics
    C. Hsu and W. T. Sha
        pp. 295-296

Capture-to-Fission Ratio Measurements of Pu^{239}
    H. P. Iskenderian
        p. 267

---

*Northwestern University.

Reactivity Transients Leading to Disassembly in Oxide-Fueled Fast
Reactors
    D. R. MacFarlane, N. A. McNeal, T. J. Heames, W. T. Sha, and
    C. K. Youngdahl
        p. 342

In-Pile Measurements of Thermal Expansion of Unirradiated EBR-II
Driver Fuel
    A. B. Rothman, C. J. Renken, R. R. Stewart, and C. E. Dickerman
        p. 349

PUBLICATION--General

Reactor Physics Division Annual Report, July 1, 1967 to June 30, 1968
    ANL-7410 (January 1969)

X